



저작자표시-비영리-변경금지 2.0 대한민국

이용자는 아래의 조건을 따르는 경우에 한하여 자유롭게

- 이 저작물을 복제, 배포, 전송, 전시, 공연 및 방송할 수 있습니다.

다음과 같은 조건을 따라야 합니다:



저작자표시. 귀하는 원저작자를 표시하여야 합니다.



비영리. 귀하는 이 저작물을 영리 목적으로 이용할 수 없습니다.



변경금지. 귀하는 이 저작물을 개작, 변형 또는 가공할 수 없습니다.

- 귀하는, 이 저작물의 재이용이나 배포의 경우, 이 저작물에 적용된 이용허락조건을 명확하게 나타내어야 합니다.
- 저작권자로부터 별도의 허가를 받으면 이러한 조건들은 적용되지 않습니다.

저작권법에 따른 이용자의 권리는 위의 내용에 의하여 영향을 받지 않습니다.

이것은 [이용허락규약\(Legal Code\)](#)을 이해하기 쉽게 요약한 것입니다.

[Disclaimer](#)

공학박사 학위논문

Numerical Investigation of the
Interaction between Flow
Structures and Sediment
Behaviors Downstream of
Backward-Facing Steps and
Aprons

후향 계단 및 하상 보호공 배후 흐름 구조와 유사 거동
의 상호작용에 대한 수치적 연구

2023 년 8 월

서울대학교 대학원

건설환경공학부

이 정 후

Numerical Investigation of the Interaction
between Flow Structures and Sediment Behaviors
Downstream of Backward-Facing Steps and
Aprons

후향 계단 및 하상 보호공 배후 흐름 구조와 유사 거동의
상호작용에 대한 수치적 연구

지도 교수 Van Thinh Nguyen
이 논문을 공학박사 학위논문으로 제출함

2023 년 3 월

서울대학교 대학원
건설환경공학부
이 정 후

이정후의 박사학위논문을 인준함
2023 년 6 월

위 원 장 박 용 성 (인)

부위원장 Van Thinh Nguyen (인)

위 원 우 효 섭 (인)

위 원 Philippe Gourbesville (인)

위 원 송 창 근 (인)

Abstract

Numerical Investigation of the Interaction between Flow Structures and Sediment Behaviors Downstream of Backward-Facing Steps and Aprons

이 정 후 (Jeonghu Lee)

건설환경공학부 (Civil and Environmental Engineering)

The Graduate School

Seoul National University

The study of the flow over hydraulic structures is still of particular interest to researchers due to the complexity of flow characteristics and sediment behaviors. This thesis is to investigate the flow and sediment behaviors behind hydraulic structures, such as various inclined backward-facing steps (BFSs) and a submerged

sluice gate. The effect of BFS angles on near-bed turbulent flow structures and bedload transport rate, as well as their interactions, is examined in surface jet flow. A combined numerical technique of large eddy simulation (LES) and discrete element method (DEM), based on the open source package OpenFOAM, is employed. The validation of the numerical model shows a good agreement between the simulation results and observed data obtained from different experiments. The simulation results reveal that the flow does not form a separation zone when the BFS angle is less than 20° , wherein the near-bed turbulence intensity is insufficient to induce substantial sediment movements. As the step angle is increased to a certain value (20°), the separation flow is formed. Consequently, the near-bed turbulence intensity is significantly increased due to the splat effect, and the sediment flux is also drastically increased. As the BFS angle further increases to 30° and 90° , the reattachment length is extended without notable changes in maximum turbulence intensity near the bed. The peaks of the mean bedload transport rate are located further downstream along the extended reattachment length. The quadrant analysis for bedload transport is performed, and the results demonstrate that the sweep event plays a significant role in moving most sediment downstream of the reattachment point. On the other hand, right upstream of the reattachment point, the burst becomes the dominant turbulence event to move the majority of the sediment backward in the upstream direction. In addition, this study further examines the flow and sediment behaviors behind an apron in submerged wall jet flow when a sluice gate is opened. For this flow regime, the effect of wide-area air injection on scour mitigation is evaluated. The LES-DEM coupling model is further expanded to incorporate air phase. The bed profile simulated by the LES-DEM model exhibited good agreement with observation data. The bedload transport rate and the maximum scour depth are

significantly reduced by the air injection, which also decreases the near-wall mean streamwise velocity. This result confirms that reducing the mean streamwise velocity is the most influential factor in mitigating scour. Although the mean vertical velocity and turbulence intensity are substantially increased due to the air injection, these factors do not contribute significantly to sediment behaviors. The maximum scour depth is shown to be decreased with a higher air injection flow rate and larger air injection area. The quadrant analysis for bedload transport reveals that without air injection, the sweep event is primarily responsible for the initial scour process. However, when air is injected, the sediment moves by primarily outward and inward interactions with a substantially reduced transport rate.

Keyword: Bedload transport; LES–DEM coupling; reattachment length; submerged wall jet flow; surface jet flow; wide–area air injection.

Student number: 2017–31683

TABLE OF CONTENTS

Abstract	i
TABLE OF CONTENTS	iv
NOMENCLATURE.....	vi
List of Tables.....	xi
List of Figures	xiii
CHAPTER 1. INTRODUCTION	1
1.1 General introduction.....	1
1.2 Motivation and necessity of research	4
1.3 Objectives.....	7
1.4 Study outline	9
CHAPTER 2. BACKGROUND CONCEPTS	11
2.1 Surface jet flow behind BFS	11
2.2 Submerged wall jet flow behind sluice gate.....	13
CHAPTER 3. LITERATURE REVIEW.....	16
3.1 Surface jet flow behind BFS	16
3.1.1 Flow and turbulence structure in separation zone	16
3.1.2 Flow-sediment interaction in separation zone.....	18
3.1.3 Effect of BFS angle on reattachment length	19
3.2 Local scour by horizontal wall jet flow.....	22
CHAPTER 4. METHODOLOGY.....	26
4.1 Numerical simulation using OpenFOAM	27
4.2 Large Eddy Simulation (LES).....	29
4.3 Coupling of LES and DEM.....	31
4.4 Incorporation of air phase into LES-DEM model	35
4.5 Measurement of reattachment length	37
4.6 Visualization of vortex structure	37

4.7 Bedload transport rate	38
4.8 Quadrant analysis for flow structure	39
4.9 Quadrant analysis for bedload transport.....	40
CHAPTER 5. Computational Setup and Application	41
5.1 Surface jet flow behind various inclined BFSs	41
5.2 Submerged wall jet flow with air injection behind sluice gate	45
CHAPTER 6. MODEL VALIDATION.....	51
6.1 Validation against surface jet flow over BFS.....	51
6.1.1 Validation of hydrodynamic model.....	51
6.1.2 Validation of LES-DEM coupling model	61
6.2 Validation against submerged wall jet flow	65
6.2.1 Validation of numerical model against mean velocity	66
6.2.2 Validation of numerical model against scouring dimensions.....	67
CHAPTER 7. RESULTS	71
7.1 Surface jet flow behind various inclined BFSs	71
7.1.1 Near-bed flow structure.....	71
7.1.2 Sediment flux	83
7.1.3 Quadrant analysis for flow structure	86
7.1.4 Quadrant analysis for bedload transport.....	90
7.2 Submerged wall jet flow with air injection behind sluice gate	95
7.2.1 Bed profile and sediment flux	95
7.2.2 Flow and turbulence structures.....	112
7.2.3 Quadrant analysis for bedload transport.....	138
CHAPTER 8. CONCLUSIONS.....	142
REFERENCES.....	150
Appendix.....	172
초 록.....	177
감사의 글.....	180

NOMENCLATURE

Latin symbols

a	Height of the opening of a sluice gate
A_h	Measurement area for bedload transport rate
B	Length of the sediment zone behind an apron
c_{pn}	Normal damping coefficients
c_{pt}	Tangential damping coefficients
C_d	Drag force coefficient
C_s	Smagorinsky constant
C_k	Kolmogorov constant
d_p	Particle diameter
d_{50}	Particle median diameter
dt	Time step for sampling numerical data
D	Vertical distance from the apron to numerical atmosphere
F_r	Froude number
F_{pb}	Particle body force
F_{pd}	Drag force based on the relative velocity of fluid and particle
F_{pn}	Normal contact force
F_{pp}	Pressure force exerted on the particle
F_{pt}	Tangential contact force
F_{pv}	Viscous force exerted on the particle
g	Gravitational acceleration
h	Initial thickness of sediment behind an apron
h_m	Maximum scour depth
I_i	Unity if a fluctuating velocity pair is measured in i-th quadrant

H	Step height of backward-facing step
I_p	Angular moment of inertia
k_{pn}	Normal spring stiffness
k_{pt}	Tangential spring stiffness
L	Apron length
m_p	Particle mass
M_a	Momentum of injected air
M_w	Momentum of inflowing water
n_f	volume fraction occupied by fluid
n_w	volume fraction of water in fluid
n_a	volume fraction of air in fluid
N_{pV}	The number of particles in a local cell volume
N_p	The number of particles in a bedload measurement area
p	Fluid pressure
P_i	Ratio of time occupied by each turbulence event in the i-th quadrant
P_{qi}	Ratio of bedload transport rate during each turbulence event in the i-th quadrant
q_x	Instantaneous bedload transport rate
Q	Isosurface value of Q-criterion
Q_x	Mean bedload transport rate
Q_a	Air injection flow rate
Q_w	Inflowing water flow rate
R^2	R-square value
R_{fp}	Fluid-particle momentum exchange
RA	Air injection length from an apron
Re	Reynolds number
Re_p	Particle Reynolds number
t	Simulation time

t_o	Initial simulation time
T	Time period for averaging flow variables
T_e	Time period to achieve the equilibrium bed profile
\mathbf{T}_{pr}	Rolling friction torque
TI_x	Streamwise turbulence intensity
TI_y	Vertical turbulence intensity
\mathbf{u}	Instantaneous velocity vector
u'	Streamwise fluctuating velocity
\mathbf{u}_p	Instantaneous particle velocity vector
u_r	Relative velocity between water and air
u^*	Friction velocity near the wall
$\Delta \mathbf{u}_{pn}$	Normal relative velocity of particle at the contact position
$\Delta \mathbf{u}_{pt}$	Tangential relative velocity of particle at the contact position
\mathbf{U}	Mean velocity vector
U	Mean streamwise velocity
U_0	Maximum mean streamwise velocity above the step edge
U_a	Inlet velocity of the wall jet at the sluice gate.
v'	Vertical fluctuating velocity
V	Mean vertical velocity, local cell volume
V_p	Volume occupied by DEM particles
V_s	Scour volume
V_w	Volume occupied by water
V_a	Volume occupied by air
W	Width of the sediment zone behind an apron
x	Longitudinal coordinate in Cartesian coordinate system
x'	Modified x-coordinate starting from $x = x_b$
x_b	Horizontal width of the step
x_r	Reattachment length

X_d	Horizontal distance from the apron to the dune crest
X_m	Horizontal distance from the apron to the dune trough
$\Delta \mathbf{x}_p$	Overlap distance of particles
y	Vertical coordinate in Cartesian coordinate system
y_z	Inner layer thickness of wall jet flow
y^+	Dimensionless wall-distance calculated by dimensionless velocity near the wall
z	Lateral coordinate in Cartesian coordinate system

Greek symbols

α	Backward-facing step angle
ρ	Density of mixed fluid
ρ_s	Density of air
ρ_s	Density of sediment
ρ_w	Density of water
ℓ_d	Height of downstream channel of backward-facing step
ℓ_u	Height of upstream channel of backward-facing step
$\boldsymbol{\tau}$	shear stress tensor
κ	von Karman constant
μ	dynamic viscosity
μ_{eff}	Effective dynamic viscosity
μ_{pc}	Coulomb friction coefficient
μ_r	Rolling friction coefficient
χ	Empirical coefficient for determining drag force with porosity
μ_{SGS}	Subgrid scale dynamic viscosity
ν	kinematic viscosity
ν_t	turbulent kinematic viscosity
$\boldsymbol{\omega}_p$	Angular particle velocity vector

ω_z	Streamwise vorticity component (rotation about the z-axis)
S	Strain rate tensor
Ω	Rotation tensor

Acronyms

3D	Three dimension
AD	Aerodynamic model
BFS	Backward-facing step
CFD	Computational fluid dynamics
DEM	Discrete element method
DNS	Direct numerical simulation
ER	Expansion ratio in backward-facing step geometry
HD	Hydrodynamic model
LES	Large eddy simulation
RANS	Reynolds-averaged Navier-Stokes
RMSE	Root mean squared error
SGS	Subgrid scale
SSL	Separated shear layer
TKE	Turbulent kinetic energy
VOF	Volume of Fluid

List of Tables

TABLE 1. PREVIOUS STUDIES ON FLOW AND SEDIMENT BEHAVIORS BY SEPARATION FLOW IN SURFACE JET FLOW.	21
TABLE 2. PREVIOUS STUDIES ON FLOW CHARACTERISTICS AND SCOURING BY HORIZONTAL WALL JET FLOW.	25
TABLE 3. CONFIGURATION OF THE NUMERICAL SIMULATION FOR SURFACE JET FLOW.	45
TABLE 4. LENGTH SCALE IN THE NUMERICAL DOMAIN.	47
TABLE 5. CONFIGURATION OF THE NUMERICAL SIMULATION FOR SUBMERGED WALL JET FLOW.	50
TABLE 6. R^2 AND RMS VALUES BETWEEN THE SIMULATION RESULTS AND EXPERIMENTAL DATA FROM RUCK AND MAKIOLA (1993) AND NAKAGAWA AND NEZU (1987).	60
TABLE 7. COMPARISON OF PERCENTAGE OF TIME OCCUPIED BY EACH TURBULENCE EVENT BETWEEN THE OBSERVATION DATA BY NELSON ET AL. (1995) AND SIMULATION RESULTS.	64
TABLE 8. COMPARISON OF PERCENTAGE OF EACH TURBULENCE EVENT WEIGHTED BY BEDLOAD TRANSPORT RATE BETWEEN THE OBSERVATION DATA BY NELSON ET AL. (1995) AND SIMULATION RESULTS.	64
TABLE 9. EXPERIMENTAL CONFIGURATION FROM CHATTERJEE ET AL. (1994).	66
TABLE 10. COMPARISON OF THE SCOUR HOLE'S DIMENSIONS BETWEEN THE SIMULATION AND EMPIRICAL FORMULA FROM CHATTERJEE ET AL. (1994).	69
TABLE 11. NEAR-BED FLOW INFORMATION AND BEDLOAD TRANSPORT RATE. 83	
TABLE 12. RATIO OF TIME (IN PERCENTAGE) BY EACH TURBULENCE EVENT IN VARIOUS BFS ANGLES.	87
TABLE 13. RATIO (IN PERCENTAGE) OF BEDLOAD TRANSPORT RATE DURING EACH TURBULENCE EVENT IN VARIOUS BFS ANGLES.	94
TABLE 14. DIMENSIONS OF SCOUR HOLE WITH AND WITHOUT AIR INJECTION IN THE CENTRAL VERTICAL PLANE.	111

TABLE 15. MAXIMUM MEAN VELOCITY AND TURBULENCE INTENSITY IN Y AXIS AT $x = 0$ IN THE CENTRAL VERTICAL PLANE.	136
TABLE 16. NEAR-BED MEAN VELOCITY AND TURBULENCE INTENSITY AT $x = 0$ AND $y = 5$ mm IN THE CENTRAL VERTICAL PLANE.	137
TABLE 17. RATIO (IN PERCENTAGE) OF BEDLOAD TRANSPORT RATE DURING EACH TURBULENCE EVENT WITH AND WITHOUT AIR INJECTION IN WALL JET FLOW.	141

List of Figures

FIGURE 1. FLOW CHART OF THE RESEARCH PROCEDURE.....	10
FIGURE 2. SCHEMATIC DIAGRAM OF DIFFERENT FLOW REGIMES OVER BFS SUGGESTED BY WU AND RAJARATNAM (1998).	12
FIGURE 3. SCHEMATIC DIAGRAM OF SUBMERGED WALL JET FLOW BEHIND SLUICE GATE.....	14
FIGURE 4. BOUNDARY LAYER OF SUBMERGED WALL JET FLOW, READAPTED FROM DEY ET AL. (2010).....	15
FIGURE 5. CONCEPTUAL MODEL OF A VORTEX TUBE FORMATION BEHIND DUNE PROPOSED BY MÜLLER AND GYR (1986).....	17
FIGURE 6. COUPLING ALGORITHM BETWEEN LES AND DEM	34
FIGURE 7. SCHEMATIC ILLUSTRATION OF THE FLUIDS (WATER AND AIR) AND SEDIMENT BASED ON THE VOLUME FRACTION IN A NUMERICAL CELL.	36
FIGURE 8. SCHEMATIC DIAGRAM OF THE COMPUTATIONAL DOMAIN WITH VARIOUS INCLINED BFSs (DIAGRAM IS NOT TO THE SCALE).	44
FIGURE 9. SCHEMATIC DIAGRAM OF THE COMPUTATIONAL DOMAIN FOR WALL JET FLOW BEHIND A SLUICE GATE (DIAGRAM IS NOT TO THE SCALE).....	49
FIGURE 10. STREAMWISE VELOCITY (A, B, C) AND TURBULENCE INTENSITY (D, E, F) PROFILES BEHIND THE STEP AT $Re=15000$, $\alpha = 10^\circ, 30^\circ, 90^\circ$, AND $ER=1.48$ (BLUE LINE IS THE LOCATION OF REATTACHMENT POINT IN THE SIMULATION; RED LINE IN THE EXPERIMENT).....	54
FIGURE 11. STREAMWISE VELOCITY (A, B, C) AND TURBULENCE INTENSITY (D, E, F) PROFILES BEHIND THE STEP AT $Re=47000$, $\alpha = 10^\circ, 30^\circ, 90^\circ$, AND $ER=1.48$ (BLUE LINE IS THE LOCATION OF REATTACHMENT POINT IN THE SIMULATION; RED LINE IN THE EXPERIMENT).....	55
FIGURE 12. STREAMWISE VELOCITY (A, B, C, D, E) PROFILES BEHIND THE STEP AT $Re=64000$, $\alpha = 10^\circ, 15^\circ, 25^\circ, 30^\circ, 90^\circ$, AND $ER=1.48$ (BLUE LINE IS THE LOCATION OF REATTACHMENT POINT IN THE SIMULATION; RED LINE IN THE EXPERIMENT).	56
FIGURE 13. STREAMWISE VELOCITY (A, B, C, D, E, F) PROFILES BEHIND THE STEP AT $Re=15000$, $\alpha = 10^\circ, 20^\circ, 25^\circ, 30^\circ, 45^\circ, 90^\circ$, AND $ER=2$ (BLUE	

LINE IS THE LOCATION OF REATTACHMENT POINT IN THE SIMULATION; RED LINE IN THE EXPERIMENT).....	57
FIGURE 14. STREAMWISE VELOCITY (A, B, C, D, E) PROFILES BEHIND THE STEP AT $Re=47000$, $\alpha = 10^\circ, 25^\circ, 30^\circ, 45^\circ, 90^\circ$, AND $ER=2$ (BLUE LINE IS THE LOCATION OF REATTACHMENT POINT IN THE SIMULATION; RED LINE IN THE EXPERIMENT).....	58
FIGURE 15. STREAMWISE VELOCITY (A, B, C, D) PROFILES BEHIND THE STEP AT $Re=64000$, $\alpha = 10^\circ, 25^\circ, 45^\circ, 90^\circ$, AND $ER=2$ (BLUE LINE IS THE LOCATION OF REATTACHMENT POINT IN THE SIMULATION; RED LINE IN THE EXPERIMENT).....	59
FIGURE 16. STREAMWISE VELOCITY (A), STREAMWISE TURBULENCE INTENSITY (B), AND VERTICAL TURBULENCE INTENSITY (C) PROFILES BEHIND THE STEP (BLUE LINE IS THE LOCATION OF REATTACHMENT POINT IN THE SIMULATION; RED LINE IN THE EXPERIMENT).....	60
FIGURE 17. NEAR-BED STREAMWISE VELOCITY (A), STREAMWISE TURBULENCE INTENSITY (B), AND VERTICAL TURBULENCE INTENSITY (C) PROFILES BEHIND THE STEP (DOTTED LINE=OBSERVATION DATA BY NELSON ET AL. (1995); SOLID LINE=SIMULATION DATA).....	63
FIGURE 18. MEAN BEDLOAD TRANSPORT RATE IN THE STREAMWISE DIRECTION BEHIND THE BFS (CIRCLE=SIMULATION DATA; CIRCLE (FILLED)=OBSERVATION BY NELSON ET AL. (1995)).	64
FIGURE 19. EXPERIMENTAL SETUP OF CHATTERJEE ET AL. (1994).....	65
FIGURE 20. COMPARISON OF VERTICAL DISTRIBUTION OF NORMALIZED STREAMWISE VELOCITY BETWEEN SIMULATION AND EXPERIMENT	67
FIGURE 21. RELATIONSHIPS OF DIMENSIONS OF SCOUR HOLE AND SCOUR VOLUME FROM CHATTERJEE ET AL. (1994). RED DOTS REPRESENT THE EXPERIMENTAL SETS.	68
FIGURE 22. SCOUR HOLE'S DIMENSIONS FORMED BY SIMULATION AND ESTIMATED BY CHATTERJEE ET AL. (1994).	70
FIGURE 23. MEAN STREAMWISE VELOCITY FOR CASEN10 (A), CASEN20 (B), CASEN30 (C), AND CASEN90 (D). SOLID LINE REPRESENTS THE REATTACHMENT POINT.	73

FIGURE 24. STREAMWISE TURBULENCE INTENSITY FOR CASEN10 (A), CASEN20 (B), CASEN30 (C), AND CASEN90 (D). SOLID LINE REPRESENTS THE REATTACHMENT POINT.	74
FIGURE 25. VERTICAL TURBULENCE INTENSITY FOR CASEN10 (A), CASEN20 (B), CASEN30 (C), AND CASEN90 (D). SOLID LINE REPRESENTS THE REATTACHMENT POINT.	75
FIGURE 26. SEPARATION ZONE WITH TIME-AVERAGED VELOCITY VECTORS IN THE CENTRAL SECTION OF THE Z-AXIS FOR CASEN10 (A), CASEN20 (B), CASEN30 (C), AND CASEN90 (D).	76
FIGURE 27. STREAMWISE VELOCITY PROFILES BEHIND THE STEP MEASURED IN THE CENTRAL VERTICAL PLANE FOR CASEN10 (A), CASEN20 (B), CASEN30 (C), AND CASEN90 (D). BLUE LINE REPRESENTS THE REATTACHMENT POINT.	77
FIGURE 28. STREAMWISE TURBULENCE INTENSITY PROFILES BEHIND THE STEP MEASURED IN THE CENTRAL VERTICAL PLANE FOR CASEN10 (A), CASEN20 (B), CASEN30 (C), AND CASEN90 (D). BLUE LINE REPRESENTS THE REATTACHMENT POINT.....	78
FIGURE 29. VERTICAL TURBULENCE INTENSITY PROFILES BEHIND THE STEP MEASURED IN THE CENTRAL VERTICAL PLANE FOR CASEN10 (A), CASEN20 (B), CASEN30 (C), AND CASEN90 (D). BLUE LINE REPRESENTS THE REATTACHMENT POINT.....	80
FIGURE 30. COHERENT VORTEX STRUCTURES VISUALIZED BY Q-CRITERION (ISOSURFACE: $Q=600$) FOR CASEN10 (A), CASEN20 (B), CASEN30 (C), AND CASEN90 (D) AT DIFFERENT INSTANTS.....	82
FIGURE 31. MEAN BEDLOAD TRANSPORT RATE DOWNSTREAM OF THE VARIOUS INCLINED BFSS (THE DASH LINES SHOW THE LOCATIONS OF REATTACHMENT POINTS ASSOCIATED WITH STEP ANGLES).	84
FIGURE 32. JOINT FREQUENCY DISTRIBUTIONS OF u' AND v' MEASURED AT $x = x_b$ (a), $x_b + 5H$ (b), AND $x_b + 10H$ (c) FOR CASEN10, AND $x = x_r$ (d), $x_r + 5H$ (e), $x_r + 10H$ (f) FOR CASEN20.....	88
FIGURE 33. JOINT FREQUENCY DISTRIBUTIONS OF u' AND v' MEASURED AT $x = x_r - 2.5H$ (a, d), x_r (b, e), AND $x_r + 5H$ (c, f) FOR CASEN30 (A-C) AND CASEN90 (D-F).....	89

FIGURE 34. JOINT FREQUENCY DISTRIBUTIONS OF u' AND v' WEIGHTED BY qx MEASURED AT $x = x_b$ (a), $x_b + 5H$ (b), $x_b + 10H$ (c) FOR CASEN10, AND $x = x_r$ (d), $x_r + 5H$ (e), $x_r + 10H$ (f) FOR CASEN20.	92
FIGURE 35. JOINT FREQUENCY DISTRIBUTIONS OF u' AND v' WEIGHTED BY qx MEASURED AT $x = x_r - 2.5H$ (a, d), x_r (b, e), AND $x_r + 5H$ (c, f) FOR CASEN30 (A-C) AND CASEN90 (D-F).	93
FIGURE 36. BEDFORM CHANGES OVER TIME IN CASENA.	97
FIGURE 37. BEDFORM CHANGES OVER TIME IN CASERA2Q025.	98
FIGURE 38. BEDFORM CHANGES OVER TIME IN CASERA2Q05.	99
FIGURE 39. BEDFORM CHANGES OVER TIME IN CASERA2Q1.	100
FIGURE 40. BEDFORM CHANGES OVER TIME IN CASERA20Q025.	101
FIGURE 41. BEDFORM CHANGES OVER TIME IN CASERA20Q05.	102
FIGURE 42. BEDFORM CHANGES OVER TIME IN CASERA20Q1.	103
FIGURE 43. BEDFORM CHANGES OVER TIME IN CASERA40Q025.	104
FIGURE 44. BEDFORM CHANGES OVER TIME IN CASERA40Q05.	105
FIGURE 45. BEDFORM CHANGES OVER TIME IN CASERA40Q1.	106
FIGURE 46. COMPARISON OF BEDLOAD TRANSPORT RATE AT VARIOUS TIME INTERVALS FOR CASENA AND CASERA2Q025-Q1.	108
FIGURE 47. COMPARISON OF BEDLOAD TRANSPORT RATE AT VARIOUS TIME INTERVALS FOR CASENA AND CASERA20Q025-Q1.	109
FIGURE 48. COMPARISON OF BEDLOAD TRANSPORT RATE AT VARIOUS TIME INTERVALS FOR CASENA AND CASERA40Q025-Q1.	110
FIGURE 49. COMPARISON OF MEAN VELOCITY (A) AND TURBULENT KINETIC ENERGY (B) CONTOURS IN THE CENTRAL VERTICAL PLANE ($Z/W=0.5$) FOR CASENA.	113
FIGURE 50. COMPARISON OF MEAN VELOCITY (A) AND TURBULENT KINETIC ENERGY (B) CONTOURS IN THE CENTRAL VERTICAL PLANE ($Z/W=0.5$) FOR CASENA.	116
FIGURE 51. COMPARISON OF MEAN VELOCITY (A, B) AND TURBULENCE INTENSITY (C, D) CONTOURS IN THE CENTRAL VERTICAL PLANE ($Z/W=0.5$) FOR CASERA2Q025.	117

FIGURE 52. COMPARISON OF MEAN VELOCITY (A, B) AND TURBULENCE INTENSITY (C, D) CONTOURS IN THE CENTRAL VERTICAL PLANE ($Z/W=0.5$) FOR CASERA2Q05.....	118
FIGURE 53. COMPARISON OF MEAN VELOCITY (A, B) AND TURBULENCE INTENSITY (C, D) CONTOURS IN THE CENTRAL VERTICAL PLANE ($Z/W=0.5$) FOR CASERA2Q1.....	119
FIGURE 54. COMPARISON OF MEAN VELOCITY (A, B) AND TURBULENCE INTENSITY (C, D) CONTOURS IN THE CENTRAL VERTICAL PLANE ($Z/W=0.5$) FOR CASERA20Q025.....	120
FIGURE 55. COMPARISON OF MEAN VELOCITY (A, B) AND TURBULENCE INTENSITY (C, D) CONTOURS IN THE CENTRAL VERTICAL PLANE ($Z/W=0.5$) FOR CASERA20Q05.....	121
FIGURE 56. COMPARISON OF MEAN VELOCITY (A, B) AND TURBULENCE INTENSITY (C, D) CONTOURS IN THE CENTRAL VERTICAL PLANE ($Z/W=0.5$) FOR CASERA20Q1.....	122
FIGURE 57. COMPARISON OF MEAN VELOCITY (A, B) AND TURBULENCE INTENSITY (C, D) CONTOURS IN THE CENTRAL VERTICAL PLANE ($Z/W=0.5$) FOR CASERA40Q025.....	123
FIGURE 58. COMPARISON OF MEAN VELOCITY (A, B) AND TURBULENCE INTENSITY (C, D) CONTOURS IN THE CENTRAL VERTICAL PLANE ($Z/W=0.5$) FOR CASERA40Q05.....	124
FIGURE 59. COMPARISON OF MEAN VELOCITY (A, B) AND TURBULENCE INTENSITY (C, D) CONTOURS IN THE CENTRAL VERTICAL PLANE ($Z/W=0.5$) FOR CASERA40Q1.....	125
FIGURE 60. COMPARISON OF MEAN VELOCITY (A, B) AND TURBULENCE INTENSITY (C, D) PROFILES IN THE CENTRAL VERTICAL PLANE ($Z/W=0.5$) BETWEEN CASENA AND CASERA20Q025-Q1.....	128
FIGURE 61. COMPARISON OF MEAN VELOCITY (A, B) AND TURBULENCE INTENSITY (C, D) PROFILES IN THE CENTRAL VERTICAL PLANE ($Z/W=0.5$) BETWEEN CASENA AND CASERA20Q025-Q1.....	129
FIGURE 62. COMPARISON OF MEAN VELOCITY (A, B) AND TURBULENCE INTENSITY (C, D) PROFILES IN THE CENTRAL VERTICAL PLANE ($Z/W=0.5$) BETWEEN CASENA AND CASERA40Q025-Q1.....	130

FIGURE 63. RELATION BETWEEN THE MAXIMUM SCOUR DEPTH AND NEAR-BED MEAN VELOCITY (A), TURBULENCE INTENSITY (B), MAXIMUM MEAN VELOCITY (C), AND TURBULENCE INTENSITY (D) IN THE CENTRAL VERTICAL PLANE AT $x = 0$ BETWEEN CASENA AND CASERA2.....	131
FIGURE 64. RELATION BETWEEN THE MAXIMUM SCOUR DEPTH AND NEAR-BED MEAN VELOCITY (A), TURBULENCE INTENSITY (B), MAXIMUM MEAN VELOCITY (C), AND TURBULENCE INTENSITY (D) IN THE CENTRAL VERTICAL PLANE AT $x = 0$ BETWEEN CASENA AND CASERA20.....	132
FIGURE 65. RELATION BETWEEN THE MAXIMUM SCOUR DEPTH AND NEAR-BED MEAN VELOCITY (A), TURBULENCE INTENSITY (B), MAXIMUM MEAN VELOCITY (C), AND TURBULENCE INTENSITY (D) IN THE CENTRAL VERTICAL PLANE AT $x = 0$ BETWEEN CASENA AND CASERA40.....	133
FIGURE 66. VORTEX STRUCTURES VISUALIZED BY Q-CRITERION (ISOSURFACE: Q=300) AT A TIME INSTANT FOR CASENA (A) AND CASERA20Q1 (B).....	135
FIGURE 67. JOINT FREQUENCY DISTRIBUTIONS OF u' AND v' WEIGHTED BY qx MEASURED AT $x = 0.015$ m (a, d), 0.075 m (b, e), AND 0.175 m (c, f) FOR CASENA (a, b, c) AND CASERA20Q1 (d, e, f).	140
FIGURE 68. SCHEMATIC DIAGRAM OF BACKWARD-FACING STEP FLOW, RE- ADAPTED FROM SODJA, (2007).....	176

CHAPTER 1. INTRODUCTION

1.1 General introduction

Hydraulic structures, such as dams, weirs, flood gates, grade control and drop structures, are built to prevent bed degradation and maintain a high upstream water level to facilitate irrigation, drainage systems, and ship navigation. Despite playing an important role in various human purposes, the construction of these hydraulic structures can cause a range of engineering problems related to aquatic habitats and channel morphology. In South Korea, the Singok submerged weir in the Han River has attracted attention due to environmental issues caused by flow characteristics influenced by the presence of the weir (Park and Lee, 2015; Kim, 2020). The flow regime is highly sensitive to the timing of high tides, low tides, and flooding events, leading to variations in the flow regime ranging from surface jet flow to impinging jet flow. The local scour behind weirs have also been issues in South Korea. The hydraulic structures where scouring has been notably problematic include the Changnyeong-Haman weir and Gangjeong weir on the Nakdong River and the Gongju weir on the Geum River (Yoo et al., 2012; Nguyen et al., 2015; Kwon et al., 2019; Kim and Kim, 2020). The loss of bed protections due to scouring downstream of these weirs has become a significant societal issue. Such scour behind hydraulic structures has also attracted great attention worldwide because it can lead to the failure of the structures (Bormann and Julien, 1991; Hoffmans and Pilarczyk, 1995; Pagliara and Palermo, 2015; Yalin, 1977; Vanoni, 2006; Dey and Barbhuiya, 2004; García, 2008).

The previous studies revealed that the interaction of flow, sediment movement, and the design of these structures can lead to local scour, sediment deposition, and erosion of structural components. Consequently, understanding and predicting the sediment transport processes are important for effective river management and the design of hydraulic infrastructure.

The investigations of interactions between flow and sediment transport are crucial components in ensuring the durability and safety of the hydraulic structures. A thorough understanding of the complex interrelationships between flow, sediment behavior, and structure can significantly contribute to the optimization of engineering practices in the field of river management. By examining these factors, researchers and engineers can identify vulnerabilities in existing structures, formulate innovative solutions to mitigate local scour and sediment deposition, and enhance the overall resilience of hydraulic infrastructures. Consequently, continued study of flow-sediment interactions and effective countermeasures are essential for maintaining the functionality of hydraulic structures.

However, investigating flow-sediment interactions is inherently challenging due to their complex, dynamic, and multidisciplinary nature. These interactions involve nonlinear processes, vary spatially and temporally, and depend on the diverse properties of sediments and the scale of observation. To address the challenges of scrutinizing the flow-sediment interactions, many researchers have employed experimental investigations, field observations, and numerical modeling to study the sediment transport mechanism over hydraulic structures and develop design guidelines that minimize the risks associated with sediment transport (Chatterjee and Ghosh, 1980; Hassan and Narayanan, 1985; Ali and

Lim, 1986; Nezu and Nakagawa, 1993; Chiew, 1995; Nelson et al., 1995; Melville and Coleman, 2000; Julien, 2010; Chatterjee et al., 1994; Hoffmans, 1998; Dey and Westrich, 2006; Guan et al., 2014; Schmeeckle, 2015; Ban and Choi, 2022). Both laboratory experiments and numerical models provide valuable insights into the study of flow-sediment interactions in natural. While laboratory experiments excel in offering controlled conditions and direct observation of phenomena, they can sometimes be limited by resource constraints and the challenge of replicating real-world conditions at a smaller scale. In such cases, numerical models can complement physical experiments by simulating a wider range of conditions, incorporating more detailed measurements, and reducing resource requirements.

This thesis conducts numerical simulations to investigate the flow characteristics and sediment transport processes behind submerged hydraulic structures. The complex interaction between flow structures and bedload transport is examined using quadrant analysis behind a backward-facing step (BFS). The BFS is a widely adopted representative geometry that can represent structures such as sharp-crested weirs, bed sills, drop structures, and grade control structures where the cross-sectional area of the flow abruptly changes, inducing separation flows. This study primarily investigates the changes in flow separation and turbulence characteristics as the BFS angle varies and examines their interaction with bedload transport.

Furthermore, the flow and sediment behaviors of submerged wall jet flow behind an apron during the opening of a sluice gate are also investigated. As the sediment transport

rate is high in this flow regime, the bed profile change over time is presented. Then, the effect of wide-area air injection on the flow structure and sediment behavior is evaluated.

A coupled model of large eddy simulation (LES) and discrete element method (DEM) is employed to reproduce the instantaneous near-bed turbulence structures and sediment behaviors. The three-dimensional hydrodynamics are simulated using LES approach to capture the large eddy motions by means of time-dependent, 3D Navier-Stokes equations. Meanwhile, the universal behaviors of smaller eddies (subgrid-scale) are solved by Smagorinsky model (Smagorinsky, 1963). The numerical model used in this study is thoroughly validated against experimental data to ensure its reliability. The outcomes of the present study are anticipated to provide valuable insights for the management of hydraulic infrastructures and river systems, contributing to their long-term sustainability and resilience against erosion and sedimentation-related challenges.

1.2 Motivation and necessity of research

While plenty of studies have investigated the flow characteristics and sediment behaviors over the hydraulic structures under impinging jet flows (Farhodi and Smith, 1985; Bormann and Julien, 1991; Chatterjee et al., 1994; Gaudio et al., 2000; Ben Meftah and Mossa, 2006; Tregnaighi et al., 2007; Ben Meftah and Mossa, 2020), the study under surface jet flows with lower Froude number, conceptualized by Rajaratnam and Muralidhar (1969), still has received less attention so far. Indeed, attention should also be paid to the surface jet flow, wherein a highly intense turbulent flow zone is formed due to

the flow separation, and consequently the intensified turbulent flow can induce sediment transport (Nezu and Nakagawa, 1994; Nelson et al., 1995; Liu et al., 2007; Guan et al., 2014; Ban and Choi, 2022). Generally, the mechanisms that induce sediment movement behind submerged structures in surface jet flow are known to be highly complex due to the uneasily reproducible large-scale coherent structures. The sediment motion in the separation zone is primarily affected by the eddies that develop along the separated shear layer (SSL). The eddies dominantly contribute to the growth of the shear layer, exchanging the momentum between the outside and inside of the separation zone. This eddy evolution process is of primary importance in generating large-scale coherent structures, which is the most influential factor in the instantaneous shear stress and pressure distributions inside the separation zone (Nezu and Nakagawa, 1993; Nelson et al., 1995). Several studies have investigated flow-sediment interactions with a perpendicular BFS.

Nelson et al. (1995) conducted laboratory experiments on a perpendicular BFS, measuring instantaneous near-bed flow velocities and bedload transport rates behind the separation zone. They assessed the impact of individual turbulence events (e.g., outward, burst, inward, and sweep events) on sediment movement, identifying the dominant turbulence events responsible for sediment transport. Schmeeckle (2015) performed a three-dimensional numerical analysis under conditions identical to those of Nelson et al.'s (1995) experiment. The numerical results identified the splat effect caused by fluctuations in high vertical velocities near the bed, which accelerated sediment movement. However, the aforementioned studies were confined to a perpendicular step angle. According to the findings by Ruck and Makiola (1993), flow and turbulence characteristics in separation zone change substantially with varying reattachment lengths, depending on the BFS angle.

In this context, it is essential to further examine the influence of turbulence structures in the separation zone on sediment behavior across various BFS angles. Moreover, the area under study should include not only the area downstream of the separation zone, as examined in the aforementioned studies, but also the entire region behind the BFSs, including the separation zone.

In addition to studying sediment behaviors in surface jet flow, the sediment transport process by horizontal wall jet flow behind an apron (bed protection) when a sluice gate is opened is investigated. This local scouring process can cause significant damage to hydraulic structures, and the sediment transport rate in this regime is much higher than that in surface jet flow. Scouring occurs when the wall jet flows through the apron and encounters the bed material, creating a scour hole around the foundation of the structure (Chatterjee and Ghosh, 1980; Hassan and Narayanan, 1985; Ali and Lim, 1986; Chatterjee et al., 1994; Hoffmans, 1998; Dey and Westrich, 2006). This can lead to instability of the structure and potentially catastrophic failure. Therefore, several countermeasures, including altering the roughness of the upstream boundary, implementing bed sills, and injecting air, have been studied to mitigate the significant scouring rate (Dey and Westrich, 2006; Dey et al., 2010; Champagne et al., 2016a & 2016b; Tipireddy and Barkdoll, 2019). Of these countermeasures, air injection can be more cost-effective than other measures, although it requires an air compressor with power supply. The effectiveness of air injection has been demonstrated in practice, which reduces the strength of the horizontal flow by redirecting the flow upward and thereby significantly reducing scouring (Champagne et al., 2016a & 2016b). In these studies, the air-injection area was only confined to the termination point of bed protection. However, as noted by Dey et al. (2010), the mean

streamwise flow velocity over the apron can be substantially reduced using a wide-area injection method. In this respect, it is worth considering the wide injection approach as a new scour mitigation measure. By using the wide-area injection, the air velocity required to balance the total injected air flow rate is not as high as it is with local air injection. The effectiveness of varying air injection areas and air injection flow rates needs to be assessed to enhance our understanding of how air injection mitigates local scour. This can be achieved by investigate the flow and turbulence structures over the scour zone, including the upstream of the apron, and identify the correlation between the flow structure and the scour process.

1.3 Objectives

This thesis first aims to investigate the flow and turbulence structures downstream of various inclined BFSs, as well as their interactions with sediment behaviors under surface jet flow. Given that there have not been studies investigating the effect of step angles on flow and sediment movements in surface jet flow, it is necessary to examine how flow-sediment interactions change depending on different step angles. Since the sediment transport process in surface jet flows typically occurs very slowly over time, bedform change is not analyzed for this flow regime. Instead, the bedload transport rate over a certain period is considered the primary factor to be linked with the instantaneous flow field to investigate the interaction between flow and sediment behaviors. The subcategories of this objective are as follows:

1. Coupling 3D LES (Large-Eddy Simulation) with DEM (Discrete Element Method) and setting up the coupled model through thorough validation.

2. Compare the bedload transport rate behind the various inclined BFSs.
3. Evaluate the contribution of each turbulence event to sediment movement behind the various inclined BFSs.

This study further examines the flow structure and the scour process downstream of an apron based on the established LES-DEM model. To implement the free surface and air injection, the existing two-phase LES-DEM model is expanded to incorporate air phase. As previous studies (Champagne et al., 2016a & 2016b) have only suggest local air injection approach, it is necessary to further investigate and evaluate the effect of wide-area air injection, employing various injection lengths and airflow rates, on flow structures and scour mitigation. The subcategories of this objective are as follows:

1. Incorporate air phase into the established two-phase LES-DEM coupling model.
2. Compare the flow and turbulence structures over the sediment zone, with and without air injection, varying the injection area and airflow rate.
3. Evaluate the effectiveness of the wide-area air injection approach in mitigating scour, varying the injection area and airflow rate.

1.4 Study outline

This thesis is comprised of nine chapters. Chapter 1 provides a general introduction and clarifies the motivations and the need for conducting this research. Chapter 2 elucidates the characteristics of two different flow regimes, surface jet flow and submerged wall jet flow, which are covered in this study, are explained in this chapter. Chapter 3 reviews previous studies on flow and sediment behavior over hydraulic structures, such as submerged BFS and sluice gates. Chapter 4 presents the governing equations and the coupling method of the hydrodynamic model (LES) and particle model (DEM), as well as the method of incorporating air phase. Various measurement methods used in simulations for calculating flow and sediment variables, and their interactions are presented. Chapter 5 outlines the computational domain and specifics of the numerical applications for the two different flow regimes. Chapter 6 evaluates the performance of the LES-DEM coupling model by comparing the simulated flow and sediment variables with observed data. Chapter 7 presents numerical results on the flow structures and sediment behaviors in both surface jet flow and submerged wall jet flow. For surface jet flow, flow and turbulence structures, as well as the bedload transport rate, are primarily examined across various BFS angles, with a focus on the characteristics of flow separation. For submerged wall jet flow, the main discussion revolves around the effect of wide-area air injection, varying the air injection flow rate and injection lengths, on scour mitigation. In both flow regimes, the interaction between the flow and sediment is investigated using quadrant analysis technique. Chapter 8 summarizes the findings from the simulation results and suggests directions for future research. Figure 1 schematizes the flow chart of the research procedure.

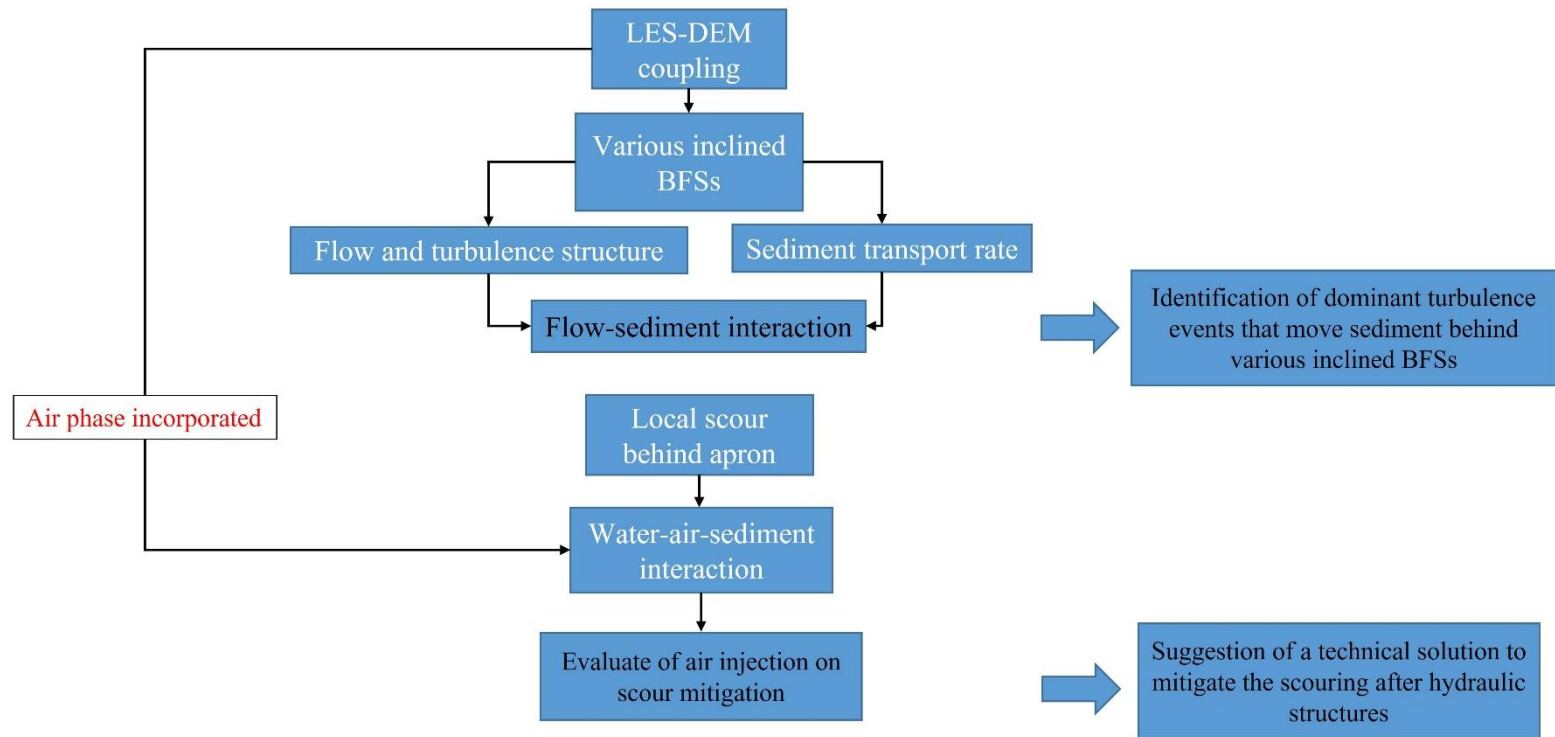


Figure 1. Flow chart of the research procedure

CHAPTER 2. BACKGROUND CONCEPTS

2.1 Surface jet flow behind BFS

Surface jet flow is one of the flow regimes classified by Wu and Rajaratnam (1996, 1998). They found that various flow regimes exist depending on the relationship between the upstream and downstream water depth of a submerged hydraulic structure, such as a sharp-crested weir and a drop structure (BFS). They classified the flows into an impinging jet and surface jet flow based on various ranges of tailwater levels. They further divided the surface flow regime into three sub-regimes of surface jet, surface wave, and breaking surface wave according to water level fluctuation right behind the submerged structures. The snapshots in Figure 2 illustrate the four different flow regimes over a drop structure, which can be considered a backward-facing step (BFS). As shown in Figure 2, the flow in surface jet regime is discharged parallel to a free surface and is separated at the BFS. The flow and turbulence characteristics, and sediment movements at downstream are featured by the flow separation and reattachment, which lead to the formation of large-scale coherent structures and intensified turbulence diffusion (Nezu and Nakagawa, 1993; Nelson et al., 1995; Chang et al., 2011). The sediment transport in this flow regime is mainly caused by the splat effect when the large-scale vortex structures impinge the bed (Nelson et al., 1995; Stoesser et al., 2008; Schmeeckle, 2015).

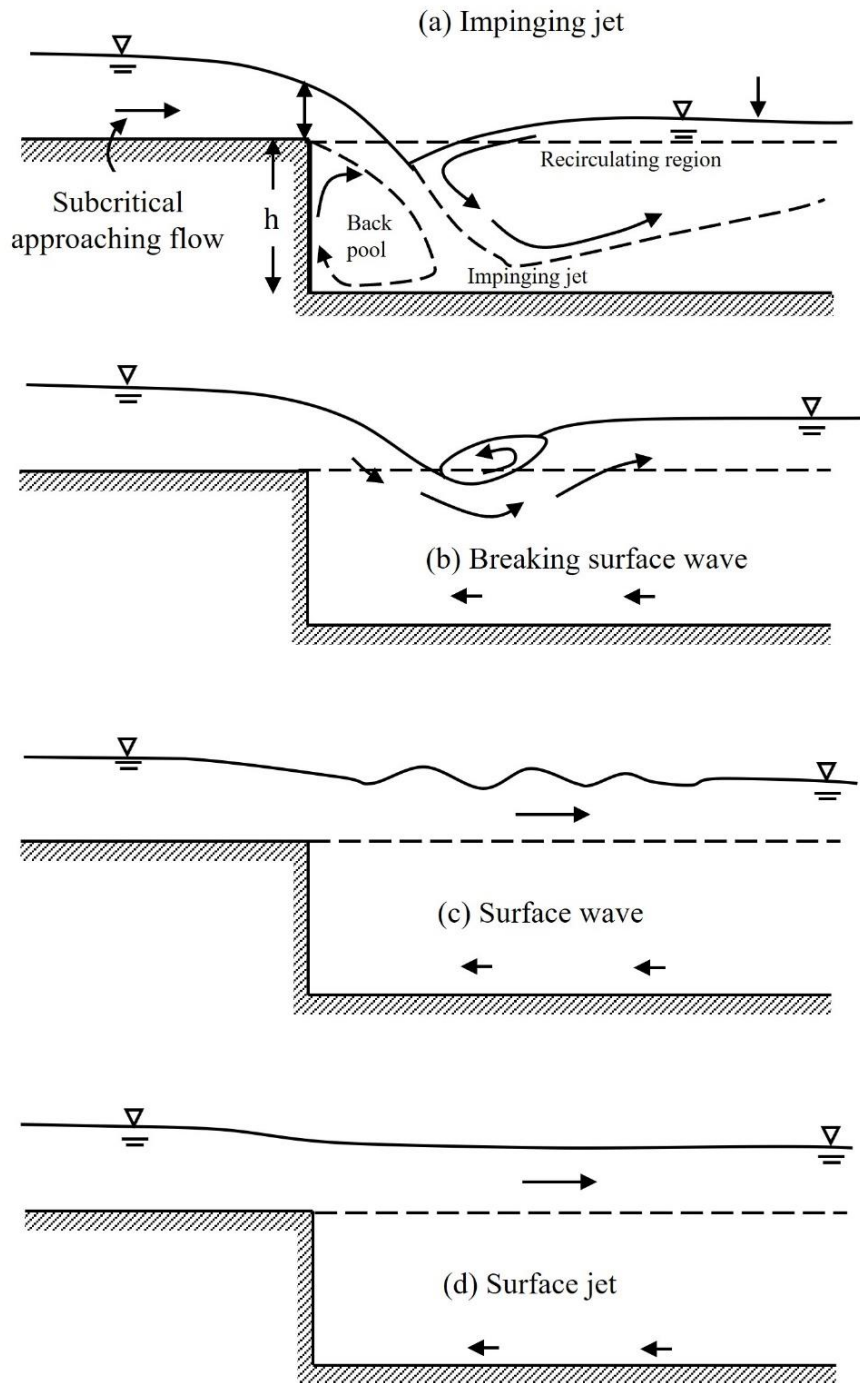


Figure 2. Schematic diagram of different flow regimes over BFS suggested by Wu and Rajaratnam (1998).

2.2 Submerged wall jet flow behind sluice gate

Submerged wall jet flow occurs when a sluice gate opens in quiescent water. This type of flow typically exhibits high stream velocity and bring massive turbulence, being discharged parallel to a bed protection. The near-wall high flow velocity generates substantial local shear stresses that typically exceed the critical shear stress required to initiate the movement of sediment, playing a significant role in the sediment transport process downstream of the apron (Khaleel and Othman, 1997; Laursen, 1952; Tarapore, 1956; Hogg et al., 1997; Chatterjee and Ghosh, 1980; Hassan and Narayanan, 1985; Ali and Lim, 1986; Chatterjee et al., 1994; Hoffmans, 1998; Dey and Sarkar, 2008). A local scour hole is rapidly formed as the wall jet flow passes a solid boundary and encounters the sediment with high energy. As the scour depth increases, the shear stress exerted on the bed is reduced; consequently, this decrease in shear stress slows down the erosion rate. It is well known that the scour depth increased with the increase of the flow velocity and the diameter of the sluice gate. Figure 3 depicts the schematic diagram of wall jet flow behind a sluice gate.

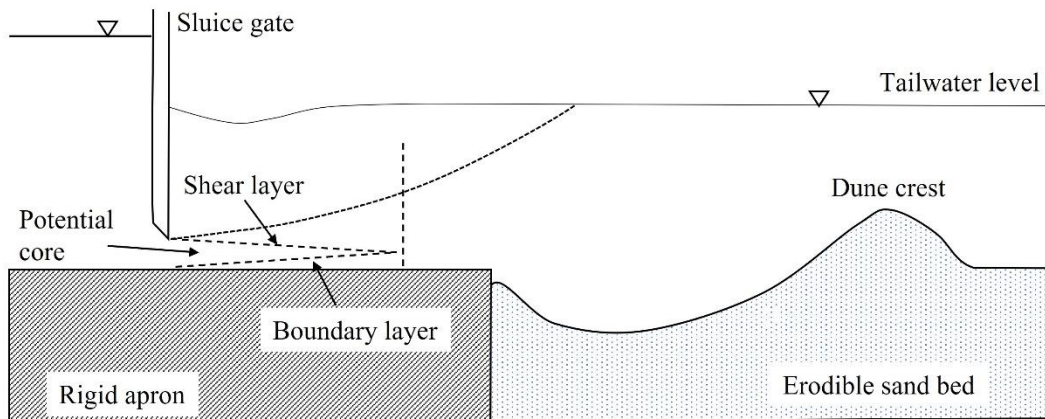


Figure 3. Schematic diagram of submerged wall jet flow behind sluice gate.

Figure 4 depicts the schematic diagram of the boundary for wall jet flow. As shown in the figure, the boundary is typically divided into the jet layer and the circulatory layer. The jet layer is further subdivided into an inner layer and an outer layer. The thickness of the inner layer, which is commonly used as a normalization factor in jet flows, is determined as a distance from the bottom boundary to the point where the jet velocity reaches its maximum, U_0 .

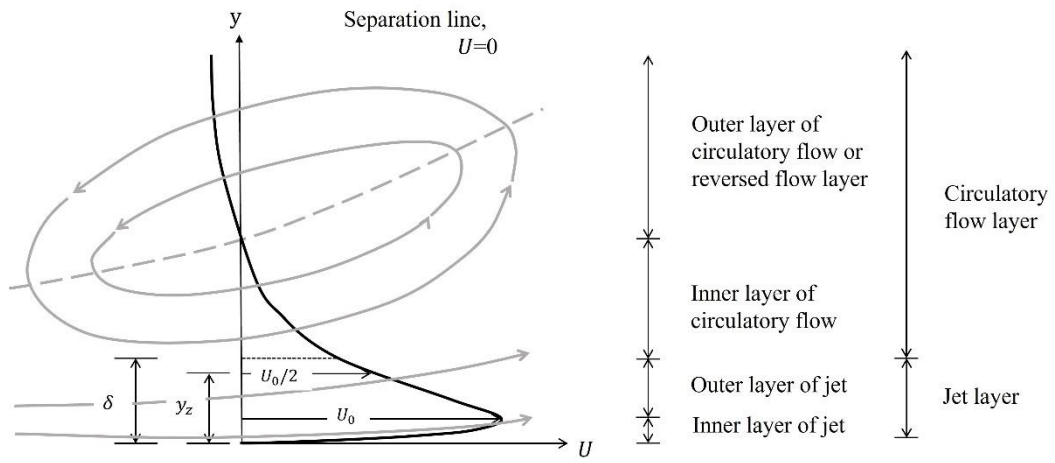


Figure 4. Boundary layer of submerged wall jet flow, readapted from Dey et al. (2010).

CHAPTER 3. LITERATURE REVIEW

3.1 Surface jet flow behind BFS

3.1.1 Flow and turbulence structure in separation zone

In the separation zone behind a BFS under surface jet flow, the sediment motion is primarily affected by the eddies that develop along the separated shear layer (SSL) (Nezu and Nakagawa, 1993). The eddies dominantly contribute to the growth of the shear layer, exchanging the momentum between the outside and inside of the separation zone. This eddy evolution process is of primary importance in generating large-scale coherent structures, the most influential factor in the instantaneous shear stress and pressure distributions inside the separation zone. A series of energetic coherent vortices, called “kolk-boil” vortices, are known to be generated at the vicinity of the reattachment point behind a single-sided BFS as the vortices along the SSL impinge on the reattachment zone, and these coherent structures are known to induce the sediment entrainment (Kiya and Sasaki, 1985; Iseya and Ikeda, 1986; Nezu and Nakagawa, 1989a; Nezu and Nakagawa, 1989b). It was reported in Eaton (1980) that the turbulent diffusion in terms of TKE and Reynolds stress is the highest in the separation zone. Several studies have also identified the high TKE and Reynolds stresses along the SSL (McLean and Smith, 1979; van Mierlo and de Ruiter, 1988; Nelson et al., 1993; Bennett and Best, 1995), indicating that the coherent vortices dominate the turbulence structure over the separation zone behind a BFS. According to Müller and Gyr (1986), Kadota and Nezu (1999), and Le Couturier et al. (2000), these large coherent vortices resemble hairpin vortices (see Figure 5).

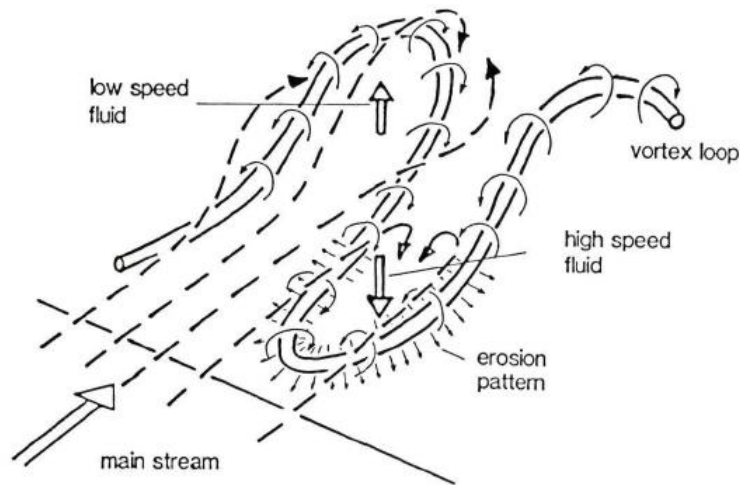


Figure 5. Conceptual model of a vortex tube formation behind dune proposed by Müller and Gyr (1986).

Several studies have examined the effect of flow separation on the instantaneous flow structures. Stoesser et al. (2008) have confirmed the influence of large-scale coherent vortices on the instantaneous flow field under a submerged flow over a fixed periodic dune profile. Their numerical results demonstrated that the large-scale coherent vortices generated by the flow separation splash on the bed, consequently, to increase the high pressure and turbulent diffusion throughout the separation zone; this phenomenon is known as the splat effect. Guan et al. (2014) examined the flow characteristics behind a submerged sharp-crested weir under surface jet flow. They confirmed that the sudden change of the flow area at the weir caused the propagating flow to be separated; and the maximum near-bed turbulence intensity in the separation zone can be considered a key factor in determining a scour hole's dimension. The bed shear stress distributions

calculated based on the measured turbulent kinetic energy appeared larger than the critical bed shear stress only for a certain distance behind the weir. More recently, based on the same flow and geometric parameters in Guan et al. (2014), Ban and Choi (2022) numerically explored the turbulent structures near the flatbed and equilibrium scour hole downstream of the sharp-crested weir. They visualized the instantaneous vortical structures along the SSL and focused more on the role of instantaneous flow behaviors than time-averaged ones. Their simulation results found that the maximum and the total amount of turbulent kinetic energy were larger for the equilibrium bed profile than for the flatbed. However, it turned out that the near-bed turbulent kinetic energy was greater for the flatbed than for the equilibrium bed profile. The mentioned studies above contributed to finding the effect of flow separation on the turbulent flow structures under surface jet flow.

3.1.2 Flow-sediment interaction in separation zone

There have been a few studies that examined to find out a correlation between the instantaneous flow structures and sediment behaviors in the separation zone. Nelson et al. (1995) conducted several laboratory experiments over a perpendicular BFS and measured the instantaneous near-bed flow velocities behind the BFS using Laser Doppler Velocimetry (LDV). Their findings identified that the sediment transport in a separation zone is mainly determined by instantaneous flow structures rather than time-averaged ones. It suggests that the local mean bed shear stress cannot be used as a suitable parameter for estimating the sediment load in a separation zone. They also found the joint frequency

distributions of fluctuating near-bed velocity using the quadrant analysis. The joint frequency was then weighted by the instantaneous bed load transport rate, measured by a high-speed camera at the same sampling frequency of the flow velocity. This enabled the quantification of the contribution of each turbulence event (e.g., the outward, burst, inward, and sweep events) to moving the sediment particles downstream of the flow reattachment point. It turned out that the outward and sweep events were the dominant turbulence types to drag most sediments behind the separation zone. More recently, a three-dimensional numerical study using a perpendicular BFS has been performed by Schmeeckle (2015), following the experiment of Nelson et al. (1995). His results suggest that the high instantaneous vertical velocity near the bed is a major factor in determining the splat effect, which leads to the increased instantaneous bed shear stress and pressure, hence increasing the sediment movement.

The studies mentioned above significantly contributed to a comprehensive understanding of complex flow characteristics and sediment transport processes, including their interactions, under surface jet flow. However, given that these studies only considered perpendicular angle of the step, it is necessary to investigate the flow and sediment behaviors for a wider range of BFS angles.

3.1.3 Effect of BFS angle on reattachment length

The reattachment length behind a BFS is determined by several geometric and flow parameters, such as the Reynolds number, expansion ratio, and upstream boundary layer state (Kuehn, 1980; Armaly et al., 1983; Durst and Tropea, 1983; Adams and Johnston,

1988; Ötügen, 1991; Williams and Baker, 1997; Tylli et al., 2002; Biswas et al., 2004; Nie and Armaly, 2004; Chen et al., 2006). Despite a wide range of previous studies on BFS flows, the dependence of the flow and turbulence characteristics, primarily reattachment length, on the BFS angle remains ambiguous. Chen et al. (2006) conducted 3D numerical simulations to figure out the effect of BFS angle on the flow structures and heat transfer distribution in a rectangular duct. The results showed that the magnitude of friction coefficients downstream of the BFS increases over the flow reattachment zone. As the BFS angle increases, the recovery of the friction becomes slower behind the flow reattachment zone. They did not provide any near wall turbulence measurements, such as turbulence intensity and Reynolds stress.

Ruck and Makiola (1993) conducted a total of 75 wind-tunnel experiments, varying the BFS angles and expansion ratios. The results indicated that the flow separation occurs at BFS angles between 15° ~ 20° . The reattachment length was observed to increase asymptotically with the BFS angle at high Reynolds numbers, defined in their study as over 15,000. It also turned out that the near-bed turbulence intensity in the separation zone increases drastically once the flow separation occurs, reaching its maximum around the flow reattachment point. Choi and Nguyen (2016) investigated the overall flow pattern over a BFS with various step angles based on numerical simulations using Reynolds averaged navier-stokes equation (RANS) and large eddy simulations (LES) following the experimental configurations in Ruck and Makiola (1993). The simulation results indicated that the LES approach provides greater accuracy than RANS in reproducing flow characteristics, such as velocity and turbulence intensity profiles, when compared with the measurement data of Ruck and Makiola (1993). It also revealed that the increase ratio in

reattachment length dramatically decreases from a BFS angle of 45° in high Reynolds number cases, which is consistent with the findings by Ruck and Makiola (1993). Table 1 summarizes the representative previous studies on flow and sediment behaviors in hydraulic structures with separation flow for surface jet flow regime.

Table 1. Previous studies on flow and sediment behaviors by separation flow in surface jet flow.

References	Experiment	Geometry	Main findings
Eaton (1980)	Lab	BFS	The effect of boundary layer state on turbulent flow behind a BFS.
Nezu and Nakagawa (1993)	Lab	BFS	Sediment behaviors associated with coherent structures in separation zone.
Ruck and Makiola (1993)	Lab	Inclined BFSs	Flow and turbulence structures over various inclined BFSs using wind tunnel experiments.
Nelson et al. (1995)	Lab	BFS	Quantified flow-sediment interactions by quadrant analysis downstream of the separation zone.
Stoessor et al. (2008)	CFD	Fixed periodic dune	Instantaneous flow and vortex structures over the separation zone.
Guan et al. (2014)	Lab	Sharp-crested weir	The maximum near-bed turbulence intensity as a key factor in determining a scour hole's dimension.
Schmeeckle (2015)	CFD	BFS	Numerically identified the splat effect in the separation zone.
Ban and Choi (2022)	CFD	Sharp-crested weir	The role of instantaneous flow behaviors than time-averaged ones in flow patterns

3.2 Local scour by horizontal wall jet flow

Local scouring induced by the action of wall jet flow near hydraulic structures has been of primary interest due to its potential to cause structural failure. The scour due to 2D horizontal wall jet flow was examined by Laursen (1952), Tarapore (1956), and Hogg et al. (1997). Chatterjee and Ghosh (1980) investigated the velocity distribution of wall jet flow as it develops over the apron and subsequent scour hole. Hassan and Narayanan (1985) examined the flow structure and similarity of scour profiles downstream from an apron caused by a submerged wall jet. They suggested a semi-empirical relationship based on the mean velocity within the scour hole to estimate the changes in scour depth over time. Ali and Lim (1986) proposed several different equations to characterize the flow structures, scour volume, and time-dependent scour holes caused by two-dimensional and three-dimensional jets. Johnston (1990) investigated the scour hole developed by a plane jet entering shallow tailwater conditions through laboratory experiments. He identified three distinct scour hole regimes, with two involving the jet permanently attaching to either the bed or the free surface boundary, and the third occurring when the jet alternates between the two boundaries. Chatterjee et al. (1994) conducted numerous laboratory experiments on various sluice openings and jet velocities for two different grain sizes. They discovered relationships that estimate the dimensions of a scour hole, such as maximum depth and location, based on time, discharge velocity, jet diameter, and mean grain size. It was revealed that the scour rate is significantly higher during the first few minutes and slower as scouring continues. They found that the scour depth increased with the increase of the flow velocity and the diameter of the jet. Hoffmans (1998) investigated

the equilibrium scour process caused by both plunging and horizontal jets without bed protection. Using Newton's second law, he derived relations to predict the maximum scour depth in the equilibrium state. Dey and Westrich (2003) carried out several experiments with cohesive sediment for various sluice openings, jet velocities, and apron lengths to investigate the time variation of scour hole and flow characteristics of the quasi-equilibrium state of scour of a cohesive bed. There was also an attempt to use CFD (Computational Fluid Dynamics) by Karim and Ali (2000) to examine flow and turbulence characteristics induced by a turbulent water jet impinging on a rigid surface and scoured bed. They used FLUENT based on various turbulence closure models to implement the flow field. The numerical results showed close agreement with relevant experimental data. Dey and Sarkar (2008) examined the mechanisms of the scour process by analyzing the velocity and turbulence intensity distributions across various stages of bed form evolution.

There have been several attempts to mitigate the local scouring behind a bed protection. Dey and Sarkar (2006) installed a launch apron behind the rigid apron to examine the scour reduction by the launch apron. The launching apron reduced scour depth by an average of 39%, with a maximum of 57.3% and a minimum of 16.2%. Although not directly related to scour reduction, Dey et al. (2010) investigated the flow velocity and turbulence by varying the velocity of the vertically injected water. In the presence of water injection, the wall shear stress and the rate of jet velocity decay were found to increase. Champagne et al. (2016a, b) examined the impact of air injection on scouring, considering variables such as air velocity, injection angle, diffuser width, diameter, and spacing, on the scouring process at a gated spillway with stilling basins. They varied the angle of air injection from -40 degrees (directed upstream) to 140 degrees (directed downstream) and found that scour

was significantly reduced at the vertical injection angle. This result indicates that deviating from the vertical injection angle does not contribute to further scour reduction. They confirmed that locally injected air in vertical direction at the end of apron reduced scour by approximately 59% near the structure. The work of Champagne et al. (2016b) is most closely related to the present study, as they also aimed to mitigate scouring through air injection. However, given that their research has not examined the flow and turbulence structures over the upstream bed and scour zone, further investigations are needed to better understand the physical mechanisms of flow alteration by air injection and its effect on the scour process. In addition, additional investigations must be conducted to determine the most effective amount and locations of air injection to identify the most efficient countermeasures against scouring. Table 2 summarizes the representative previous studies on scouring by horizontal wall jet flow.

Table 2. Previous studies on flow characteristics and scouring by horizontal wall jet flow.

References	Experiment	Method	Main findings
Chatterjee and Ghosh (1980)	Lab	-	Velocity distribution of wall jet flow over an apron and scour hole
Hassan and Narayanan (1985)	Lab	-	Flow structure and similarity of scour profiles downstream from an apron
Ali and Lim (1986)	Lab	-	Equations to characterize the flow structures, scour volume, and time-dependent scour holes
Johnston (1990)	Lab	-	Scour hole developed by a plane jet entering shallow tailwater conditions
Chatterjee et al. (1994)	Lab	-	Estimation the dimensions of a scour hole based on flow and sediment parameters
Hoffmans (1998)	Lab	-	Relations to predict the maximum scour depth in the equilibrium state based on Newton's second law
Karim and Ali (2000)	CFD	-	Flow velocities and shear stresses induced by a turbulent water jet over scoured bed
Dey and Westrich (2003)	Lab	-	Time variation of scour hole and the flow characteristics of the quasi-equilibrium state of scour of a cohesive bed
Dey and Sarkar (2006)	Lab	Launch apron	Reduction in the maximum scour depth by placing a launch apron downstream of the rigid apron
Dey and Sarkar (2008)	Lab	-	Flow structures of submerged jets in evolving scour hole downstream of an apron
Dey and et al. (2010)	Lab	Water injection	Reduction in bed shear stress in the presence of upward injection
Champagne et al. (2016a, b)	Lab	Air injection	The effect of air velocity, injection angle, diffuser width, diameter, and spacing on scouring

CHAPTER 4. METHODOLOGY

Turbulence fluctuation is characterized by random motion (small-scale eddies) and coherent structure (large-scale eddies). While the second-order moment of Gaussian probability distribution can describe the random motions, the coherent structures known as large-scale eddies or vortices have a life cycle including birth, development, interaction, and breakdown, whose evolutionary relations cannot be represented by means of conventional probabilistic tools, but by the higher-order moments. In addition, the large eddies have a significant contribution to the sediment behaviors downstream of the step geometry; on the other hand, the universal behaviors of smaller eddies need to be captured. These behaviors suggest that the LES technique is appropriate for the study of the interaction between turbulence and sediment transport. Moreover, the sediment movements are resolved by DEM, whose particles are advected according to the forces exerted by the instantaneous flow field. DEM has a significant advantage of being able to directly quantify kinetic properties of numerical sand grains, such as instantaneous particle velocity, particle-particle contact force, and particle-wall contact force. Using DEM, we can calculate the bedload transport rate based on each particle's instantaneous velocity and volume at any measurement points. It can be stated that DEM can provide a more accurate estimate of bedload transport rate in a direct way than conventional methods that can only describe a time-averaged value based on mean bed shear stress.

Therefore, in this study, a coupled LES-DEM model (Goniva et al., 2012) is employed to reproduce the instantaneous near-bed turbulence structures and sediment behaviors. The

three-dimensional hydrodynamics based on OpenFOAM (OpenCFD, L. T. D, 2009) are simulated using the LES approach to capture the large eddy motions by means of time-dependent, 3D Navier-Stokes equations. Meanwhile, the universal behaviors of smaller eddies (subgrid-scale) are solved by the Smagorinsky model (Smagorinsky, 1963). The numerical model is validated against experimental data to ensure its reliability.

4.1 Numerical simulation using OpenFOAM

OpenFOAM, an abbreviation for Open Field Operation and Manipulation, is an esteemed open-source Computational Fluid Dynamics (CFD) software (OpenCFD, L. T. D, 2009). OpenFOAM numerically solves the governing equations of fluid dynamics, primarily the Navier-Stokes equations for momentum conservation and the continuity equation for mass conservation. Depending on the problem's complexity, it may also solve additional equations like energy or species transport equations.

One of the general aspects of OpenFOAM is the discretization of the governing equations using the Finite Volume Method (FVM), which converts the continuous domain into a finite number of control volumes, thereby transforming the partial differential equations into algebraic equations. This discretization is closely linked to mesh generation, where the computational domain is divided into polyhedral cells, and the quality of this mesh is vital for solution accuracy and stability. OpenFOAM supports structured and unstructured meshes and offers users a wide array of discretization schemes such as upwind schemes, central differencing, and QUICK to tailor the approach to the

simulation's needs. Alongside mesh generation, defining appropriate boundary conditions is essential. OpenFOAM provides various boundary conditions for different field variables with the choice depending on the physical problem and domain geometry.

After laying the foundation through discretization and boundary conditions, selecting a suitable solver is imperative. OpenFOAM features an extensive solver library catering to different fluid flow problems, from incompressible to compressible and laminar to turbulent flows. When dealing with turbulent flows, OpenFOAM offers a selection of turbulence models, such as Reynolds Averaged Navier-Stokes (RANS) turbulence closure models, and Large Eddy Simulation (LES). Choosing a turbulence model involves considering the trade-offs between accuracy and computational cost.

Determining numerical time step is another integral component, especially for transient simulations. OpenFOAM covers both steady-state and transient simulations, offering various time discretization options. Additionally, it incorporates iterative solution algorithms and linear equation solvers. In this study, Pressure Implicit with Splitting of Operators (PISO) algorithm is used to reproduce the unsteady flows. The interFoam solver is designed to solve problems involving unsteady, incompressible flow where the phases are immiscible and the shape of the interface is of interest. The PISO algorithm is in conjunction with the Volume of Fluid (VOF) method, which is a widely used method for interface capturing or tracking in multiphase flows. The behaviors of air, water, and sediment can be described using the coupled model between the interFoam solver and DEM. A detailed description of coupling is in Chapter 4.3 and Chapter 4.4.

4.2 Large Eddy Simulation (LES)

The governing equations of the LES model are achieved by spatially filtering the Navier-Stokes equations over the finite grid domain. The turbulence scales larger than the filter width are directly resolved, and the smaller eddies are modeled with the assumption of isotropic turbulence. Considering the interaction with the sediment phase, the spatially filtered continuity equation and Navier-Stokes equations are written as follows:

$$\frac{\partial(\rho n_f)}{\partial t} + \nabla \cdot (\rho n_f \bar{\mathbf{u}}) = 0 \quad (1)$$

$$\frac{\partial(\rho n_f \bar{\mathbf{u}})}{\partial t} + \nabla \cdot (\rho n_f \bar{\mathbf{u}} \bar{\mathbf{u}}) = -n_f \nabla \bar{p} + \nabla(n_f \bar{\boldsymbol{\tau}}) + \mathbf{R}_{fp} \quad (2)$$

$\bar{\mathbf{u}}$ and \bar{p} denote the resolved flow velocity vector and pressure respectively; ρ is the fluid density. n_f is the volume fraction occupied by the fluid defined as below:

$$n_f = 1 - \sum_{i=1}^{N_{pV}} V_{pi} = (V_w + V_a) / V \quad (3)$$

where N_{pV} is the number of particles included in local cell volume V , and V_p is the volume occupied by DEM particles. V_w and V_a represent the volume occupied by water and air, respectively. \mathbf{R}_{fp} is the momentum exchange with sediment phase, which is described in detail in Chapter 4.3 below. The stress tensor $\bar{\boldsymbol{\tau}}$ is defined as follows:

$$\bar{\boldsymbol{\tau}} = (\mu_{\text{eff}})(\nabla \bar{\mathbf{u}} + (\nabla \bar{\mathbf{u}})^T) \quad (4)$$

where $\mu_{\text{eff}} = \mu + \mu_{\text{SGS}}$; μ and μ_{SGS} represent the dynamic viscosity of water and subgrid-scale (SGS) viscosity, respectively. As aforementioned, the well-known Smagorinsky model (Smagorinsky, 1963) is adopted for the SGS stress modeling. The spatial filtering

is conducted implicitly so that the filtering size is dependent on the local grid size. The grid filter width Δ is determined based on the local cell volume in such a way:

$$\Delta = \sqrt[3]{\Delta x \Delta y \Delta z} \quad (5)$$

where $\Delta x, \Delta y$, and Δz are local grid sizes in x , y , and z directions; μ_{SGS} is quantified based on the SGS length scale l_{SGS} and resolved strain tensor $\bar{\mathbf{S}}$, as follows:

$$\mu_{SGS} = \rho l_{SGS}^2 |\bar{\mathbf{S}}|, \quad l_{SGS} = C_s \Delta \quad (6)$$

where the Smagorinsky constant C_s is defined as 0.173 according to Lilly (1966) and Pope (2000) based on the following relationship:

$$C_s = \frac{1}{\pi} \left(\frac{2}{3C_\kappa} \right)^{\frac{3}{4}} \quad (7)$$

where $C_\kappa = 1.5$ is the Kolmogorov constant. However, the Smagorinsky model has the inherent disadvantage that μ_{SGS} is sometimes overestimated near a wall boundary. To solve this, the following Van Driest wall damping function is applied to the nearby cells of wall boundaries:

$$l_{SGS} = \min(\kappa y D, C_s \Delta) \quad (8)$$

where κ and y represent Von Kármán constant, defined as 0.41, and the wall normal distance, respectively. D is a function that accounts for the viscous effect near a wall, defined as:

$$D = 1 - \exp\left(-\frac{y^+}{A^+}\right), \quad y^+ = \frac{y u^*}{\nu} \quad (9)$$

where the model constant A^+ is determined as 26, as suggested by Van Driest (1956), and y^+ represents the dimensionless wall distance. u^* is referred to as the friction velocity. By adopting the wall damping function, the eddy viscosity becomes smaller in the buffer layer and subsequently almost zero in the sub-viscous layer.

The numerical procedure to solve the pressure-velocity coupling is based on the Pressure Implicit with Splitting of Operators (PISO) algorithm with the Gaussian interpolation for cell-centered data. The first order backward scheme is used for time discretization, and the second-order schemes are applied to spatial discretization. A blended scheme between the linear-upwind and central scheme is used for the flow velocity. For diffusive flow properties, the central scheme is applied. The numerical time step is maintained as 10^{-4} s for the whole simulation time to keep the Courant number less than 0.4 for all the numerical cells throughout the computational domain. A validation of the LES model against various experimental results is presented in Chapter 6.

4.3 Coupling of LES and DEM

The behaviors of numerical sediment grains are determined by the force of surrounding fluid, and the position and state of motion of the particles affect the fluid field again. The interaction of flow and sediment phases is reproduced through the LES-DEM coupling method. The movements of particles are governed by following DEM:

$$m_p \frac{du_p}{dt} = F_{pn} + F_{pt} + F_{pd} + F_{pp} + F_{pv} + F_{pb} \quad (10)$$

$$I_p \frac{d\omega_p}{dt} = \mathbf{r}_p \times \mathbf{F}_{pt} + \mathbf{T}_{pr} \quad (11)$$

where \mathbf{u}_p is the particle velocity and m_p is the particle mass. \mathbf{u}_p and ω_p are respectively the translational and angular particle velocity. I_p represents the angular moment of inertia. \mathbf{F}_{pn} and \mathbf{F}_{pt} denote the normal contact force and tangential contact force of the numerical particles, respectively; \mathbf{F}_{pp} and \mathbf{F}_{pv} represent the pressure and viscous force exerted on the particles, respectively. \mathbf{F}_{pb} mainly consists of the body force due to the gravitational acceleration \mathbf{g} . \mathbf{F}_{pd} is the drag force calculated based on the relative velocity between the fluid and particles. \mathbf{T}_{pr} is the rolling friction torque. The components of forces in Eqs (10) and (11) are defined as follows:

$$\mathbf{F}_{pn} = -k_{pn}\Delta\mathbf{x}_p + c_{pn}\Delta\mathbf{u}_{pn} \quad (12)$$

$$\mathbf{F}_{pt} = \min \left\{ \left| k_{pt} \int_{t_0}^t \Delta\mathbf{u}_{pt} dt + c_{pt}\Delta\mathbf{u}_{pt} \right|, \mu_{pc}\mathbf{F}_{pn} \right\} \quad (13)$$

$$\mathbf{F}_{pp} = -V_p \nabla p \quad (14)$$

$$\mathbf{F}_{pv} = -\nabla \cdot (\boldsymbol{\tau}) V_p \quad (15)$$

$$\mathbf{F}_{pb} = m_p \mathbf{g} \quad (16)$$

$$\mathbf{T}_{pr} = \mu_r |\mathbf{F}_{pn}| \frac{\omega_{pij}}{|\omega_{pij}|} \quad (17)$$

Here, $\Delta\mathbf{x}_p$ is the overlap distance of particles; $\Delta\mathbf{u}_{pn}$ and $\Delta\mathbf{u}_{pt}$ are referred to the normal and tangential relative velocity at the contact position, respectively. k_{pn} and k_{pt} denote the normal and tangential spring stiffness; c_{pn} and c_{pt} represent the normal and tangential

damping coefficients; t and t_0 are the simulation and initial times, respectively. μ_{pc} and μ_r represent the coulomb and rolling friction coefficient, respectively. V_p denotes the particle volume. ω_{pij} is the relative angular velocity between the i and j -th particles.

The fluid-particle momentum exchange \mathbf{R}_{fp} in Eq. (2) is mostly calculated by means of the drag force, which is defined as follows:

$$\mathbf{R}_{fp} = \mathbf{K}_{fp}\mathbf{u} - \mathbf{K}_{fp}\mathbf{u}_p \quad (18)$$

where \mathbf{K}_{fp} is defined as follows:

$$\mathbf{K}_{fp} = -\frac{\left|\sum_{i=1}^{N_p V} \mathbf{F}_{pd}\right|}{V|\mathbf{u} - \mathbf{u}_p|} \quad (19)$$

Here, V denotes the local cell volume, and the drag force \mathbf{F}_{pd} is determined based on the relative velocity of fluid and particle by the theory of Di Felice (1994) as below:

$$\mathbf{F}_{pd} = \frac{1}{8}C_d\pi d_p^2\rho n_f^2|\mathbf{u} - \mathbf{u}_p|(\mathbf{u} - \mathbf{u}_p)n_f^{-\chi} \quad (20)$$

The components of Eq (20) are defined as follows:

$$C_d = \left(0.63 + 4.8/\sqrt{Re_p}\right)^2 \quad (21)$$

$$Re_p = \frac{n_f d_p |\mathbf{u} - \mathbf{u}_p|}{\nu} \quad (22)$$

$$\chi = 3.7 - 0.65\exp\left[-(1.5 - \log Re_p)^2/2\right] \quad (23)$$

where ν and d_p are the kinetic viscosity of water and particle diameter; χ and Re_p denote an empirical coefficient and the particle Reynolds number, respectively. C_d is the drag coefficient applied to each sediment grain.

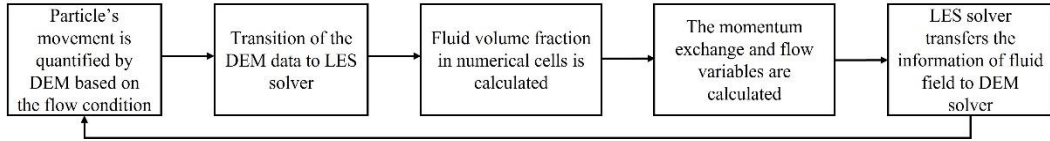


Figure 6. Coupling algorithm between LES and DEM

Figure 6 briefly illustrates the coupling process between flow and particles. First, the DEM solver computes particle movement using Eqs (10) and (11), based on initial fluid conditions, and transfers the particle data to the LES solver. Subsequently, DEM particles' properties, such as velocities and positions, are relayed to the LES solver. The LES solver then identifies the numerical cells containing the DEM particles and calculates the fluid volume fraction, n_f , using Eq (3). Following this, the LES solver computes the momentum exchange, \mathbf{R}_{fp} , and flow variables based on the fluid governing equations, Eqs (1) and (2). Finally, the LES solver conveys the fluid field information back to the DEM solver, enabling the particles to be repositioned according to the updated fluid field. More details about the LES-DEM coupling used in this study can also be found in Goniva et al. (2012).

The time step of updating the sediment movements is chosen as 10^{-5} s so that the coupling between the LES and DEM is implemented every 10 steps of DEM. The good agreement with experimental data confirms the performance of the LES-DEM coupling, which is presented in Chapter 6.

4.4 Incorporation of air phase into LES-DEM model

It is crucial to take into account the effect of the air phase on the flow structure and sediment transport process in wall jet flow because the water surface fluctuates significantly due to the high Froude number. Furthermore, implementing air flow is essential to investigate the influence of air injection on the scouring process. In this context, the two-phase LES-DEM model described in Chapter 4.3 is extended to incorporate air phase based on Volume of Fluid (VOF) method. The VOF method is a popular method for multiphase flow simulation where two or more immiscible fluids are involved, such as water and air. The fluid density ρ is calculated considering the volume fraction of each fluid phase as follows:

$$\rho = \rho_w n_w + \rho_a n_a = \rho_w n_w + \rho_a (1 - n_w) \quad (24)$$

where ρ_w and ρ_a represent the density of water and air; n_w and n_a denote the volume fractions of water and air, respectively. n_w and n_a can range from 0 to 1, and their sum is always 1 in a numerical cell by the VOF model. The effect of the air phase on the drag force, presented in Eq. (20), is reflected through the mixed ρ , presented in Eq (24). Based on Eq. (20), it can be inferred that when the volume fraction of air is dominant in a local numerical cell, it does not contribute significantly to sediment transport due to its low ρ .

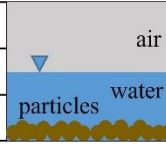
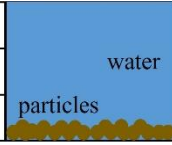
$n_f = 1$	air	$0 < n_f < 1$		$0 < n_f < 1$	
$n_w = 0$		$0 < n_w < 1$		$n_w = 1$	
$n_a = 1$		$0 < n_a < 1$		$n_a = 0$	

Figure 7. Schematic illustration of the fluids (water and air) and sediment based on the volume fraction in a numerical cell.

Figure 7 depicts the varying conditions of volume fractions within a numerical cell. When a numerical cell is fully occupied by air, the water volume fraction, n_w , becomes 0, and the air volume fraction, n_a , becomes 1. If there are no sediment particles in the cell, the fluid volume fraction, n_f , becomes 1. In cases where an air phase is present in a numerical cell and the cell is occupied by particles or a portion of a single particle, the fluid volume fraction takes a value between 0 and 1. Similarly, the volume fractions of water and air range between 0 and 1. Since the value of n_f is dependent on the volume of the particles, the coupling model inherently incorporates the influence of different particle sizes. When only water and particles are present in the numerical cell, the fluid volume fraction, n_f , takes a value between 0 and 1, while the water fraction n_w becomes 1 due to the absence of air.

The VOF model typically solves an advection equation for the volume fraction n_f , and this equation is fundamental to the method. The equation follows the principle of conservation of mass for the fluid phase. The generic form of the advection equation is as follows:

$$\frac{\partial(n_f n_w)}{\partial t} + \nabla \cdot (n_f n_w \bar{\mathbf{u}}) + \nabla \cdot (n_f n_w (1 - n_w) \bar{\mathbf{u}}_r) = 0 \quad (25)$$

where $\bar{\mathbf{u}}_r$ is the relative velocity vector between water and air. The last term in the left side only serves to capture the interface of the two fluid phases. This equation states that the rate of change of the volume fraction of a fluid phase within a control volume must be balanced against the net flux of the phase's volume fraction across the control volume boundaries. This notion adheres to the principles of a typical conservation law. This advection equation is typically discretized and solved using a method that can maintain the sharp interface between the phases. In OpenFOAM, a method called MULES (Multidimensional Universal Limiter for Explicit Solution) is often used for this purpose. It should be noted that in the VOF model, the physical properties such as density and viscosity are calculated based on the volume fraction of each fluid.

4.5 Measurement of reattachment length

The mean streamwise velocity U in the cell center at each first cell from the bottom boundary with $y^+ < 1$ is numerically calculated. Then the exact position in streamwise coordinate where the U changes from negative to positive value is found.

4.6 Visualization of vortex structure

The large-scale vortex structures are numerically visualized using the Q-criterion first suggested by Hunt et al. (1988) as:

$$Q = \frac{1}{2} \left(\|\Omega_{ij}\|^2 - \|S_{ij}\|^2 \right) \quad (26)$$

where the strain rate tensor S_{ij} and the rotation rate Ω_{ij} are respectively defined as:

$$S_{ij} = \frac{1}{2} \left(\frac{\partial u_i}{\partial x_j} + \frac{\partial u_j}{\partial x_i} \right), \quad (27)$$

$$\Omega_{ij} = \frac{1}{2} \left(\frac{\partial u_i}{\partial x_j} - \frac{\partial u_j}{\partial x_i} \right) \quad (28)$$

$Q > 0$ represents the existence of a vortex. According to the definition, the Q criterion defines vortices as areas where the vorticity magnitude is greater than the magnitude of the rate of strain.

4.7 Bedload transport rate

The depth-integrated and time-averaged bedload transport rate Q_x is defined as follows:

$$Q_x = \frac{1}{T} \int \sum_{l=1}^{N_p} V_p u_{pl} / A_h dt \quad (29)$$

where T represents the period of averaging, and N_p is the total number of sediment particles in a measurement area. V_p and u_{pl} denote the particle volume and individual particle's velocity, respectively. l is the index of each particle. A_h and dt denote the measurement area and time interval of measurement, respectively. The individual shape of grains is assumed to be spherical throughout this study.

4.8 Quadrant analysis for flow structure

The quadrant analysis approach, which was first suggested by Lu and Willmarth (1973), was used to investigate the turbulent flow structures near the bed. The u' , v' pairs are divided into four quadrants according to their sign as below:

I_1 : Outward interaction ($u' > 0, v' > 0$)

I_2 : Ejection event ($u' < 0, v' > 0$)

I_3 : Inward interaction ($u' < 0, v' < 0$)

I_4 : Sweep event ($u' > 0, v' < 0$)

Here, I_1 and I_3 contribute negatively to the Reynolds stress $-\langle u'v' \rangle$, while I_2 and I_4 positively contribute to it. A sorting function I is introduced to distinguish each quadrant. In this study, we let I_i be the i -th quadrant. I_i is defined as one if it is in the i -th quadrant, and zero otherwise. Thereby, the ratio of time occupied by each turbulence event in the i -th quadrant, denoted as P_i , is defined as follows:

$$P_i = \frac{\int I_i(t)dt}{T} \quad (30)$$

where T and dt are the total simulation time and time interval of measurement, respectively.

4.9 Quadrant analysis for bedload transport

The weighted-quadrant analysis technique, initially proposed by Nakagawa and Nezu (1981), was utilized to examine the interaction between the turbulent flow structures and sediment behaviors. The weighted-quadrant analysis quantifies the interaction between a fluctuating flow field and any variable of interest by weighting the frequency of the flow velocity with the interested variable. In this study, the instantaneous bedload transport rate q_x is determined as the variable of interest. In the quadrant analysis for bedload transport, the ratio of bedload transport rate during each turbulence event in the i -th quadrant, denoted as P_{qi} , is quantified as following manner:

$$P_{qi} = \frac{\int |q_x(t)| I_i(t) dt}{\int |q_x(t)| dt} \quad (31)$$

where q_x is the instantaneous bedload transport rate.

CHAPTER 5. Computational Setup and Application

5.1 Surface jet flow behind various inclined BFSs

The schematic illustration of the computational domain for numerical simulations is shown in Figure 8. The numerical domain was constructed with reference to Nelson et al. (1995), in which only perpendicular step angle was used. In this thesis, various inclined BFSs are constructed by adjusting the step angle α , as shown in Figure 8. A range of step angles, namely 10° , 20° , 30° , and 90° , were carefully selected for consideration in this study. These angles were chosen to encompass a variety of flow separation trends. By incorporating these different step angles, it is aimed to capture a comprehensive understanding of the flow and turbulence structures around the various inclined BFSs. The step height, denoted as H , has a value of 0.04m, according to Nelson et al. (2005). The height of the upstream and downstream channels of the BFS are denoted as ℓ_u and ℓ_d , respectively. The Reynolds number (Re) and expansion ratio (ER) are respectively defined as $\frac{U_o \ell_u}{\nu}$ and $\frac{\ell_d}{\ell_u}$, where U_o represents the time-averaged, maximum velocity on the longitudinal centerline at the step edge ($x = 0$). The origin of the coordinate system is located downside of the step edge, at the center of the spanwise direction. The reattachment length x_r is defined as the distance from the step edge, where $x = 0$, to the end of the separation zone boundary. The reattachment point is determined where the mean streamwise velocity changes from negative to positive sign at the vicinity of the bed. x_b in

Figure 8 represents the horizontal width of the step, varying with the BFS angle; $x_b = 0$ for $\alpha = 90^\circ$. The length scales in x, y, and z directions of the computational domain are $80H$, $5H$ (downstream of the step), and H , respectively.

The inlet boundary is located at $x = -50H$, which is sufficiently far away on the upstream of the BFS for the flow to be fully developed. A constant flow velocity is uniformly imposed at the inlet boundary based on the Reynolds number. The bottom boundary is treated as a wall boundary where the no-slip condition is applied. At the bottom boundary downstream of the BFS, the channel is covered with 2 mm thickness of uniform sand (diameter of 0.9 mm). The kinematic properties of fluid and sediment near the interface are determined by the LES-DEM coupling, as delineated in Chapter 4.3. The wall damping function shown in Eq (8) is applied to all the wall boundaries, whereby the Neumann boundary condition with zero-gradient is applied to pressure. The top boundary is constructed as a rigid lid on which slip boundary condition is applied. The application of the rigid-lid approximation can be deemed reasonable when the Froude number (Fr) is not large, such as $Fr < 0.4$ (Blanckaert and De Vriend, 2004). At the outlet boundary, located at $x = 30H$, the pressure is uniformly fixed as zero. Meanwhile, the Neumann boundary condition with zero-gradient is set at the outlet boundary for the flow velocity. The periodic boundary condition is applied on the side boundaries for all the flow variables to obtain the two-dimensionality of the flow at the centerline of the flow direction.

The vertical grid size near the bed is determined to be fine enough to capture the size of the sediment grains. We also identified that the vertical grid size above the topmost sand grains is fine enough with $y^+ = 0.8$; this y^+ value falls within the range of viscous sublayer

($0 < y^+ < 5$) as suggested by Pope (2000). This finer grid resolution in the vicinity of the interface between flow and sediment grains is to ensure accurately reproduction of the flow behavior in the inner boundary layer. The total number of grids is 2,384,840, and the aspect ratio is maintained below four throughout the computational domain.

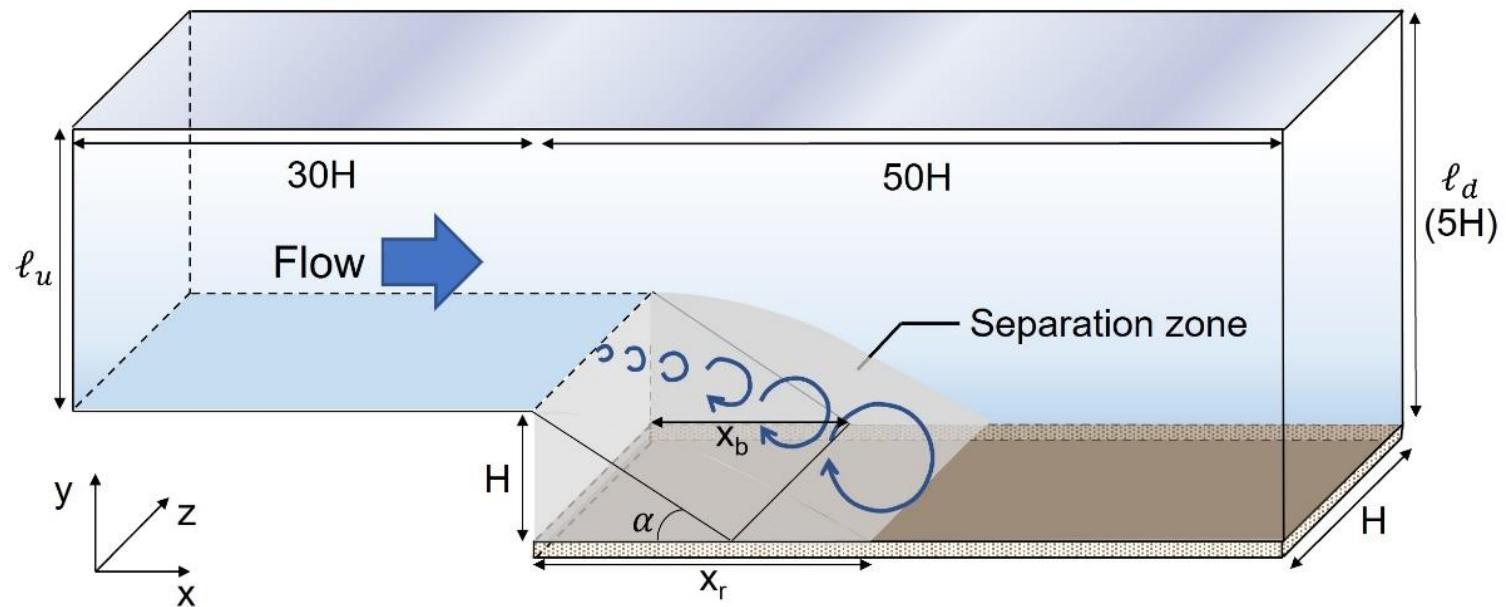


Figure 8. Schematic diagram of the computational domain with various inclined BFSs (diagram is not to the scale).

The total number of particles used in the numerical simulation is 92,233. As aforementioned, this study extends the work of Nelson et al. (1995) to cover various inclined BFSs to investigate the effect of BFS angles on near-bed flow structures and sediment behaviors in surface jet flow. The configuration of the numerical simulations is summarized in Table 3.

Table 3. Configuration of the numerical simulation for surface jet flow.

Run	x_b/H	Re	ER	Fr	α (°)	ρ_s (kg/m ³)	d_{50} (mm)
CaseN10	5.671	64000	1.25	0.33	10	2650	0.9
CaseN20	2.748				20		
CaseN30	1.732				30		
CaseN90	0				90		

5.2 Submerged wall jet flow with air injection behind sluice gate

In this study, an experimental case from Chatterjee et al. (1994), which addresses the local scouring process caused by submerged wall jet flows, is selected to construct a numerical domain. There are two benefits to conducting numerical simulations based on their experimental case: first, the apron geometry is simple to numerically implement the wide-area air injection; second, the validation of the LES-DEM model for the local scour profile is possible based on the empirical formula suggested by their study.

The computational domain for the wall jet flow induced by the opening of a sluice gate is illustrated in Figure 9. The height of the gate is denoted as a . The length of apron is defined as L . B represents the length of the sediment packing. The vertical length and width

of the flume are labeled D and W, respectively. The height of BFS is denoted as h . Initially, sediment fills up to this height. The total number of particles used in the numerical simulation is 6,909. The initial water depth is determined as $d_t = 0.31$ m according to the experiment of Chatterjee et al. (1994). Table 4 summarizes the length scales of the numerical experiment in this study. The origin of the coordinate system is located at the step edge (the end of apron), at the center of the spanwise direction. Table 5 summarizes the detail of the configurations of air injection. The number of air slots consist of three depending on the injection length RA (the length from $x = 0$). The air slots are placed on the apron boundary, arranged in 2 rows in the z direction. The ratio of air injection flow rate Q_a to the inflow water flow rate Q_w is determined as $Q_a/Q_w = 0.25, 0.5, \text{ and } 1$. Here, Q_a is calculated by summing all the airflow rate injected from each air slot. The ratio of the momentum of injected air, M_a , to that of inflowing water, M_w , is also summarized in Table 5. Whereas Q_a is calculated based on each air injection velocity and air injection area, M_a is derived from the square of this velocity and air injection area. Consequently, the ratio of momentum of air to that of inflowing water, M_a/M_w , decreases as the number of air slots increase, due to the reduced air injection velocity, as shown in the table. The air is vertically injected directly from the apron boundary without a need to establish any flow chambers. This approach allows for the examination of the sole effect of air injection on the flow, without any flow disturbances caused by such chambers. The spacing and diameter of the air inlets have been determined to be 3 mm and 7 mm, respectively.

The simulation domain omits the reproduction of the entire sluice gate and water on the left side of the gate to minimize unnecessary computational costs. However, a discharge

velocity $U_a = 2.42$ m/s is imposed on the inlet boundary, located on the left side of the domain, as schematized in Figure 9. The right side of the sluice gate surface is replaced with a wall boundary above the inlet. The apron upstream of sediment box is also treated as a wall boundary. The wall boundaries employ the same no-slip condition and wall damping function as described in Chapter 4.2. The top boundary is treated as an atmosphere, below which, a free water surface forms. The outlet boundary is located at $x = 3.66$ m, whereby the pressure is uniformly set to zero. The periodic boundary condition is applied on the side boundaries to avoid side wall effect. Reynolds number Re and Froude number Fr are 48,400 and 5.46, respectively, based on the inlet velocity as below:

$$Re = U_a a / \nu \quad (32)$$

$$Fr = U_a / (ga)^{0.5} \quad (33)$$

where U_a is the discharge velocity at the inlet; g is the gravitational acceleration.

Table 4. Length scale in the numerical domain.

a (m)	L (m)	h (m)	B (m)	D (m)	W (m)	d_t (m)
0.02	0.66	0.11	3.0	0.61	0.02	0.31

The numerical procedure to solve the pressure-velocity coupling is based on the Pressure Implicit with Splitting of Operators (PISO) algorithm with the Gaussian interpolation for cell-centered data. The first order backward scheme is used for the time discretization and the second order schemes are applied to the spatial discretization. A fixed blended scheme

between the linear-upwind and central scheme is used for the flow velocity. For diffusive flow properties, the central scheme is applied. The numerical time step is maintained as 10^{-4} s for the whole simulation time to keep the Courant number less than 0.4 for all the numerical cells throughout the computational domain.

The parallel computation was carried out by our High-Performance Computing (HPC) system, which is equipped with 224 cores of Intel Xeon Gold 6330 running at 2.3 GHz. The simulations employed a total of 128 cores and 16 GB of memory per core. OpenMPI was used for the parallelization. For reference, the numerical simulation of a surface jet flow over a perpendicular backward-facing step, comprising 2,384,840 numerical cells and 92,233 sediment particles, took approximately 10 days to simulate 60 s using parallel computation on our HPC system.

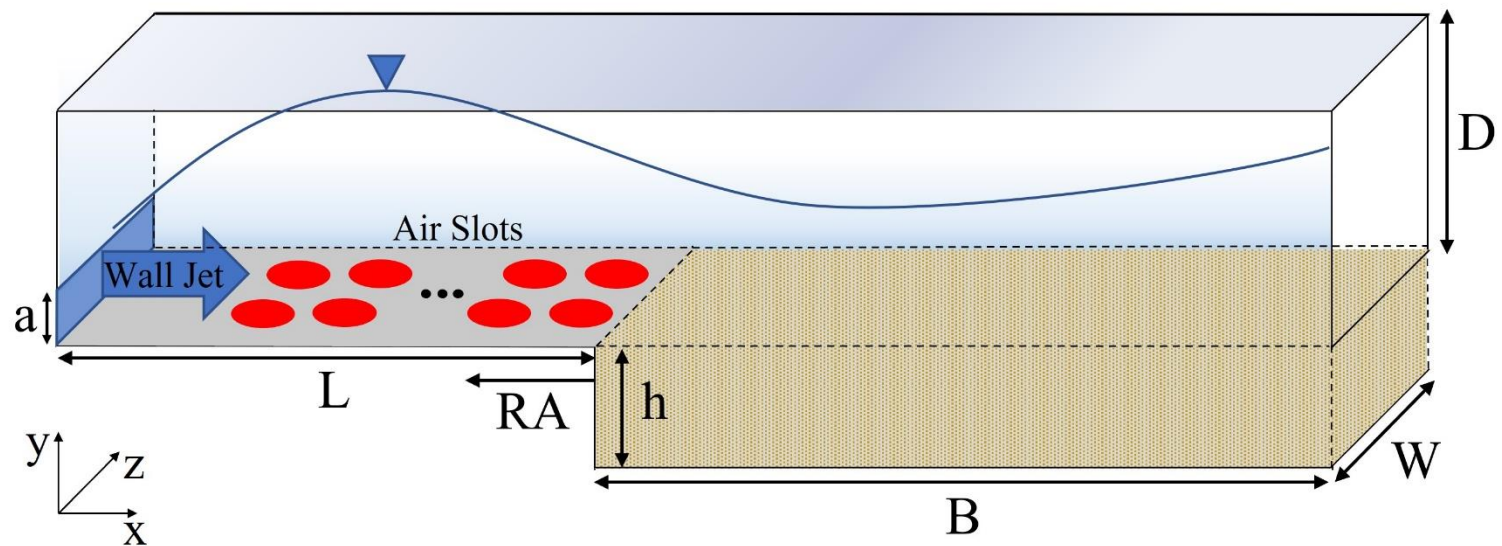


Figure 9. Schematic diagram of the computational domain for wall jet flow behind a sluice gate (diagram is not to the scale)

Table 5. Configuration of the numerical simulation for submerged wall jet flow.

Run	Air injection	RA (cm)	Air velocity (m/s)	M _a /M _w	Q _a /Q _w	Slots numbers (x × z)	Slot diameter (mm)	d ₅₀ (mm)
CaseNA	X	-	-	-	-	-	7	4.3
CaseRA2Q025	O	2	1.57	0.162	0.25	2 × 2		
CaseRA2Q05			3.14	0.648	0.5			
CaseRA2Q1			6.28	2.592	1.0			
CaseRA20Q025		20	0.157	0.016	0.25	20 × 2		
CaseRA20Q05			0.314	0.065	0.5			
CaseRA20Q1			0.628	0.259	1.0			
CaseRA40Q025		40	0.0785	0.008	0.25	40 × 2		
CaseRA40Q05			0.157	0.032	0.5			
CaseRA40Q1			0.314	0.13	1.0			

CHAPTER 6. MODEL VALIDATION

6.1 Validation against surface jet flow over BFS

The numerical tool was thoroughly validated against a wide range of measurement data obtained from various observations of the flow over BFSs under surface jet flow. First, the hydrodynamic model based on the LES approach is validated against the experimental data of Ruck and Makiola (1993) and Nakagawa and Nezu (1987). Secondly, the LES-DEM coupling model is validated against the observation of Nelson et al. (1995).

6.1.1 Validation of hydrodynamic model

As the Froude number is low ($Fr < 1$), many previous authors (Hincu and Finkelstein, 1963; Sumbal, 1966; Ljatcher and Prudovski, 1984; Faulhaber, 1983 & 1986; Nestmann and Bachmeier, 1987; Nestmann, 1992) have revealed that the flow characteristics between the hydrodynamic and aerodynamic models are quite similar. They have successfully applied the aerodynamic models for studying the river flows instead of using a hydrodynamic model. An advantage of an aerodynamic model (AD) over hydrodynamic model (HD) is that the experimental model can be easily built in small scales in the laboratory based on the Reynolds number similarity between aerodynamic and hydrodynamic models. Particularly, the research group at the Federal Waterways Engineering and Research Institute was very profitable in the application of AD to study the flow and bed-morphology of the Elbe River (Faulhaber, 1983 & 1986; Nestmann,

1992). In addition, the study on the fluctuation of the reattachment of the flow over a step in an open channel is successfully implemented by the duct flow (Eaton and Johnston, 1981; Ruck and Makiola, 1993).

The LES model was first validated against the measurement data obtained from the wind tunnel tests of Ruck and Makiola (1993). They measured the mean velocity, turbulence intensity, and reattachment length behind various inclined BFSs ($\alpha = 10^\circ, 15^\circ, 20^\circ, 25^\circ, 30^\circ, 45^\circ, 90^\circ$) with different expansion ratios (ER=1.48, 2.0, 3.27) and Reynolds numbers (Re=5000, 8000, 11000, 15000, 47000, 64000) using LDV. Figure 10-15 compare the simulated velocity component U/U_o , turbulence intensity $\left(\sqrt{\langle u'^2 \rangle}/U_o\right)^2$, and mean flow reattachment length x_r with the observation data. The values are normalized by the maximum streamwise velocity U_o , measured 2H upstream of the step edge ($x/H = -2$). For the sake of brevity, the streamwise and vertical turbulence intensities are denoted as $TI_x = \sqrt{\langle u'^2 \rangle}/U_o$ and $TI_y = \sqrt{\langle v'^2 \rangle}/U_o$, respectively. The comparisons for several representative high Reynolds numbers (Re=15,000, 47,000, and 64,000) and various BFS angles ($\alpha = 10^\circ - 90^\circ$) at ER=1.48 and 2 are briefly presented herein. As shown in these figures, the simulation results showed a good agreement to the measurement data, indicating that the 3D LES model can accurately reproduce the turbulent flow behaviors around the separation zone at various inclined BFSs. It can also be seen in the figures that the LES model precisely predicts the reattachment length x_r .

The performance of the hydrodynamic model was further validated against the observation data from a laboratory-scale open channel experiment conducted by Nakagawa and Nezu (1987). The experiment consists of a perpendicular BFS ($\alpha = 90^\circ$)

with $ER=1.23$ at $Re=99,750$. They measured the mean velocity, turbulence intensity profiles, and the reattachment length behind the BFS. Figure 16 compares the simulated flow velocity, turbulence intensity, and reattachment length with the observation data, reaffirming that the LES model can accurately capture the flow structures downstream of the BFS.

Table 6 provides the R-squared (R^2) and Root Mean Square Error (RMSE) (defined in Eqs (33) and (34) below) of the mean velocity and turbulence intensity to quantitatively evaluate the accuracy of the 3D LES model against the measurement data.

$$RMSE = \left[\sum_{i=1}^n \frac{(O_i - P_i)^2}{n} \right]^{0.5} \quad (34)$$

$$R^2 = \left[\frac{\sum_{i=1}^n (O_i - \bar{O})(P_i - \bar{P})}{\left[\sum_{i=1}^n (O_i - \bar{O})^2 \right]^{0.5} \left[\sum_{i=1}^n (P_i - \bar{P})^2 \right]^{0.5}} \right]^2 \quad (35)$$

where O_i and P_i denote the i -th observed and simulated values, respectively, while \bar{O} and \bar{P} are the averaged values of the observed and simulated data. In the two validation cases (Nakagawa and Nezu, 1987; Ruck and Makiola, 1993), the minimum R^2 value was found to be 0.812, and the maximum RMSE value was 0.137 for both mean velocity and turbulence intensity, implying that the hydrodynamic model performs very well in reproducing the separation flow field at various BFS angles.

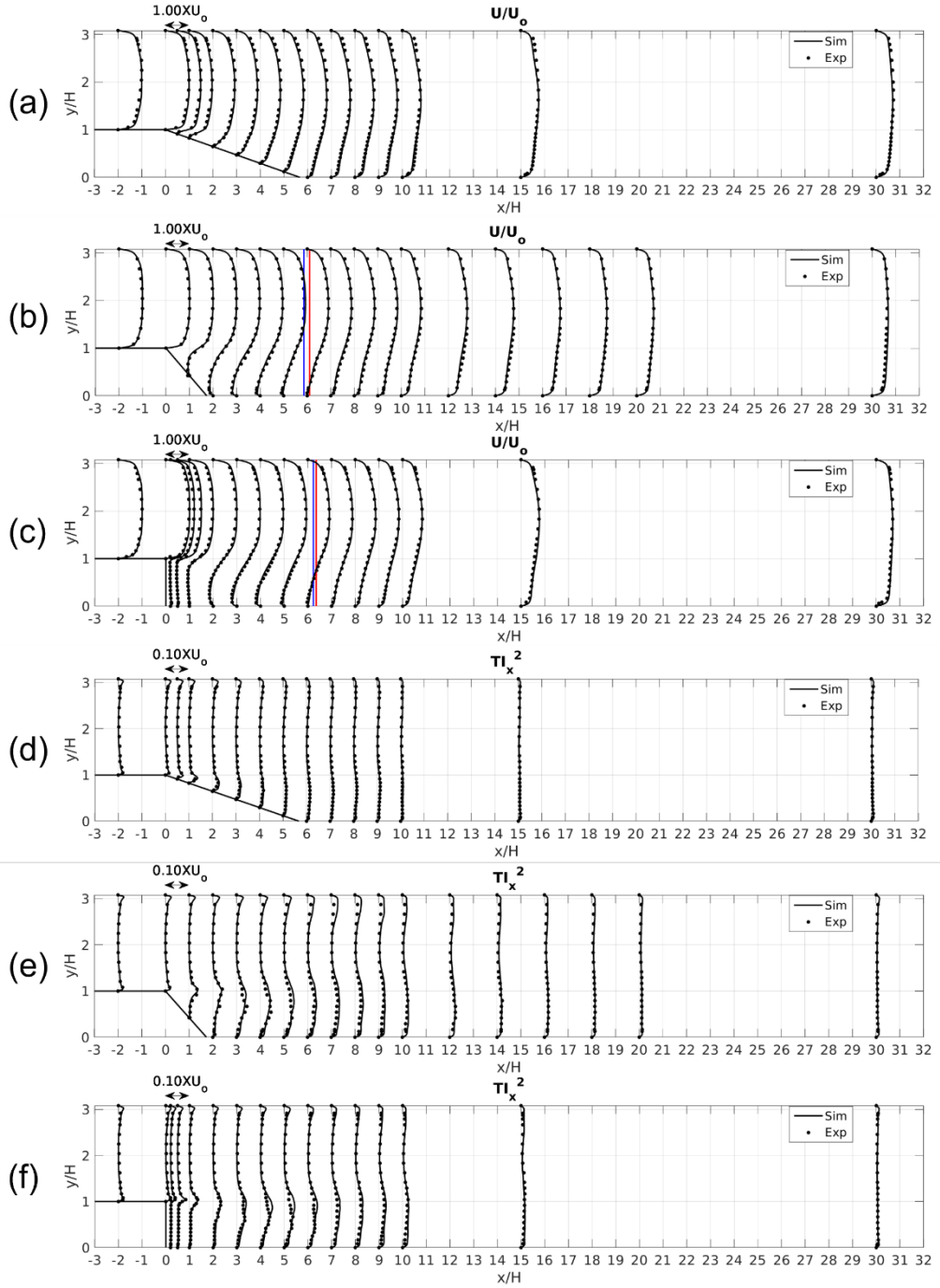


Figure 10. Streamwise velocity (a, b, c) and turbulence intensity (d, e, f) profiles behind the step at $Re=15000$, $\alpha = 10^\circ, 30^\circ, 90^\circ$, and $ER=1.48$ (Blue line is the location of reattachment point in the simulation; Red line in the experiment).

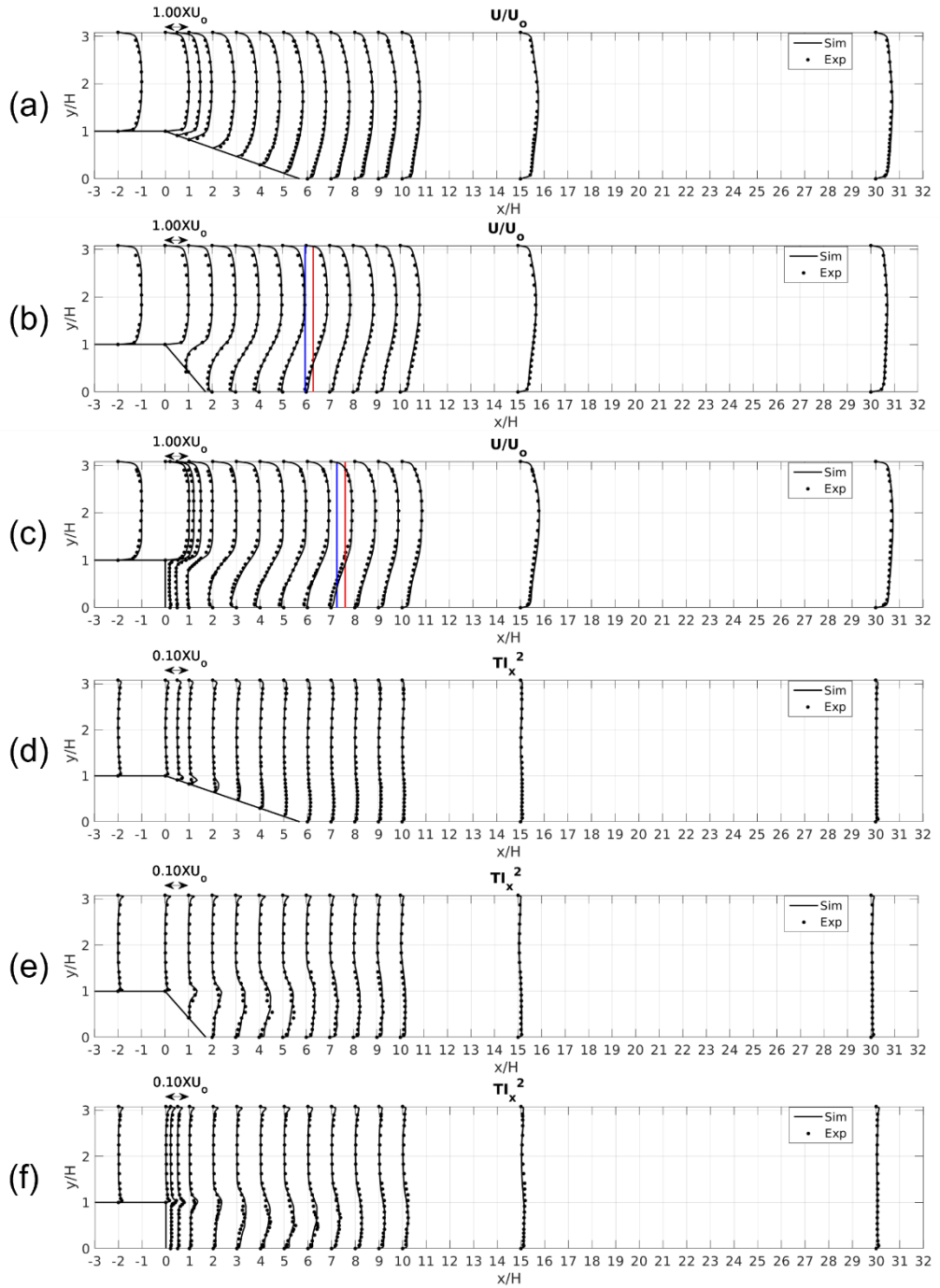


Figure 11. Streamwise velocity (a, b, c) and turbulence intensity (d, e, f) profiles behind the step at $Re=47000$, $\alpha = 10^\circ, 30^\circ, 90^\circ$, and $ER=1.48$ (Blue line is the location of reattachment point in the simulation; Red line in the experiment).

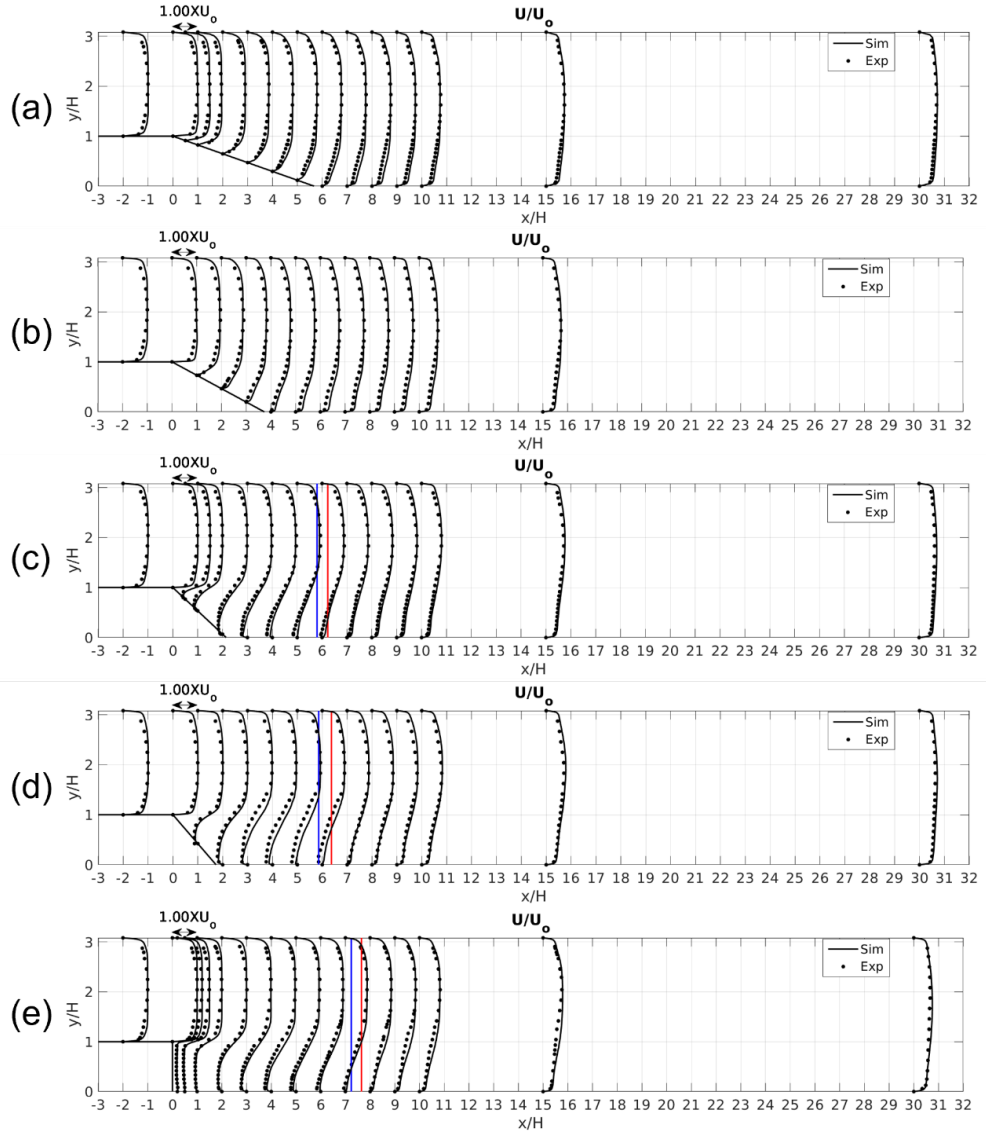


Figure 12. Streamwise velocity (a, b, c, d, e) profiles behind the step at $Re=64000$, $\alpha = 10^\circ, 15^\circ, 25^\circ, 30^\circ, 90^\circ$, and $ER=1.48$ (Blue line is the location of reattachment point in the simulation; Red line in the experiment).

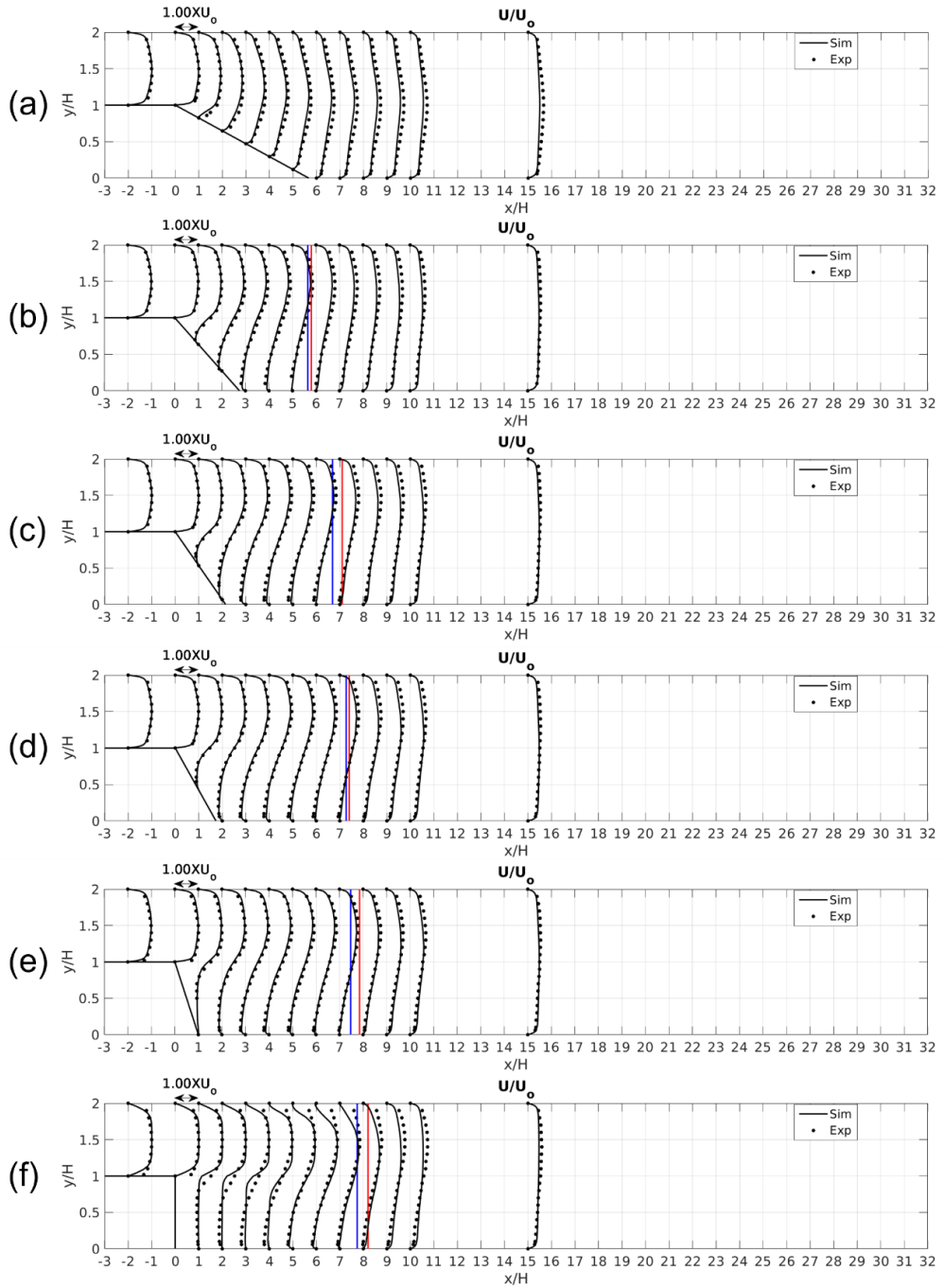


Figure 13. Streamwise velocity (a, b, c, d, e, f) profiles behind the step at $Re=15000$, $\alpha = 10^\circ, 20^\circ, 25^\circ, 30^\circ, 45^\circ, 90^\circ$, and $ER=2$ (Blue line is the location of reattachment point in the simulation; Red line in the experiment).

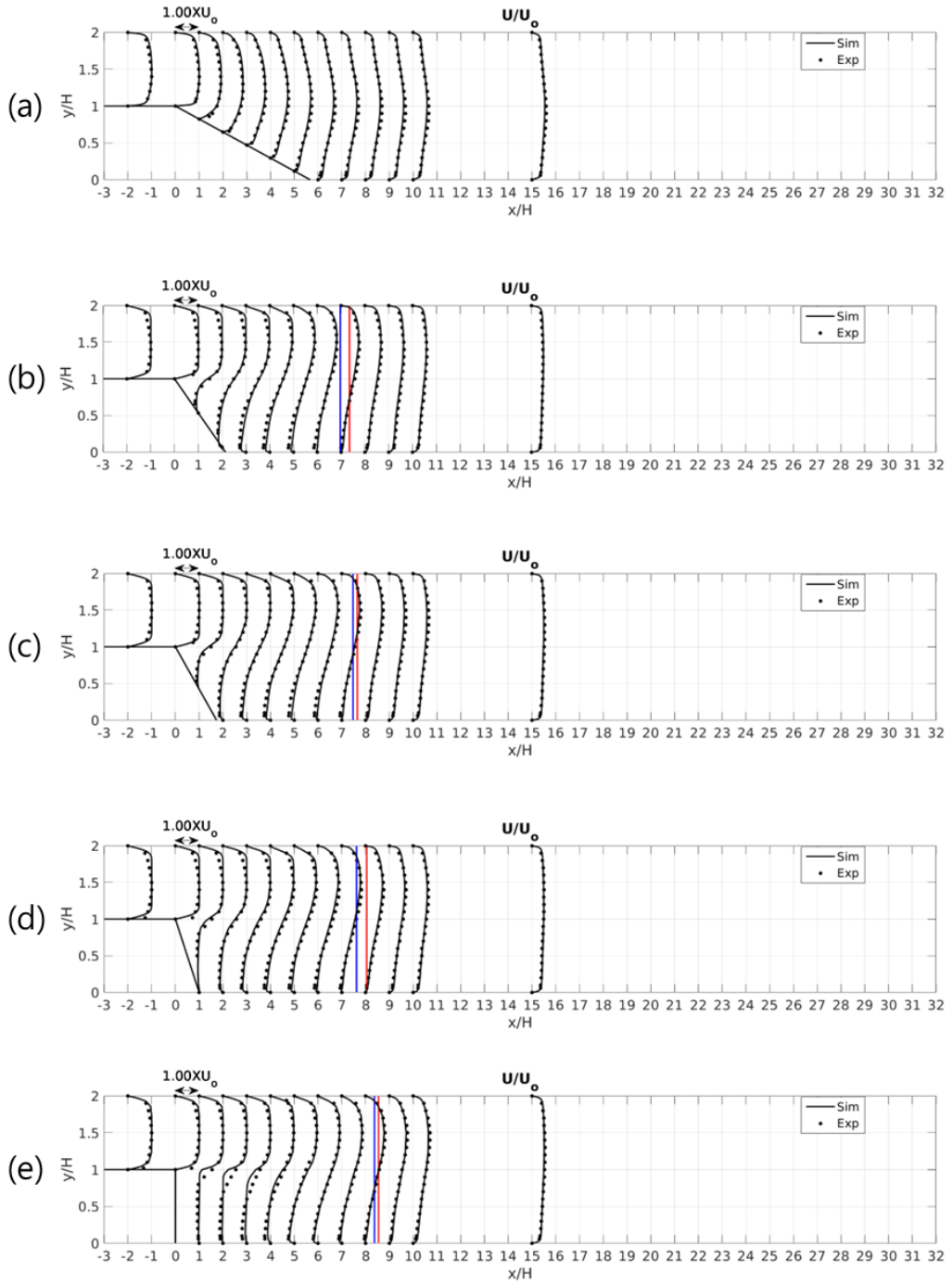


Figure 14. Streamwise velocity (a, b, c, d, e) profiles behind the step at $Re=47000$, $\alpha = 10^\circ, 25^\circ, 30^\circ, 45^\circ, 90^\circ$, and $ER=2$ (Blue line is the location of reattachment point in the simulation; Red line in the experiment).

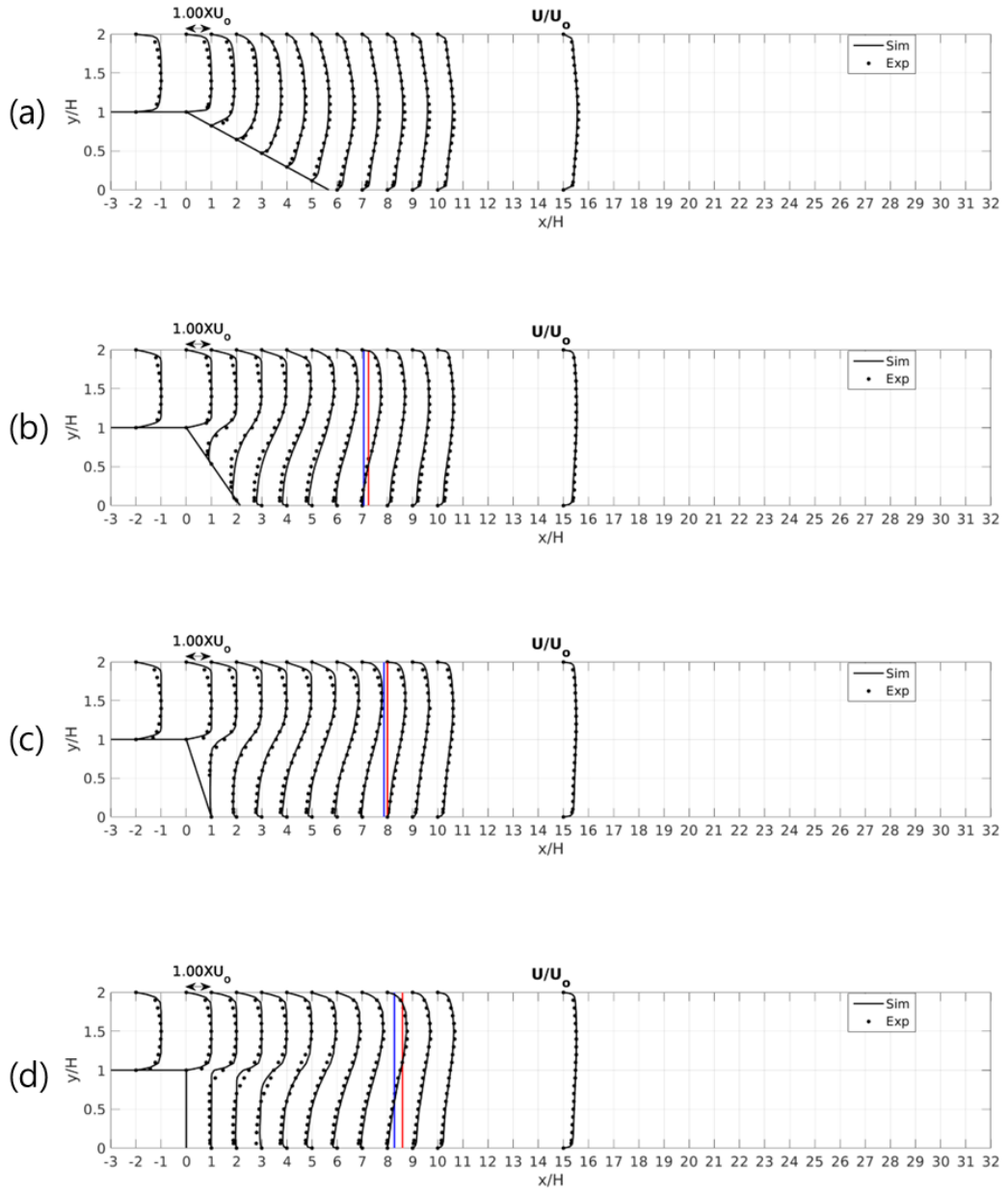


Figure 15. Streamwise velocity (a, b, c, d) profiles behind the step at $Re=64000$, $\alpha = 10^\circ, 25^\circ, 45^\circ, 90^\circ$, and $ER=2$ (Blue line is the location of reattachment point in the simulation; Red line in the experiment).

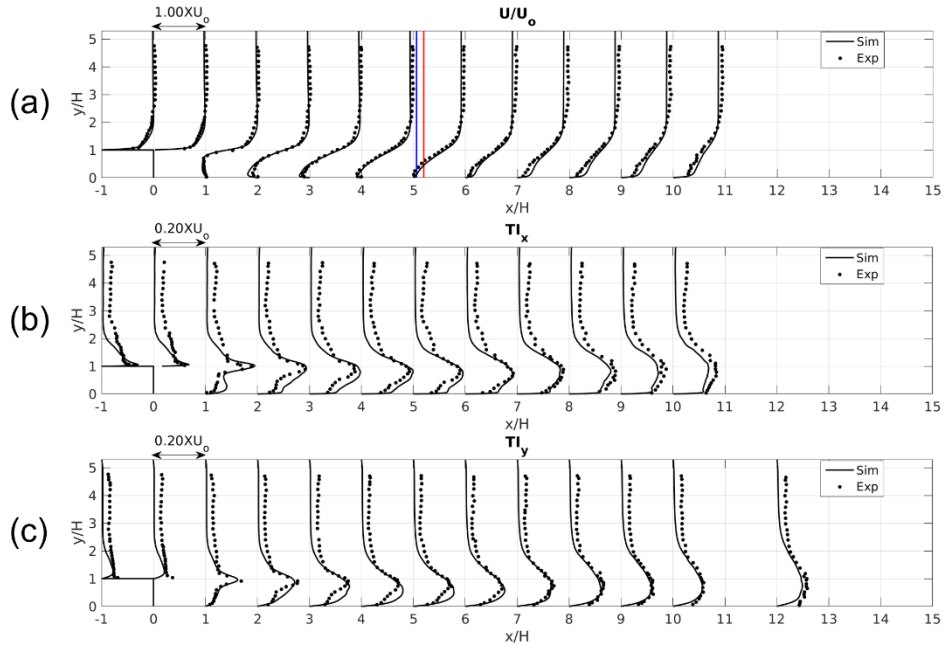


Figure 16. Streamwise velocity (a), streamwise turbulence intensity (b), and vertical turbulence intensity (c) profiles behind the step (Blue line is the location of reattachment point in the simulation; Red line in the experiment).

Table 6. R^2 and RMS values between the simulation results and experimental data from Ruck and Makiola (1993) and Nakagawa and Nezu (1987).

Experiment	Re	α ($^\circ$)	$R^2 \left(\frac{U}{U_0} \right)$	$R^2 \left(\frac{u'}{U_0} \right)$	$RMSE \left(\frac{U}{U_0} \right)$	$RMSE \left(\frac{u'}{U_0} \right)$
Ruck and Makiola (1993)	15000	10	0.959	0.817	0.096	0.037
	15000	30	0.977	0.932	0.077	0.023
	15000	90	0.970	0.865	0.097	0.035
	47000	10	0.961	0.812	0.098	0.042
	47000	30	0.978	0.902	0.092	0.029
	47000	90	0.9	0.922	0.085	0.078
Nakagawa and Nezu (1987)	99,750	90	0.832	0.873	0.137	0.096

6.1.2 Validation of LES-DEM coupling model

The validation of the LES-DEM coupling, delineated in Chapter 4.3, was confirmed by comparing the simulation results and observation data from Nelson et al. (1995). They conducted a laboratory experiment consisting of a recirculating acrylic plastic plume with a movable perpendicular BFS at $ER=1.25$ and $Re=64,000$ to investigate the effect of the near-bed turbulence structures due to flow separation on bedload transport rate. They used the sand grains with a mean diameter of 0.9 mm distributed behind the BFS. The sand density was 2650 kg/m^3 as general quartz. LDV and high-speed cinematography were respectively utilized to quantify the near-bed flow velocity and bedload transport rate at six different measurement points. The bedload transport rate was measured by counting the number of grains crossing a 0.01 m long lateral line for a certain time. They provided near-bed flow statistics and joint frequency distributions of fluctuating velocity pairs of u' and v' weighted by the instantaneous bedload transport rate q_x . In our numerical simulation, the sediment grains were packed from $y/H = -0.05$ to $y = 0$ downstream of $x = x_b$.

Figure 17 shows the comparison of U , $\sqrt{\langle u'^2 \rangle}$, and $\sqrt{\langle v'^2 \rangle}$ between simulation results and observations at $x/H = 10, 15, 17.5, 20, 22.5$, and 25 , and $y/H = 0.125$. The RMSE values for U , $\sqrt{\langle u'^2 \rangle}$, and $\sqrt{\langle v'^2 \rangle}$ were found to be 0.021, 0.006, and 0.006, respectively, and R^2 values for the same flow properties were 0.955, 0.960, and 0.884, showing good agreement between the experimental data and numerical results. In the simulation, the reattachment point in the vicinity of the bed at $y/H = 0.0025$ was found to be $x_r/H = 6.71$, which is reasonably comparable to the experimental data, $x_r/H = 6.25$. Figure 18

compares the mean bedload transport rate Q_x obtained from the simulation and the experiment of Nelson et al. (1995) downstream of the BFS. The dashed line and dash-single dotted line in Figure 17 and Figure 18 represent the reattachment point obtained from the simulation and experiment, respectively. As shown in the figures, the simulated reattachment length and bedload transport rate exhibited reasonable agreement with the observation data. Table 7 compares the quadrant analysis results, while Table 8 shows a comparison of the quadrant analysis results weighted by the instantaneous bedload transport rate q_x , which was named quadrant analysis for bedload transport. Overall, the numerical results were shown to be in line with the experimental data, wherein the dominant turbulence events were found to be burst and sweep; while the sweep and outward events significantly contributed to bedload transport. The good results obtained from the validation process show that the numerical model can be used as a modeling tool to investigate the flow characteristics and their interaction with bedload transport.

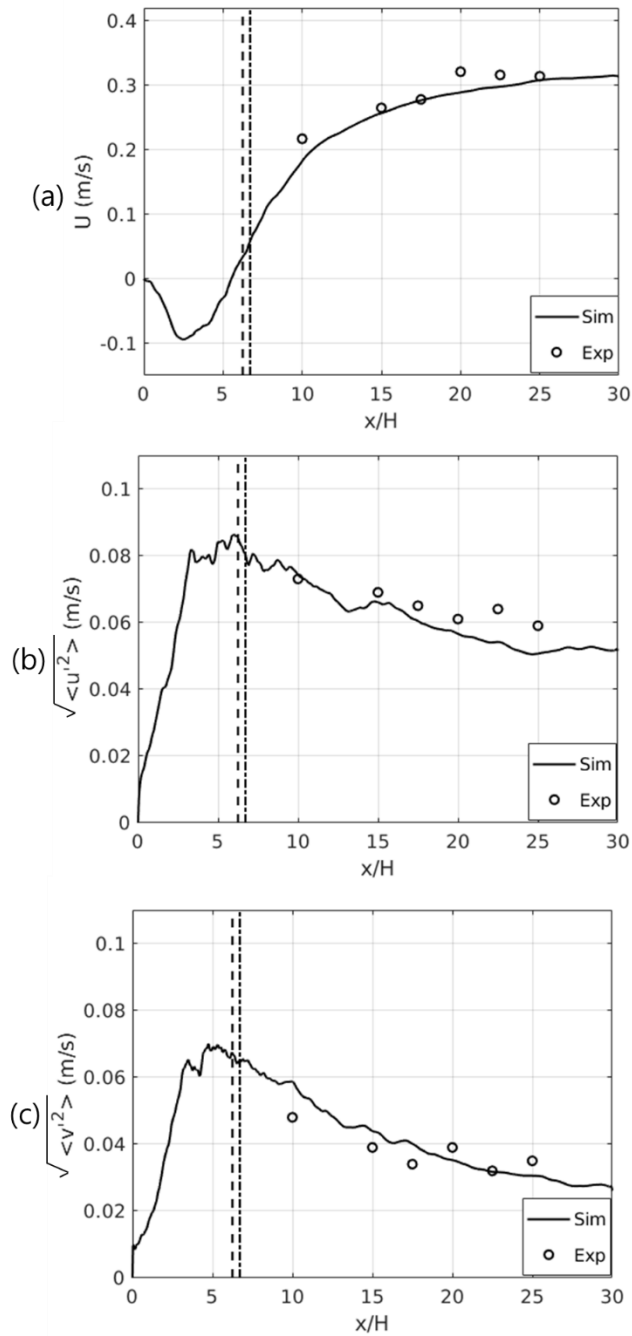


Figure 17. Near-bed streamwise velocity (a), streamwise turbulence intensity (b), and vertical turbulence intensity (c) profiles behind the step (Dotted line=observation data by Nelson et al. (1995); Solid line=simulation data)

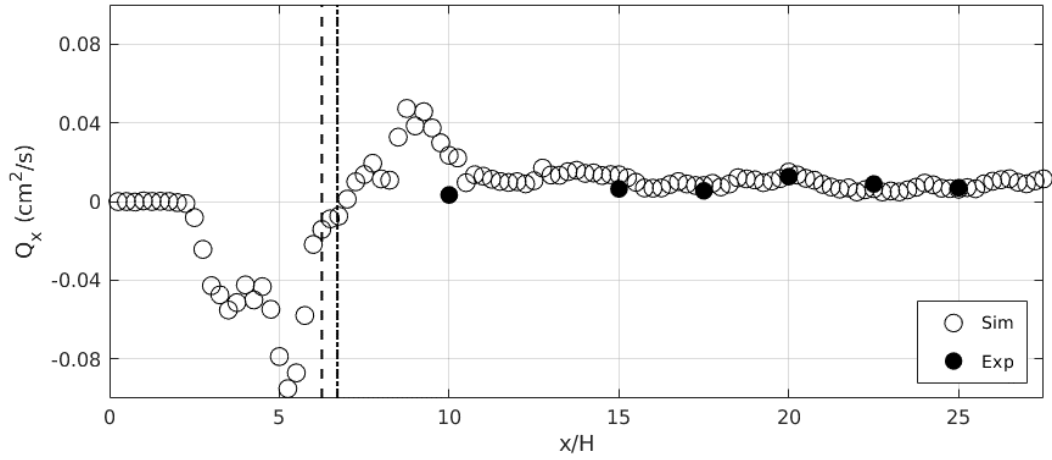


Figure 18. Mean bedload transport rate in the streamwise direction behind the BFS (Circle=simulation data; Circle (filled)=observation by Nelson et al. (1995)).

Table 7. Comparison of percentage of time occupied by each turbulence event between the observation data by Nelson et al. (1995) and simulation results.

x/H	Burst		Sweep		Outward Interaction		Inward Interaction		RMSE
	Exp	Sim	Exp	Sim	Exp	Sim	Exp	Sim	
10.0	33	33.7	33	25.4	13	19.7	21	21.1	5.08
15.0	36	36.6	27	28.0	18	18.1	19	17.3	1.03
17.5	29	29.2	30	28.2	19	22.3	22	20.3	2.07
20.0	30	30.6	31	29.8	20	22.7	18	16.9	1.60
22.5	32	29.5	34	28.5	16	22.3	18	19.6	4.44
25.0	25	31.0	33	28.9	17	20.4	26	19.7	5.10

Table 8. Comparison of percentage of each turbulence event weighted by bedload transport rate between the observation data by Nelson et al. (1995) and simulation results.

x/H	Burst		Sweep		Outward Interaction		Inward Interaction		RMSE
	Exp	Sim	Exp	Sim	Exp	Sim	Exp	Sim	
10.0	15	11.1	48	47.4	32	36.2	4	5.3	2.95
15.0	9	11.7	53	44.5	28	36.5	10	7.3	6.30
17.5	11	13.3	44	41.1	35	37.6	10	8.0	2.47
20.0	14	16.4	48	47.1	30	28.5	9	8.0	1.57
22.5	20	14.5	47	50.0	25	28.3	9	7.2	3.65
25.0	15	16.2	47	39.2	25	28.2	12	16.5	4.82

6.2 Validation against submerged wall jet flow

In this study, the proposed LES-DEM coupling model is further validated to appropriately simulate the scour hole created by the wall jet flow near hydraulic structures. For the validation, the dimensions of the simulated scour hole in the numerical model are compared with the result of the empirical formula derived from the numerous experimental data of Chatterjee et al. (1994).

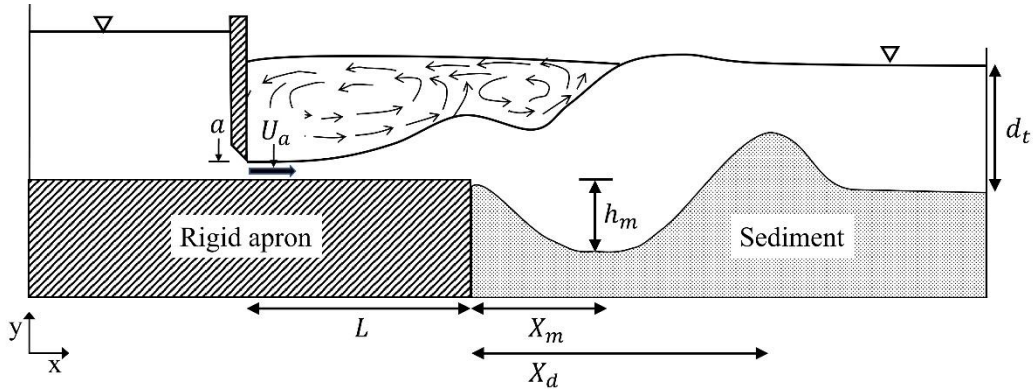


Figure 19. Experimental setup of Chatterjee et al. (1994).

Figure 19 schematizes the experimental setup of Chatterjee et al. (1994). They conducted 28 distinct experiments, varying the gate height (a), discharge velocity (U_a), and mean diameter (d_{50}). The numerical model was validated against one of these experimental conditions, wherein the initial scour can occur relatively quickly. The experimental condition employed for the verification process is listed in Table 9.

Table 9. Experimental configuration from Chatterjee et al. (1994).

L (m)	a (m)	d_t (m)	U_a (m/s)	Fr	d_{50} (mm)	ρ_s (kg/m ³)	Dimensions		
							Length (m)	Width (m)	Depth (m)
0.66	0.02	0.31	2.42	5.46	4.3	2650	9	0.6	0.69

6.2.1 Validation of numerical model against mean velocity

To accurately reproduce the sediment transport process behind the apron, it is crucial to precisely model the wall jet flow at the end of the apron, which is located just upstream of the sediment zone. To confirm the performance of the numerical model employed in this study on properly simulating the flow characteristics of the developed jet flow, the vertical distribution of mean streamwise velocity measured at $x=0$ is compared to that measured by Chatterjee et al. (1980); the results are illustrated in Figure 20. As depicted in the figure, U/U_0 calculated by the numerical model exhibits good agreement with the experimental data, with obtained RMSE and R2 values of 0.0948 and 0.9256, respectively, indicating a reasonable agreement with the observed data. The normalization factor y_z for vertical coordinate y is the inner jet thickness, which is calculated as $y_z = 6$ mm.

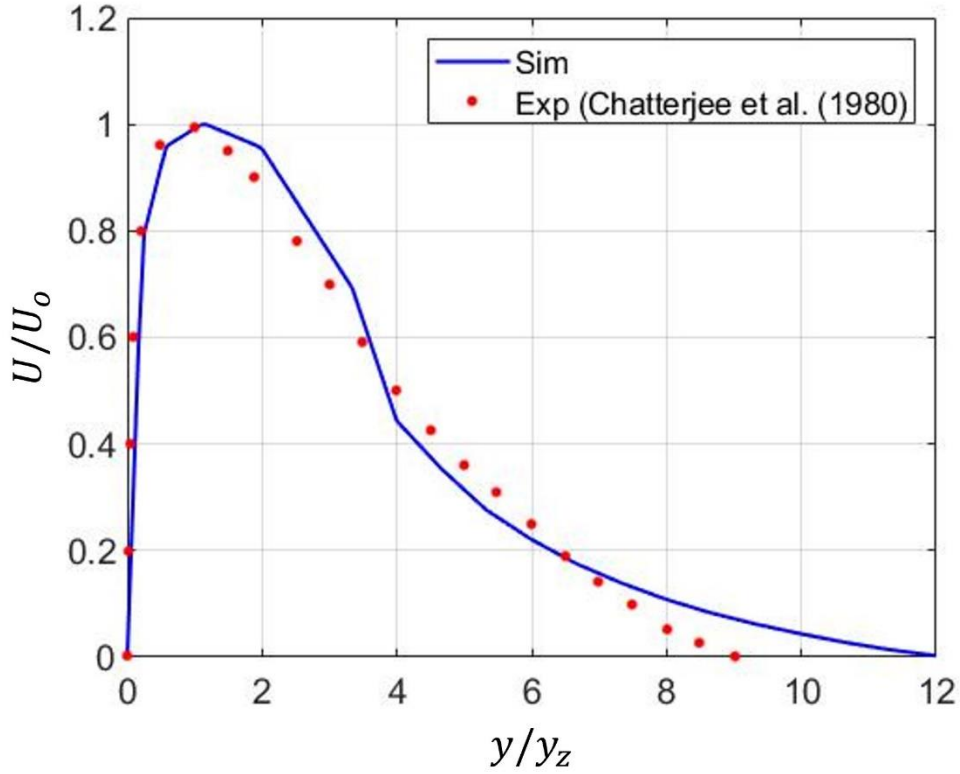


Figure 20. Comparison of vertical distribution of normalized streamwise velocity between simulation and experiment

6.2.2 Validation of numerical model against scouring dimensions

Figure 21 shows the variation of maximum scour depth (h_m), location of maximum scour (X_m), and the peak position of dune (X_d) derived from the numerous data sets obtained from the experiments conducted by Chatterjee et al. (1994). We can find the relationships of the scour dimensions in the figure as a function of scour volume (V_s) as follows:

$$X_m = 0.6V_s^{0.374} \quad (36)$$

$$X_d = 2.684V_s^{0.45} \quad (37)$$

$$h_m = 0.513V_s^{0.549} \quad (38)$$

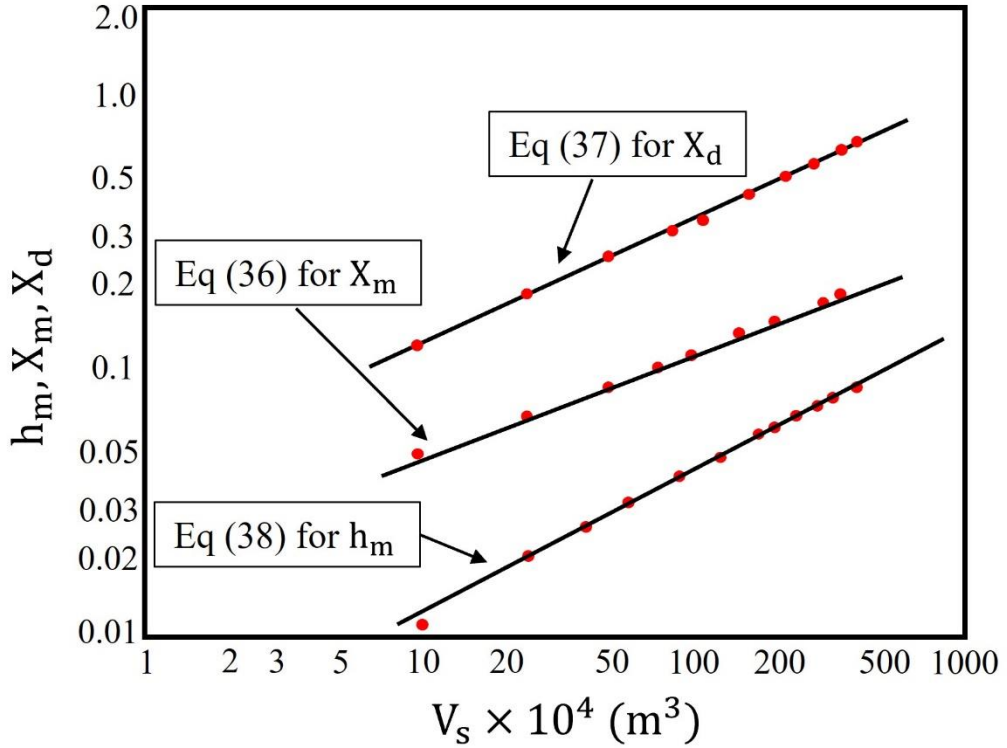


Figure 21. Relationships of dimensions of scour hole and scour volume from Chatterjee et al. (1994). Red dots represent the experimental sets.

They also suggest a formula to estimate the scour volume (V_s) from the data sets as follows:

$$V_s = 0.374U_a^2a\left(\frac{t}{T}\right)^{0.343} \quad (39)$$

Where t and T are the time elapsed from when the sluice gate is opened and the time for equilibrium, respectively. the numerical model is validated against the scour dimensions after 60 s.

The comparison between the scour hole's dimensions from the simulation and the formulas from Chatterjee et al. (1994) is presented in Figure 22 and Table 10. In Figure 22, X_{me} and X_{ms} represent the location of maximum scour obtained by the simulation and empirical formula; X_{de} and X_{ds} denote the location of the peak of the dune calculated by the simulation and empirical formula; h_{me} and h_{ms} are the maximum scour depth quantified by the simulation and empirical formula, respectively.

Table 10. Comparison of the scour hole's dimensions between the simulation and empirical formula from Chatterjee et al. (1994).

	X_m (m)	X_d (m)	h_m (m)
Chatterjee et al. (1994)	0.132	0.385	0.05
LES-DEM	0.151	0.371	0.054
Error (%)	-14.4	3.63	8

The error rate between the simulated and estimated values of X_m and X_d were found to be -14.4 % and 3.63 % based on the experimental data. The error of maximum scour depth h_m was 8 %. Overall, a good agreement between the simulation results and experimental data has been achieved.

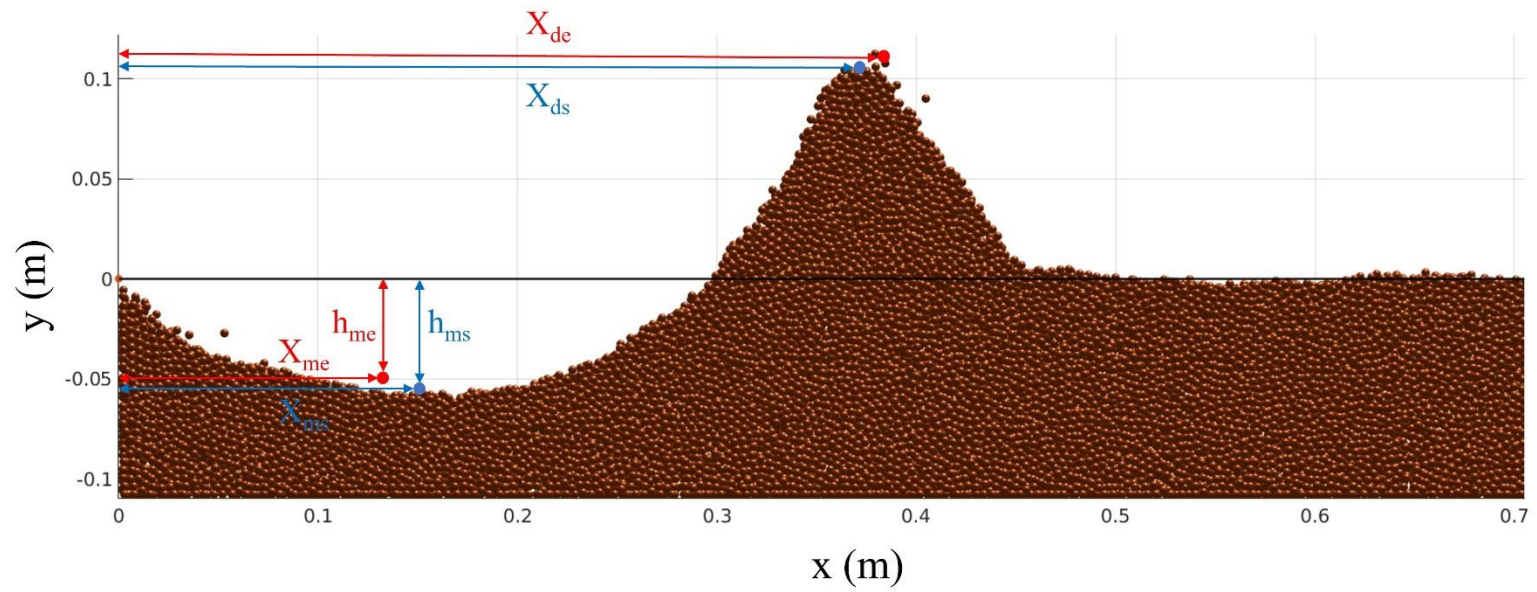


Figure 22. Scour hole's dimensions formed by simulation and estimated by Chatterjee et al. (1994).

CHAPTER 7. RESULTS

7.1 Surface jet flow behind various inclined BFSs

The results shown in this chapter provide the near-bed flow and sediment properties measured for 60 s after the flow is fully developed. It should mention that the simulation time of 60 s is sufficient to examine the interaction between flow structures and sediment behaviors, as suggested by Nelson et al. (1995) and Schmeeckle (2015). The near-bed flow structures and their interaction with bedload transport associated with various angles of the inclined BFSs are presented and discussed in detail in the following chapters.

7.1.1 Near-bed flow structure

Figure 23 illustrates the near-bed mean velocity and turbulence intensity measured at the vicinity of channel bed ($y/H = 0.0025$) from the step to downstream of various inclined BFSs (10° , 20° , 30° , and 90°). The solid black line in the snapshots represents the reattachment point at $x = x_r$. It was found that the flow separation was first formed at the step angle of 20° (CaseN20). It also shows that the increment in the reattachment length x_r as the step angle α increases from 20° to 30° is significantly longer than those when α increases from 30° to 90° . This tendency is consistent with the findings of Ruck and Makiola (1993) for Reynolds numbers higher than 15,000. In addition, the reattachment length obtained from CaseN90 (step angle of 90°) was found to be about 6.71, which falls within the range between 3 and 9 suggested by Nezu and Nakagawa

(1987, 1989). The snapshots in Figure 26 show the mean velocity vector at the central vertical plane for the various BFS angles. Figure 26a shows that flow separation is not induced in CaseN10 ($\alpha = 10^\circ$); the separation zone started to form up, and enlarged as the step angle α is increased to 20° , 30° , and 90° , consequently the reattachment length is extended further downstream, as indicated in Figures 26b-26d. Figure 27 depicts the mean velocity profiles at the centerline longitudinal plane at 11 different measurement points. It is confirmed that the mean flow is almost recovered far downstream (at $x/H=25$) in all the simulation cases. The information on the reattachment length (x_r/H) and mean velocity (U/U_0) near the bed is shown in Table 11.

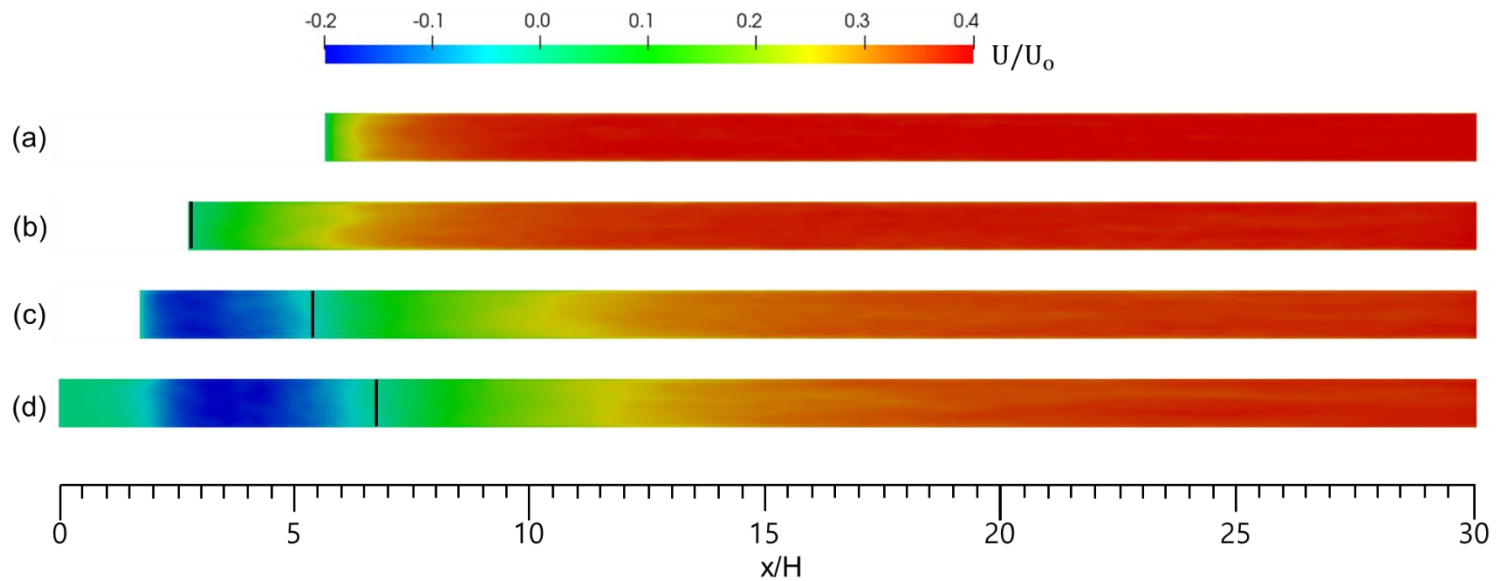


Figure 23. Mean streamwise velocity for CaseN10 (a), CaseN20 (b), CaseN30 (c), and CaseN90 (d). Solid line represents the reattachment point.

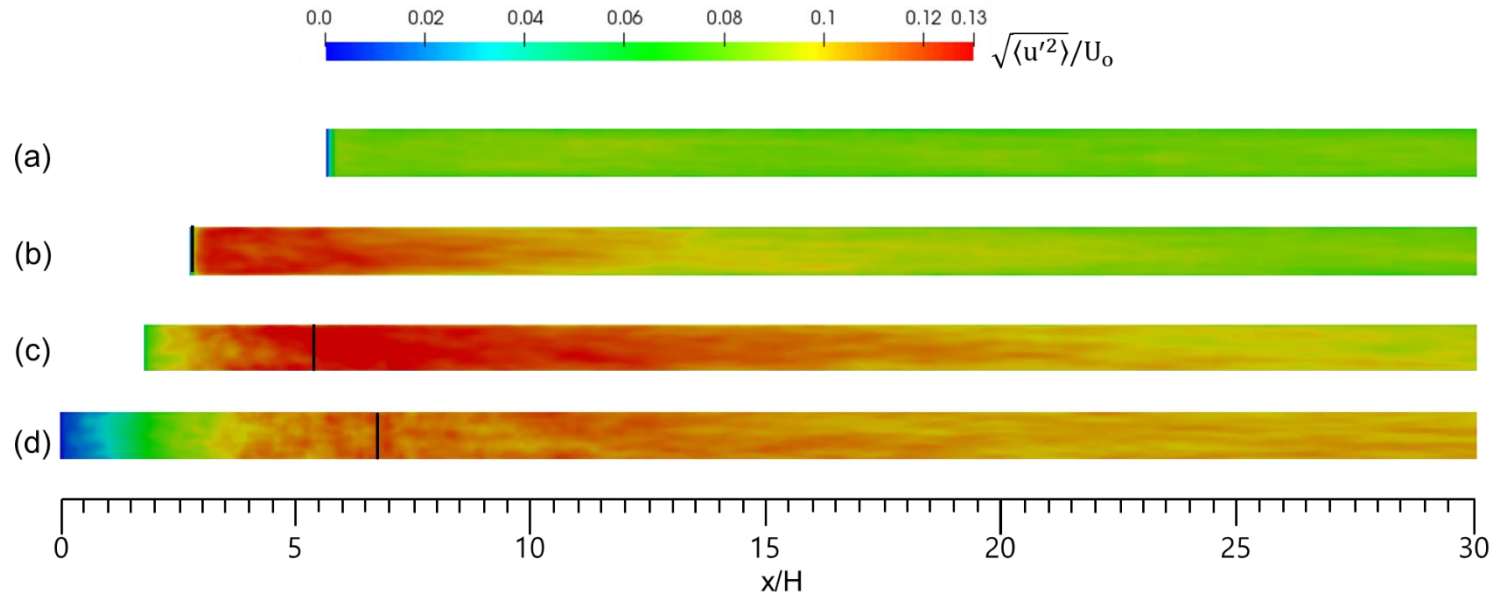


Figure 24. Streamwise turbulence intensity for CaseN10 (a), CaseN20 (b), CaseN30 (c), and CaseN90 (d). Solid line represents the reattachment point.

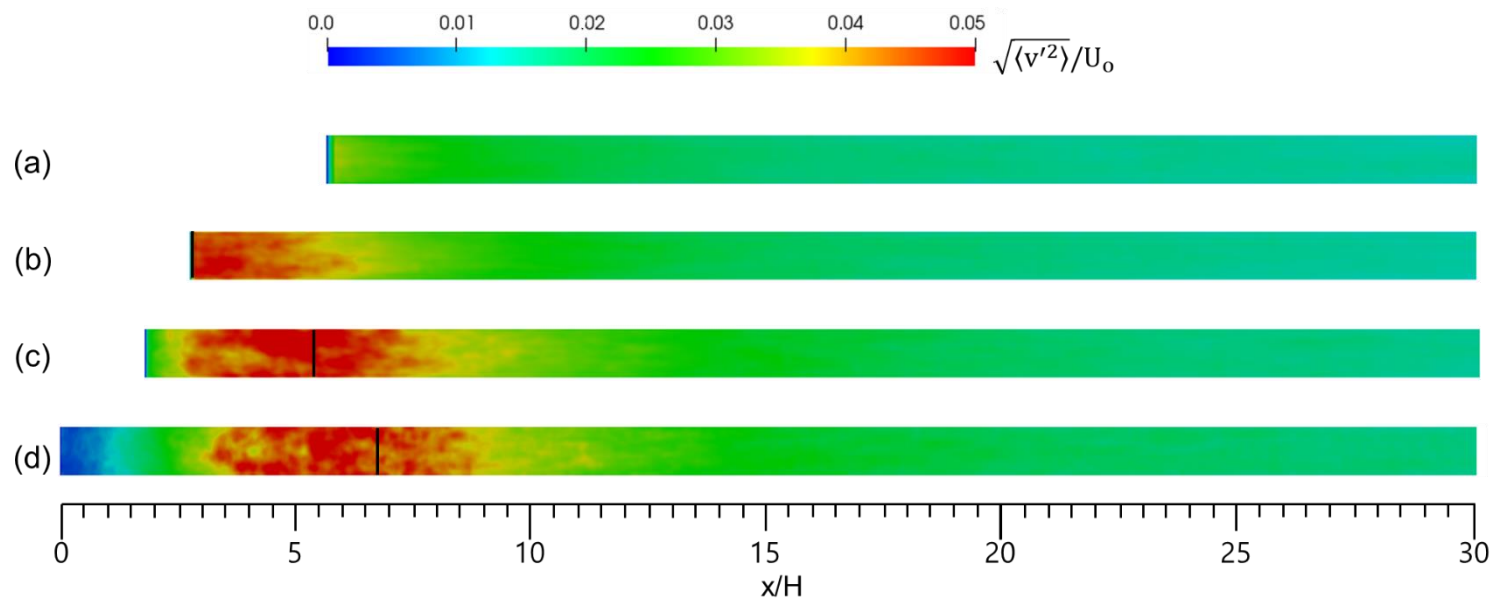


Figure 25. Vertical turbulence intensity for CaseN10 (a), CaseN20 (b), CaseN30 (c), and CaseN90 (d). Solid line represents the reattachment point.

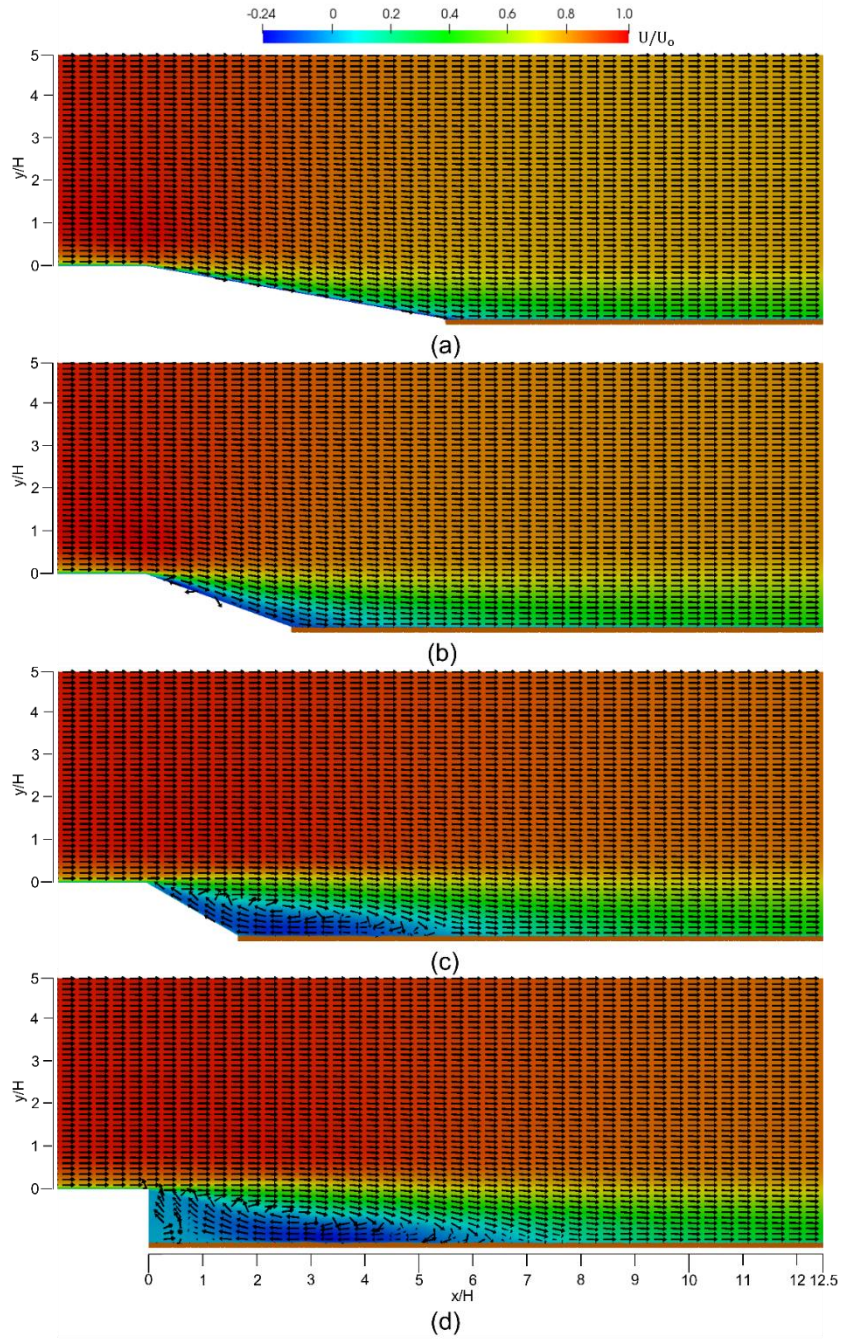


Figure 26. Separation zone with time-averaged velocity vectors in the central section of the z-axis for CaseN10 (a), CaseN20 (b), CaseN30 (c), and CaseN90 (d).

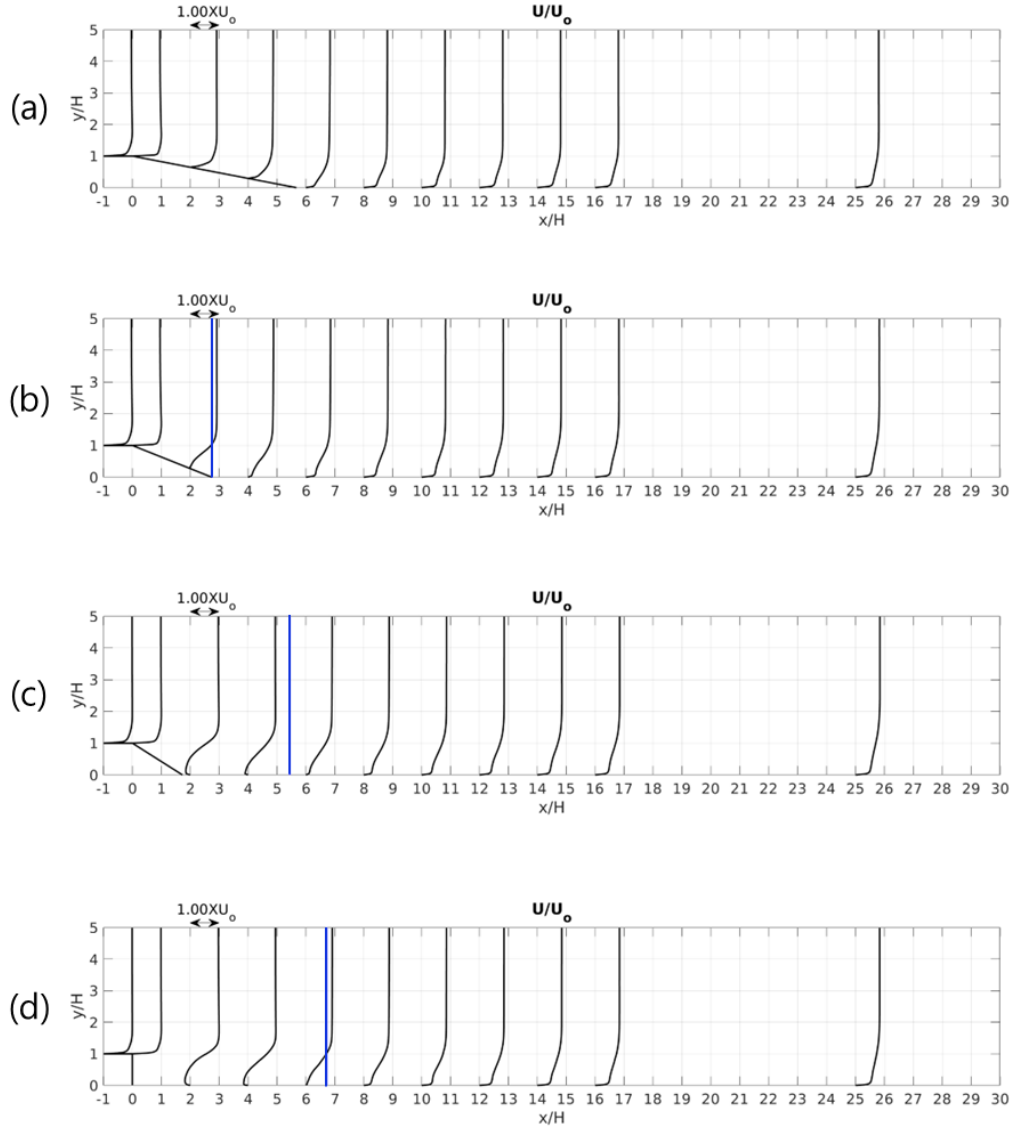


Figure 27. Streamwise velocity profiles behind the step measured in the central vertical plane for CaseN10 (a), CaseN20 (b), CaseN30 (c), and CaseN90 (d). Blue line represents the reattachment point.

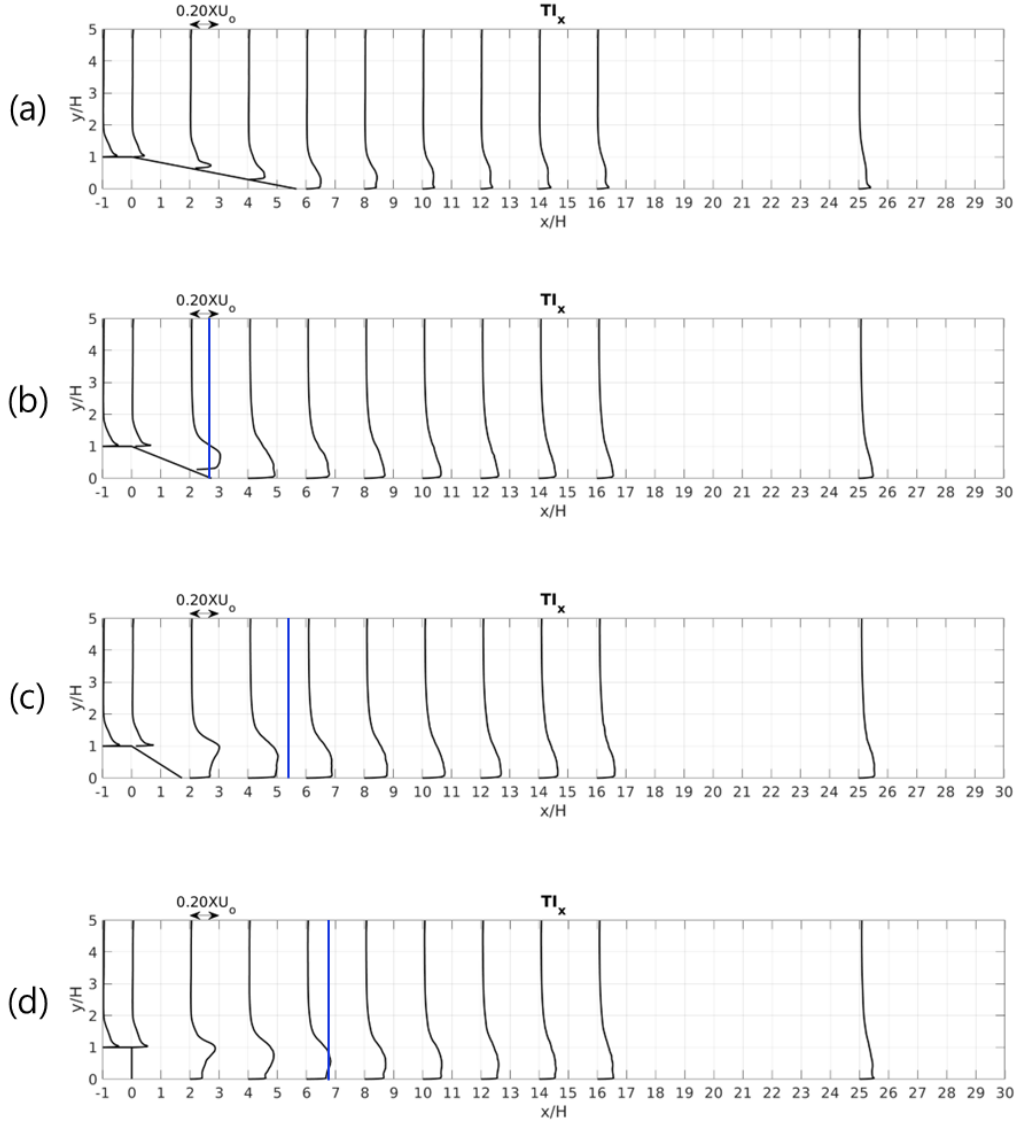


Figure 28. Streamwise turbulence intensity profiles behind the step measured in the central vertical plane for CaseN10 (a), CaseN20 (b), CaseN30 (c), and CaseN90 (d). Blue line represents the reattachment point.

Figures 24 and 25 present the near-bed turbulence intensity in the streamwise and vertical directions. It showed that the turbulence intensities $TI_x \left(\sqrt{\langle u'^2 \rangle} / U_o \right)$ and $TI_y \left(\sqrt{\langle v'^2 \rangle} / U_o \right)$ drastically increased once the flow separation occurred in CaseN20 ($\alpha = 20^\circ$). It shows that the maximum value of TI_x and TI_y at this step angle was significantly increased respectively at 50% and 61.3% in comparison to those in CaseN10 ($\alpha = 10^\circ$). As the BFS angle further increased to $\alpha = 30^\circ$ and 90° , the change of the maximum values of TI_x and TI_y became negligible. This tendency is also shown in Figures 28 and 29 near the channel bed. The second-order flow statistics are summarized in the third and fourth columns of Table 11. It shows a significant increase in TI_y when flow separation starts to occur (at $\alpha = 20^\circ$) due to the splat effect, which was first conceptualized by Perot and Moin (1995). This splat effect occurs as the eddies along the SSL splash on the bed around the reattachment point. After impinging on the bed, the flow moves parallel to the bed, leading to massive turbulent diffusion. The splat effect has also been numerically identified in the simulations by Stoessor et al. (2008) and Schmeeckle (2015) in the vicinity of the bed for a separation flow. In addition, the numerical results show that the maximum value of turbulence intensity is the largest once $\alpha = 20^\circ$ and 30° located around the reattachment point, as shown in Table 11, which is consistent with the findings in the wind tunnel experiments of Ruck and Makiola (1993).

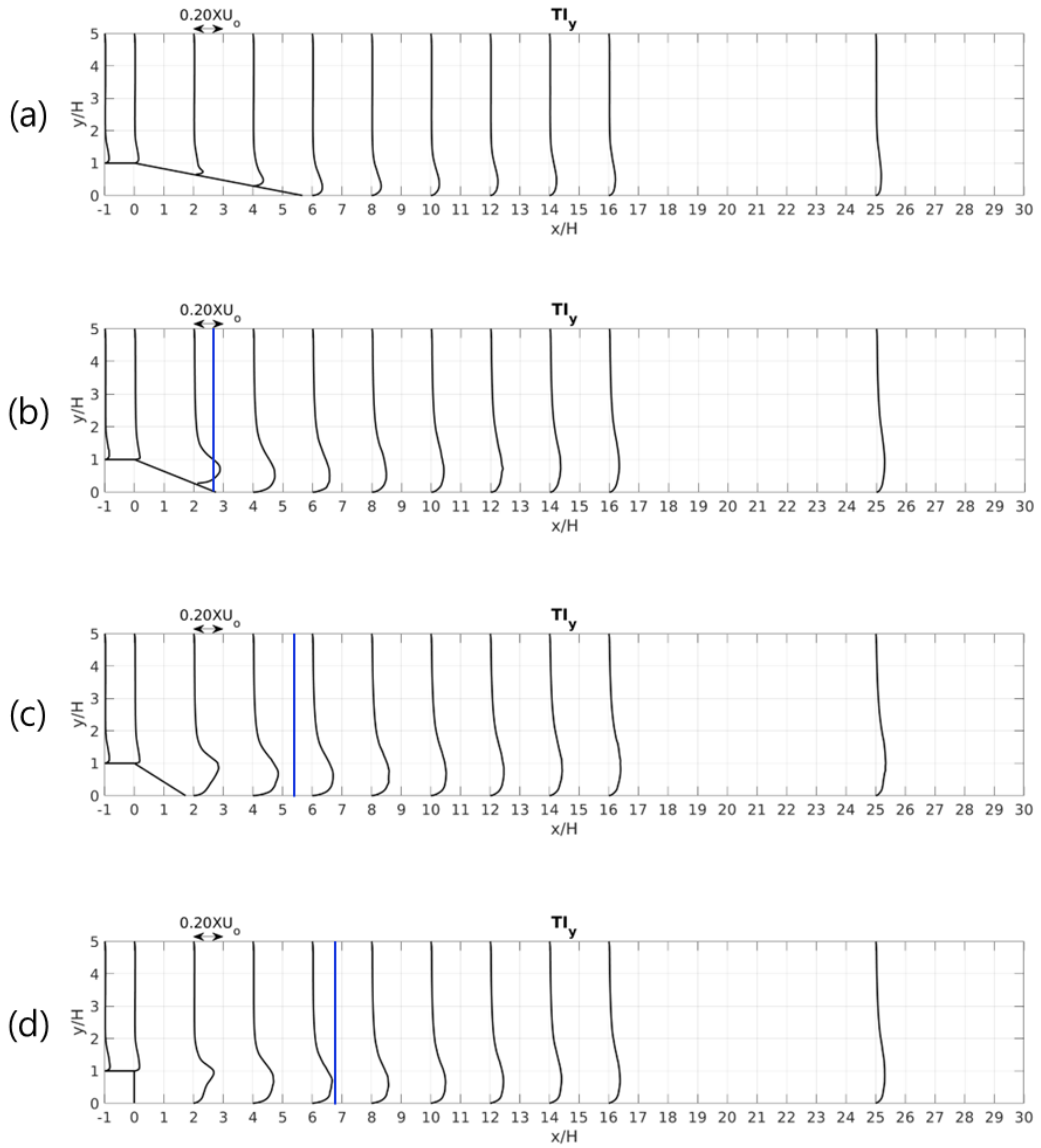


Figure 29. Vertical turbulence intensity profiles behind the step measured in the central vertical plane for CaseN10 (a), CaseN20 (b), CaseN30 (c), and CaseN90 (d). Blue line represents the reattachment point.

Figure 30 illustrates the instantaneous coherent turbulent structures at arbitrary times using Q-criterion. The isosurface value of Q in the figure was determined as 600 because the hairpin- coherent vortices at this value were best presented for the simulation results. The contour of Q in the figures is colored based on the vorticity ω_z normalized by H and U_o . As depicted in the figure, only small-scale vortex structures along the BFS are generated in CaseN10 due to the lack of flow separation. However, when the flow is separated in CaseN20, the coherent vortices begin to form rapidly in the form of hairpin vortices, and as α further increases, the vortices are generated more actively. In the same context, ω_z is also increased as the flow separation occurs in CaseN20. However, ω_z barely increases for further increasing α ($\alpha > 30^\circ$). The coherent vortices were enlarged to downstream as the angle α is increased. This is consistent with the increased turbulence intensity near the bed, as shown in Figures 24 and 25. The energetic coherent vortices when flow separation occurred ($\alpha = 20^\circ, 30^\circ$, and 90°), depicted in Figure 30b-30d, are responsible for the large peaks of sediment transport rates shown in Figure 31.

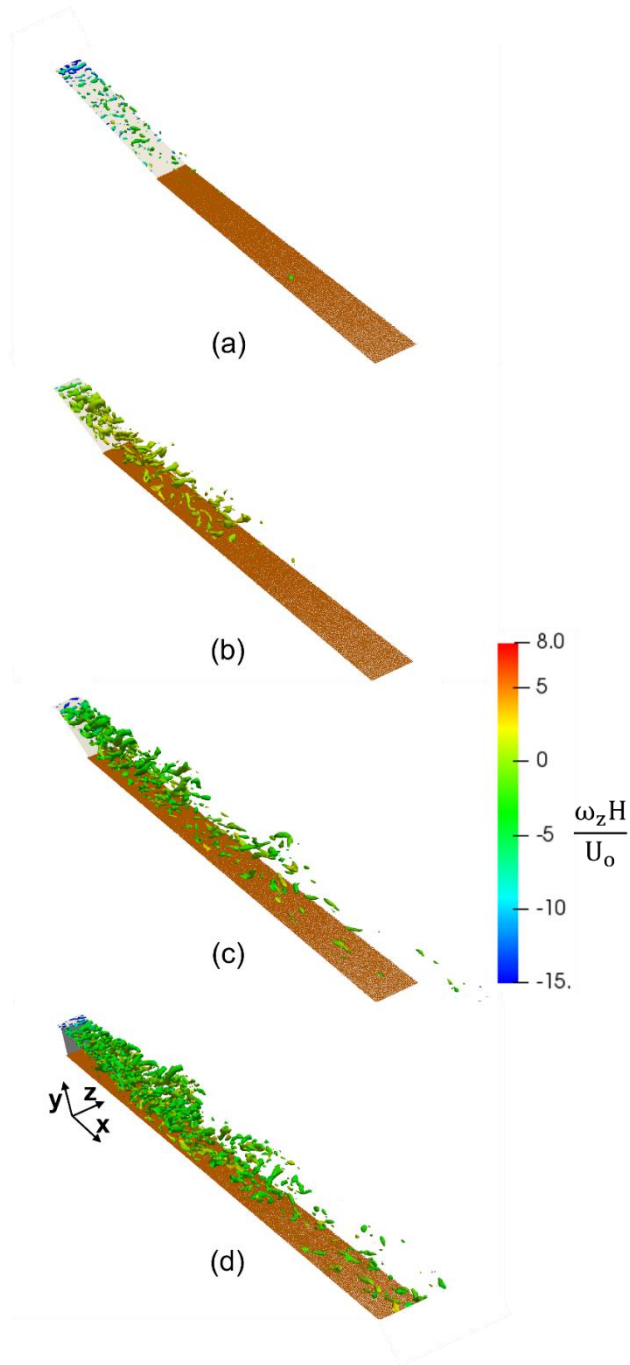


Figure 30. Coherent vortex structures visualized by Q-criterion (isosurface: $Q=600$) for CaseN10 (a), CaseN20 (b), CaseN30 (c), and CaseN90 (d) at different instants.

7.1.2 Sediment flux

Q_x was measured at much shorter streamwise distance intervals (0.01 m) than in Nelson et al. (1995), in which only six measurement points were used. The spanwise measurement length was determined as 0.03 m. The numerous measurement gauges in the simulations enabled us to explore better the trend of bedload transport rate along the flow direction, as shown in Figure 31.

Table 11. Near-bed flow information and bedload transport rate.

	x_r/H	Max (U/U_o)	Max (TI_x)	Max (TI_y)	Q_x (cm ² /s) [Min, Max]
CaseN10	-	0.4	0.08	0.031	[0.0005, 0.0136]
CaseN20	2.75	0.39	0.12	0.05	[-0.001, 0.072]
CaseN30	5.44	0.37	0.13	0.057	[-0.092, 0.045]
CaseN90	6.71	0.37	0.11	0.052	[-0.095, 0.047]

Figure 31 plots Q_x along the streamwise direction for all the simulation cases. The streamwise coordinate x was substituted with a normalized coordinate x' , defined as $x' = x - x_b$. This is to locate the origin of the streamwise coordinate at $x = x_b$ for each case. The minimum and maximum values of Q_x are summarized in the last column of Table 11. The low amplitude of Q_x in CaseN10 indicates that the high mean velocity does not play a substantial role in sediment movement if flow separation is not formed, as mentioned by previous studies (Nelson et al., 1993 and McLean et al., 1994).

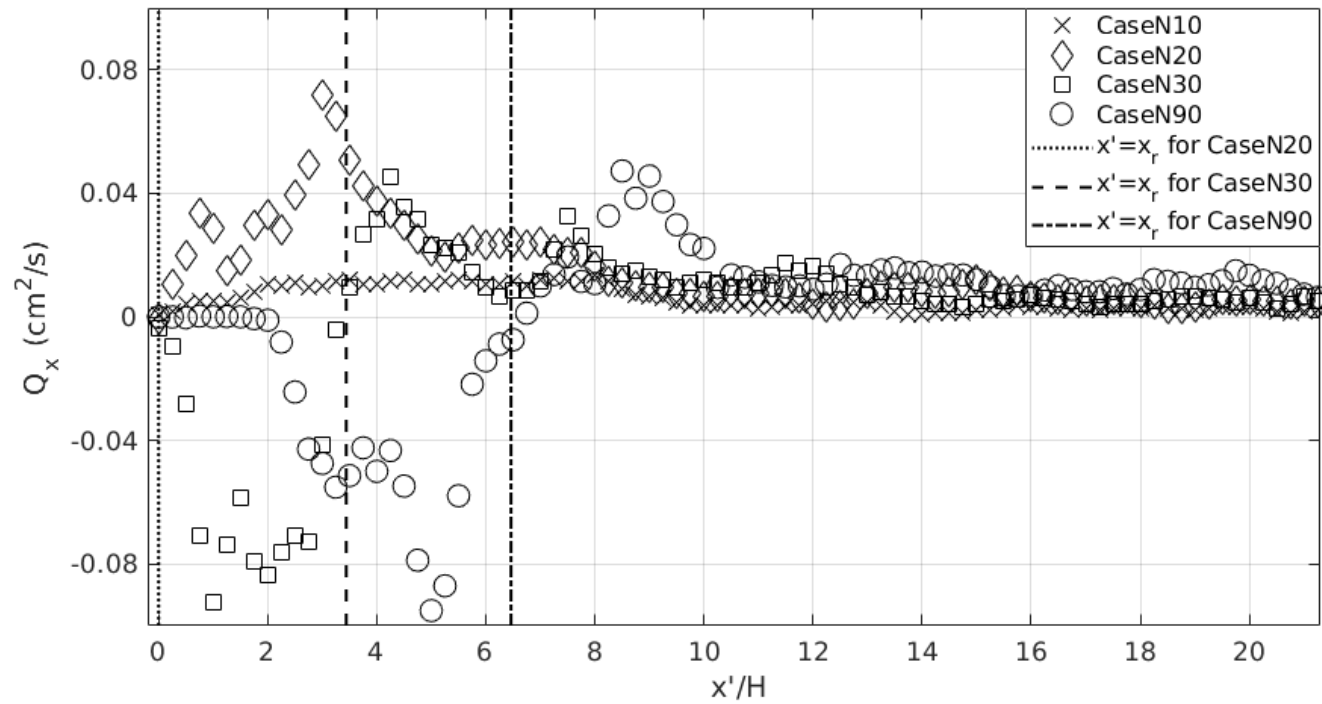


Figure 31. Mean bedload transport rate downstream of the various inclined BFSs (the dash lines show the locations of reattachment points associated with step angles).

However, in the cases of flow separation, such as CaseN20, CaseN30, and CaseN90, the amplitude of Q_x was much larger than that in CaseN10. It indicates that the position at which the direction of Q_x shifts from backward to forward almost coincides with the location of reattachment point at $x = x_r$. However, the backward sediment transport in CaseN20 is barely observed due to the very short reattachment length downstream of the BFS. Among all the simulation cases, the maximum peak of Q_x was observed in CaseN20 when the flow separation started to form. This can be attributed to the rapidly increased turbulence intensity and fast flow recovery right downstream of the reattachment, as shown in Figures 23-25. It appeared that the peak value of Q_x is decreased in CaseN30 and CaseN90 in comparison to that in CaseN20. In those cases, another peak of Q_x in the opposite direction of the flow was observed at some distances upstream of the reattachment point. This can be explained by an increase in backflow velocity near the bed upstream of the reattachment point, as illustrated in Figures 23c and 23d.

As shown in Figure 31, the peak of the bedload flux Q_x obtained from CaseN90 is located further downstream in comparison with the results obtained from CaseN30 as the reattachment length is extended. This finding demonstrates that the BFS angle plays a substantial role in sediment behaviors. In addition, it was found that as the BFS angle increases, the distance needed to stabilize the bedload movement also increases. Indeed, the bedload transport rates measured at $x'/H = 20$, which is sufficiently far from the step, were $0.003\text{cm}^2/\text{s}$, $0.0056\text{cm}^2/\text{s}$, $0.0059\text{cm}^2/\text{s}$, and $0.0135\text{cm}^2/\text{s}$ for CaseN10, CaseN20, CaseN30, and CaseN90, respectively. In CaseN20, there was no significant difference in the distance needed for the sediment movement to be stabilized compared to

CaseN30, although the vortex structures in CaseN20 were less actively generated than in CaseN30.

7.1.3 Quadrant analysis for flow structure

The quadrant analysis approach, described in Chapter 4.8, was applied to investigate the turbulent flow structures near the bed, and the results are summarized in Table 12, including the measurement points. As shown in the table, most measurement points are located near the reattachment points. Because there was no flow reattachment numerically found in CaseN10, we substituted the base measurement point $x = x_r$ with $x = x_b$ for this simulation case exceptionally. The results upstream of the reattachment point at $x = x_r - 2.5H$ for CaseN10 and CaseN20 are not presented since the measurement points are not included in the computational domain.

Figures 32 and 33 illustrate the frequency contours of the fluctuating velocity pairs in the four quadrants. The frequencies were normalized to a peak value of unity in the figures. The legend in those figures represents the frequency probability with intervals of 0.1. The quadrant analysis results reveal that the bursts and sweeps are the most prevalent turbulence events, regardless of the BFS angle, as illustrated in Figures 32 and 33. This result indicates that the dominant turbulence events are not dependent on the BFS angle or location behind the BFS. However, we can see that the area of the frequency distribution becomes larger for the cases when flow separation occurs, such as CaseN20, CaseN30, and CaseN90. This is consistent with the higher turbulence intensity shown in Figures 24 and 25 for those cases.

Table 12. Ratio of time (in percentage) by each turbulence event in various BFS angles.

Measurement Point	α (°)	Burst	Sweep	Outward interaction	Inward interaction
$x = x_r - 2.5H$	10	-	-	-	-
	20	-	-	-	-
	30	31.4	26.1	20.4	22.2
	90	28.8	29.4	19.3	22.5
$x = x_r$ $x = x_b$ (CaseN10)	10	37.7	33.2	13.9	15.2
	20	21.6	35.2	24.5	18.7
	30	35.1	26.7	17.2	20.9
	90	30.2	30.3	15.2	24.4
$x = x_r + 2.5H$ $x = x_b + 2.5H$ (CaseN10)	10	36.1	28.5	18.6	16.8
	20	33.1	25.7	21.7	19.5
	30	26.6	29.8	22.3	21.3
	90	34.8	25.8	17.8	21.6
$x = x_r + 5H$ $x = x_b + 5H$ (CaseN10)	10	32.5	30.0	19.0	18.5
	20	36.4	25.4	21.8	16.5
	30	27.1	28.6	22.7	21.6
	90	33.6	27.6	21.4	17.4
$x = x_r + 10H$ $x = x_b + 10H$ (CaseN10)	10	32.3	32.2	18.3	17.3
	20	30.7	28.2	22.1	19.0
	30	26.2	29.3	24.2	20.3
	90	29.2	28.2	22.3	20.3
$x = 25H$	10	29.0	34.1	19.9	17.0
	20	33.2	30.1	19.3	17.5
	30	28.6	27.6	23.8	20.1
	90	31.0	28.9	20.4	19.7

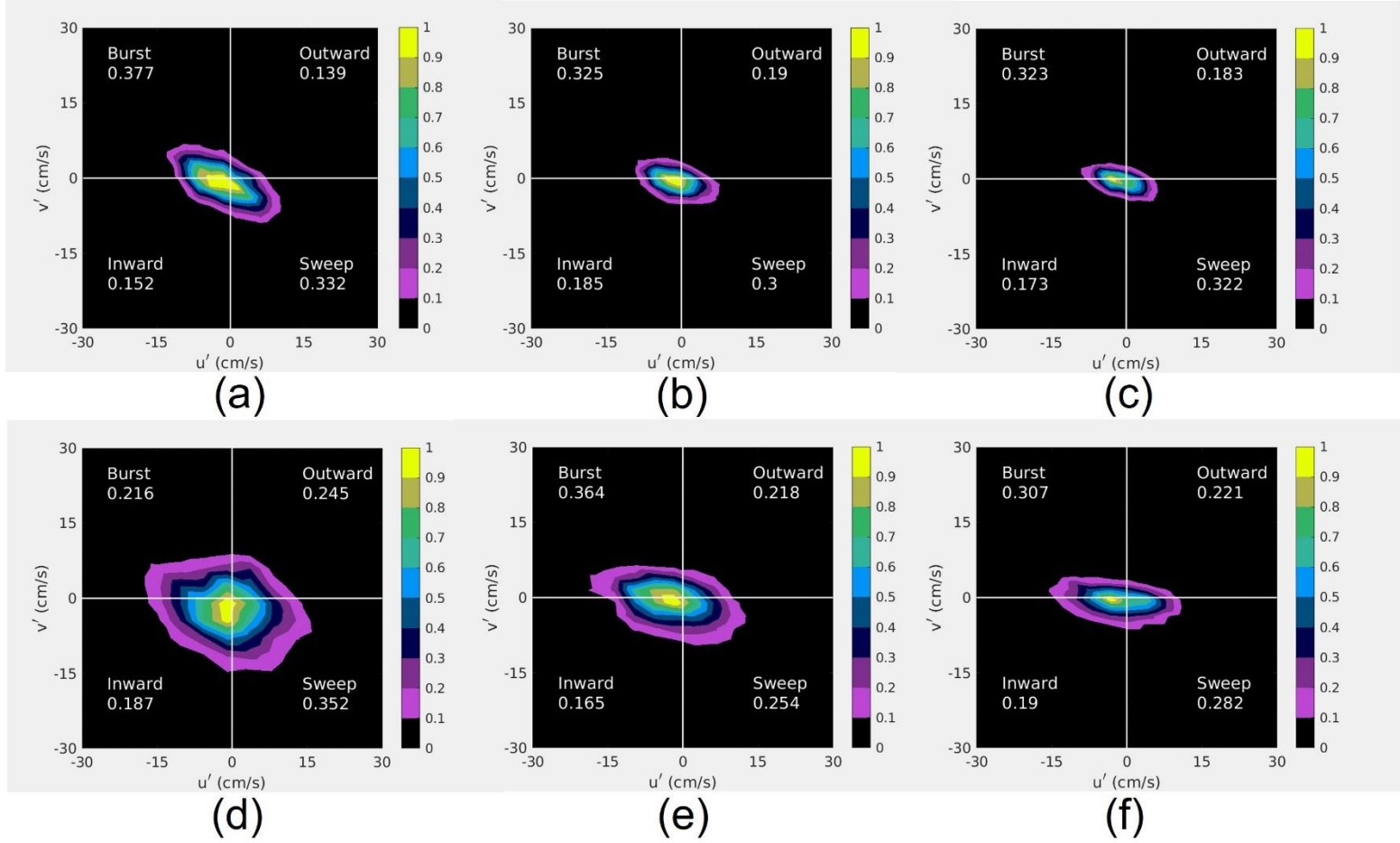


Figure 32. Joint frequency distributions of u' and v' measured at $x = x_b$ (a), $x_b + 5H$ (b), and $x_b + 10H$ (c) for CaseN10, and $x = x_r$ (d), $x_r + 5H$ (e), $x_r + 10H$ (f) for CaseN20.

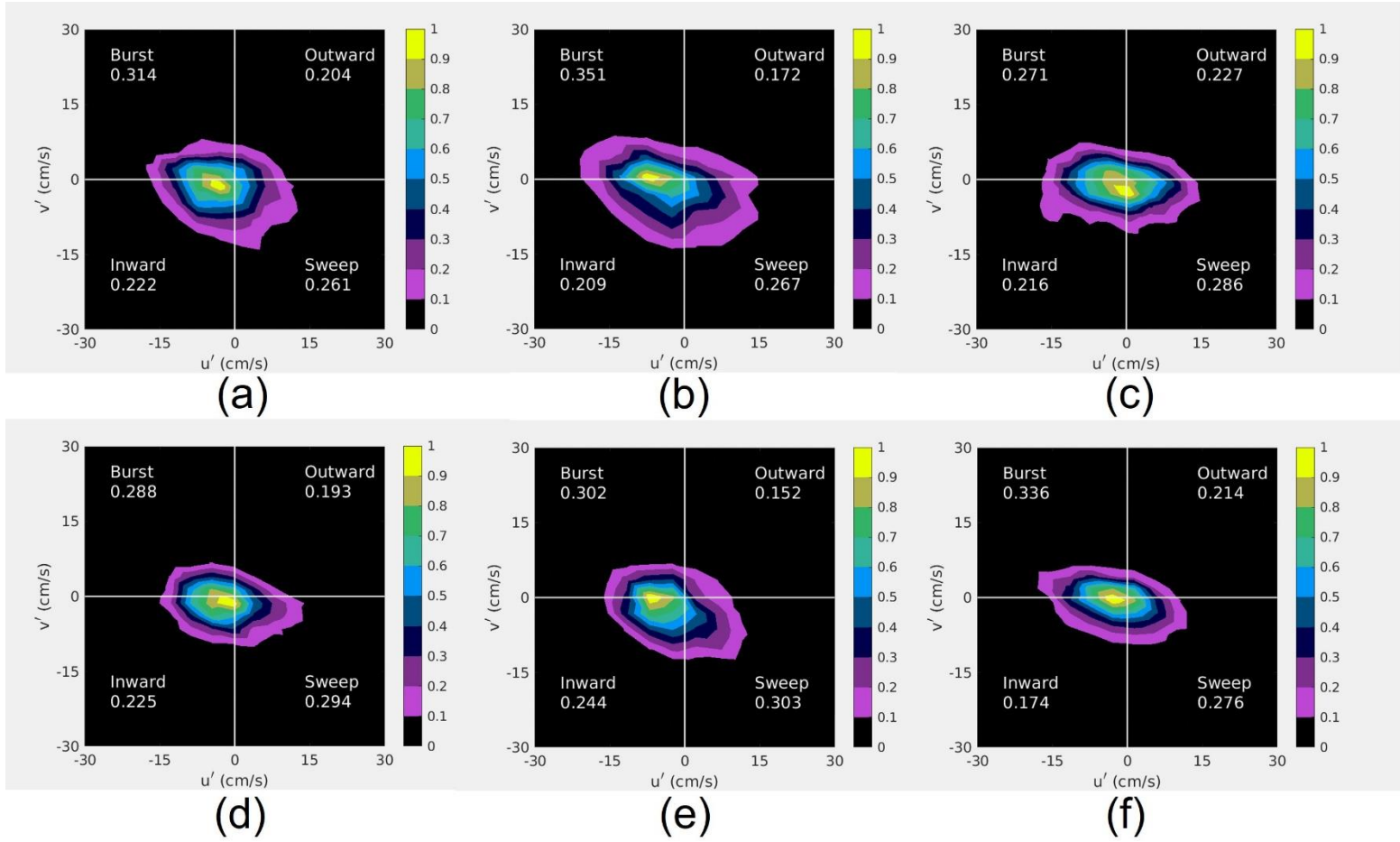


Figure 33. Joint frequency distributions of u' and v' measured at $x = x_r - 2.5H$ (a, d), x_r (b, e), and $x_r + 5H$ (c, f) for CaseN30 (a-c) and CaseN90 (d-f).

7.1.4 Quadrant analysis for bedload transport

The weighted-quadrant analysis technique, delineated in Chapter 4.9, was utilized to examine the interaction between the turbulent flow structures and sediment movement. The results of the weighted-quadrant analysis are summarized in Table 13. The measurement points used are the same as those in the quadrant analysis for flow structure. The q_x -weighted joint frequency contours in percentage were plotted in Figures 34 and 35. The results are illustrated in the figures at three representative measurement points where the difference of the dominant turbulence events is best seen near the reattachment point. The frequencies shown in Figures 34 and 35 together with Table 13 clearly demonstrate the dependence of the interaction between near-bed turbulence structures and sediment motions on the BFS angle.

In CaseN10, the flow separation did not occur, it shows that the two most dominant turbulence events were bursts and sweeps, which however have less effect on sediment movement. Overall, the bedload transport rate was relatively small in this case. These results agree with the observation data obtained from Nelson et al. (1995) when the flow is not separated. However, in all other simulation cases (CaseN20, CaseN30, and CaseN90) when flow separation occurs, it shows that the bedload transport rate significantly becomes larger, especially around the reattachment point. It appeared that burst was the most dominant turbulence event to drag most sediment backward at $x = x_r - 2.5H$ located just upstream of the reattachment point, as depicted in Figures 35a and 35d. This dominant ratio of bedload transport in the backward direction is in line with the negative bedload transport rate for CaseN30 and CaseN90 shown in Figure 31. At $x = x_r$,

the sweep was the most dominant turbulence events to drag the sediment forward, as shown in Figure 34d, Figure 35b, and Figure 35e. This trend lasted until $x = x_r + 2.5H$ in CaseN20 and CaseN30, and $x = x_r + 5H$ in CaseN90, in which the larger coherent vortices are generated as shown in Figure 30. These prevailing sweep events clearly represent the splat effect at the reattachment point and are the most responsible for sweeping the sediment forward. The dominant burst and sweep events on the basis of the reattachment point are in concurrence with the high vertical turbulence intensity presented in Figures 25b-25d. Schmeeckle (2015) also identified that the sediment movements at the reattachment point were mainly attributed to the sweep event with strong instantaneous bed shear stress therein. At $x = 25H$, the two most dominant turbulence events are burst and sweep in CaseN20, and sweep and outward interactions in CaseN30 and CaseN90, which are showing that the flow separation effect in the larger BFS angles is still contributing to dragging the sediment further downstream. In this regard, we can identify the relatively higher value of Q_x on downstream shown in Figure 31. It was also confirmed by Nelson et al. (1995) that the dominant turbulence events to move the sediment downstream were the sweep and outward interactions for a perpendicular BFS at the same measurement point (at $x=25H$). This result suggests that the dominant turbulence event to move the sediment is significantly dependent on the BFS angle and the reattachment length.

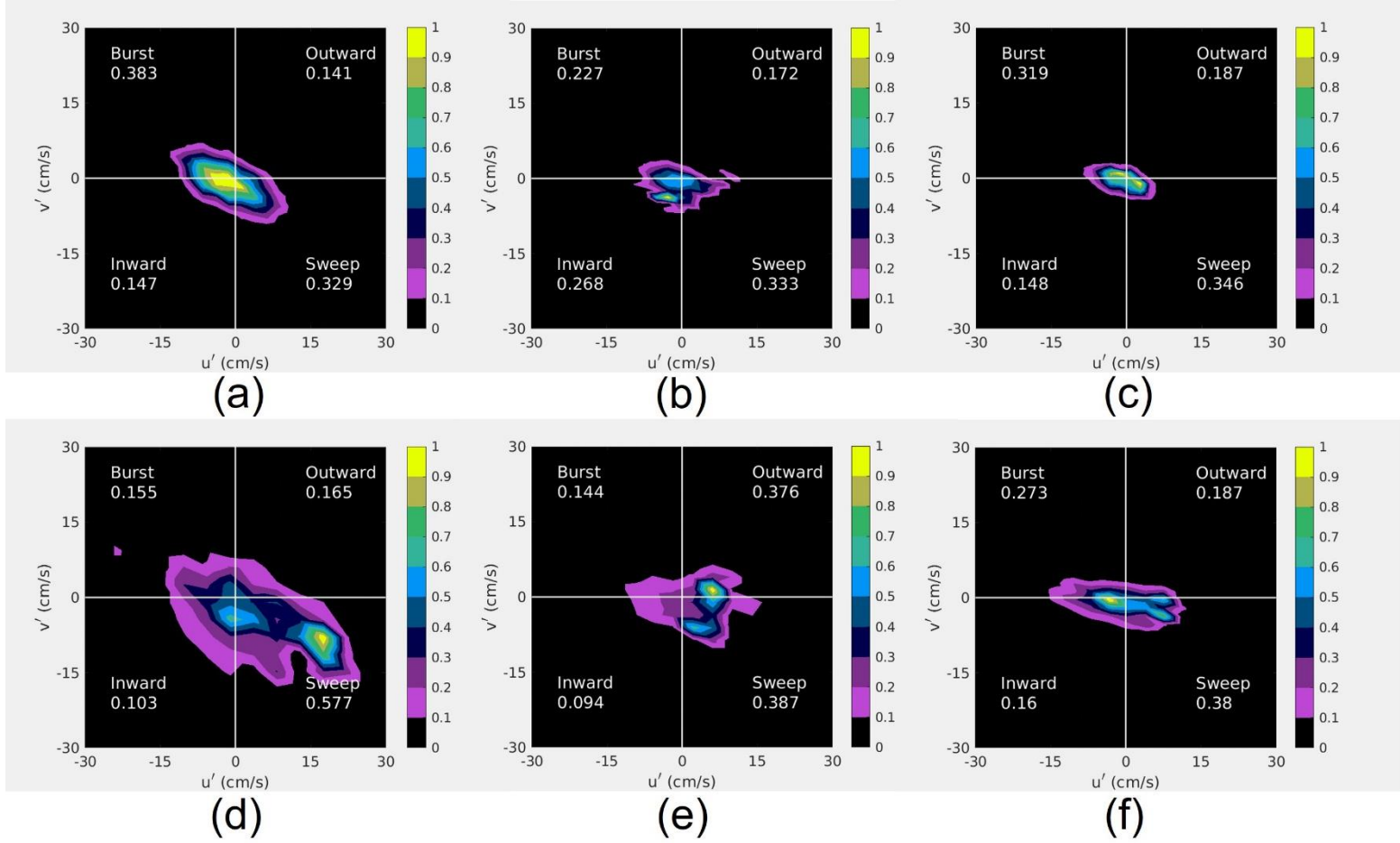


Figure 34. Joint frequency distributions of u' and v' weighted by q_x measured at $x = x_b$ (a), $x_b + 5H$ (b), $x_b + 10H$ (c) for CaseN10, and $x = x_r$ (d), $x_r + 5H$ (e), $x_r + 10H$ (f) for CaseN20.

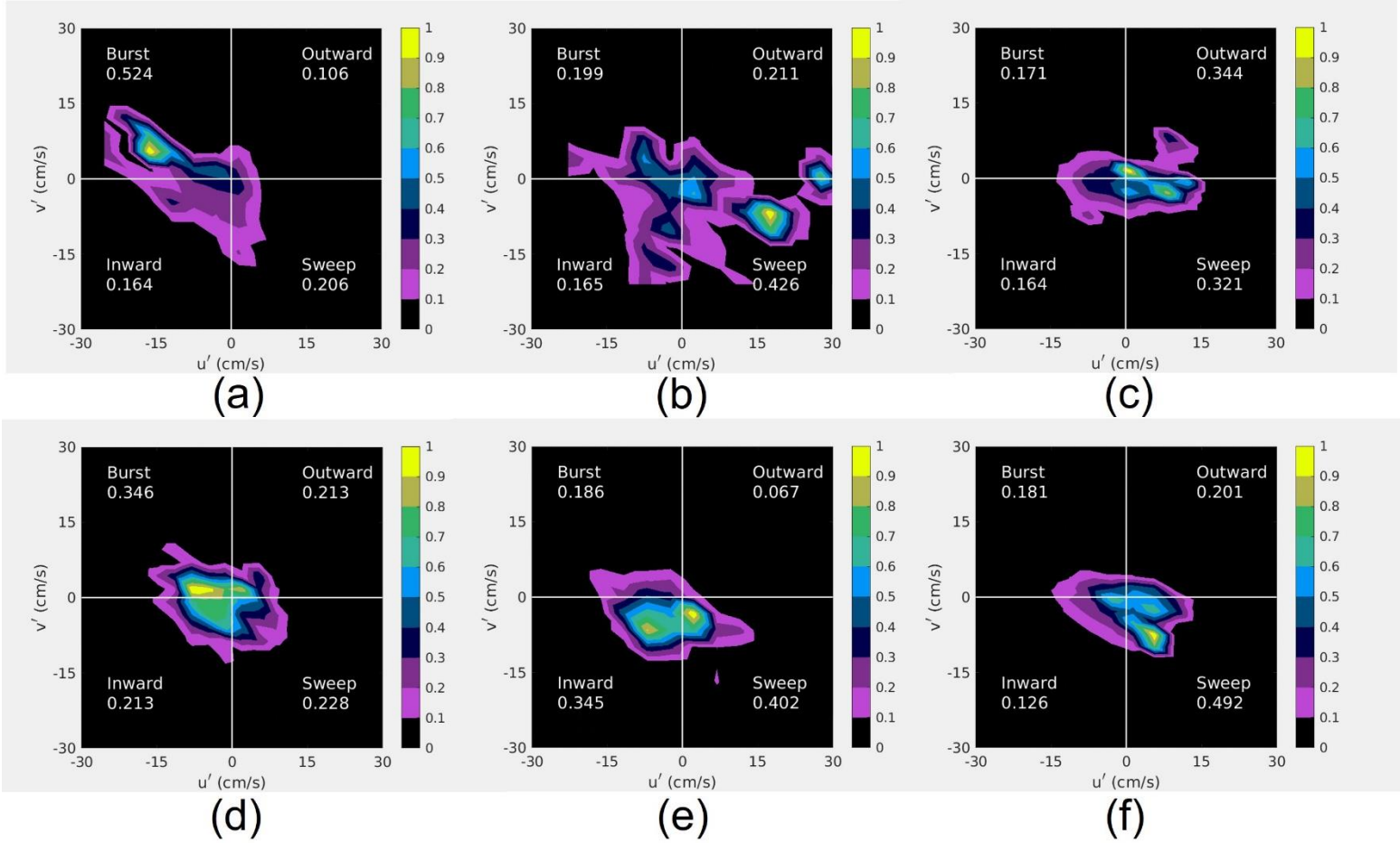


Figure 35. Joint frequency distributions of u' and v' weighted by q_x measured at $x = x_r - 2.5H$ (a, d), x_r (b, e), and $x_r + 5H$ (c, f) for CaseN30 (a-c) and CaseN90 (d-f).

Table 13. Ratio (in percentage) of bedload transport rate during each turbulence event in various BFS angles.

Measurement Point	α (°)	Burst	Sweep	Outward interaction	Inward interaction
$x = x_r - 2.5H$	10	-	-	-	-
	20	-	-	-	-
	30	52.4	20.6	10.6	16.4
	90	34.6	22.8	21.3	21.3
$x = x_r$ $x = x_b$ (CaseN10)	10	38.2	33.2	13.8	14.8
	20	15.6	57.1	16.5	10.9
	30	19.9	42.6	21.1	16.5
	90	18.6	40.2	6.7	34.5
$x = x_r + 2.5H$ $x = x_b + 2.5H$ (CaseN10)	10	31.5	26.4	25.1	17.0
	20	12.0	63.5	19.4	5.1
	30	16.0	50.1	19.9	14.0
	90	18.6	53.8	12.9	14.7
$x = x_r + 5H$ $x = x_b + 5H$ (CaseN10)	10	23.1	32.8	17.5	26.6
	20	14.8	38.3	37.2	9.8
	30	17.1	32.1	34.4	16.4
	90	18.1	49.2	20.1	12.6
$x = x_r + 10H$ $x = x_b + 10H$ (CaseN10)	10	32.0	34.3	18.8	15.0
	20	28.3	37.5	18.6	15.5
	30	24.3	34.0	26.0	15.7
	90	21.8	27.5	33.4	17.3
$x = 25H$	10	27.4	35.2	20.5	16.8
	20	29.8	34.1	20.5	15.6
	30	21.8	34.3	27.7	16.2
	90	21.4	34.4	28.2	16.1

7.2 Submerged wall jet flow with air injection behind sluice gate

In this chapter, the flow and turbulence structures, bedload transport, and the resulting bed profiles are investigated under two conditions: firstly, when air is not injected, and secondly, when air is vertically injected at three different air injection flow rates over three distinct areas, as shown in Table 5. Considering that the sediment transport is primarily driven by the water phase rather than the air phase, all flow variables presented in this chapter are calculated based on the flow velocity multiplied by the Volume of Fluid (VOF) coefficient, n_w . This approach allows the flow variables to represent solely the water behavior influenced by air.

7.2.1 Bed profile and sediment flux

Figures 36-45 illustrate the bed profiles at 10-second intervals for all the simulation cases after the wall jet flow is discharged from the inlet. The scour hole's dimensions are summarized in Table 14. It is observed that, overall, as the air injection volume increases for the same air injection length, both the distance from the end of the apron to the maximum scour depth X_m and to the crest X_d decrease, along with a decrease in the maximum scour depth h_m . Similarly, for the same air injection volume, as the air injection length increases, X_m , X_d , and h_m were shown to be decreased. In CaseRA2Q025 and CaseRA20Q025, the reduction rates for h_m were identified at 51.85% and 53.7%, respectively, whereas a more significantly increased reduction rate for h_m was achieved in CaseRA40Q025 at 72.22%, as illustrated in Figures 37, 40, and 43. The increased

reduction in scour, along with a longer air injection length at the same volumetric air flow rate, can be attributed to the decrease in momentum of the air injection flow, as indicated in Table 5. A similar trend is observed when the air injection volume is doubled ($Q_a/Q_w = 0.5$). In CaseRA2Q05 and CaseRA20Q05, the reduction rates of h_m were calculated as 61.11% and 70.37%, respectively. In CaseRA40Q05, the reduction rate of the scour depth was shown to be 85.19%. This can be seen in Figures 38, 41, and 44. The tendency of the increasing scour reduction rate is also in line with the decreases of the momentum of air flow. In the cases (CaseRA2Q1, CaseRA20Q1, and CaseRA40Q1) where the air injection volume is equal to the water inflow volume, the reduction rate of h_m was quantified as 90.74%, 87.03%, and 88.89%, respectively, as shown in Figures 39, 42, and 45. At this volumetric air flow rate ($Q_a/Q_w = 1$), no notable trend was observed in the scour reduction rate along with the decreasing momentum of air flow. The simulation results above indicates that scour mitigation can be achieved through increasing the air injection flow rate and the injection area.

In addition, scour volume V_s was quantified by subtracting the total volume of the remaining DEM particles at the end of simulation from the initial sediment volume over the range from $x=0$ to the point where the bed profile intersects with $y=0$. Overall, the trend of V_s is consistent with h_m , as shown in Table 14. V_s was found to decrease by 90.74% in CaseRA2Q1, 87.03% in CaseRA20Q1, and 88.89% in CaseRA40Q1.

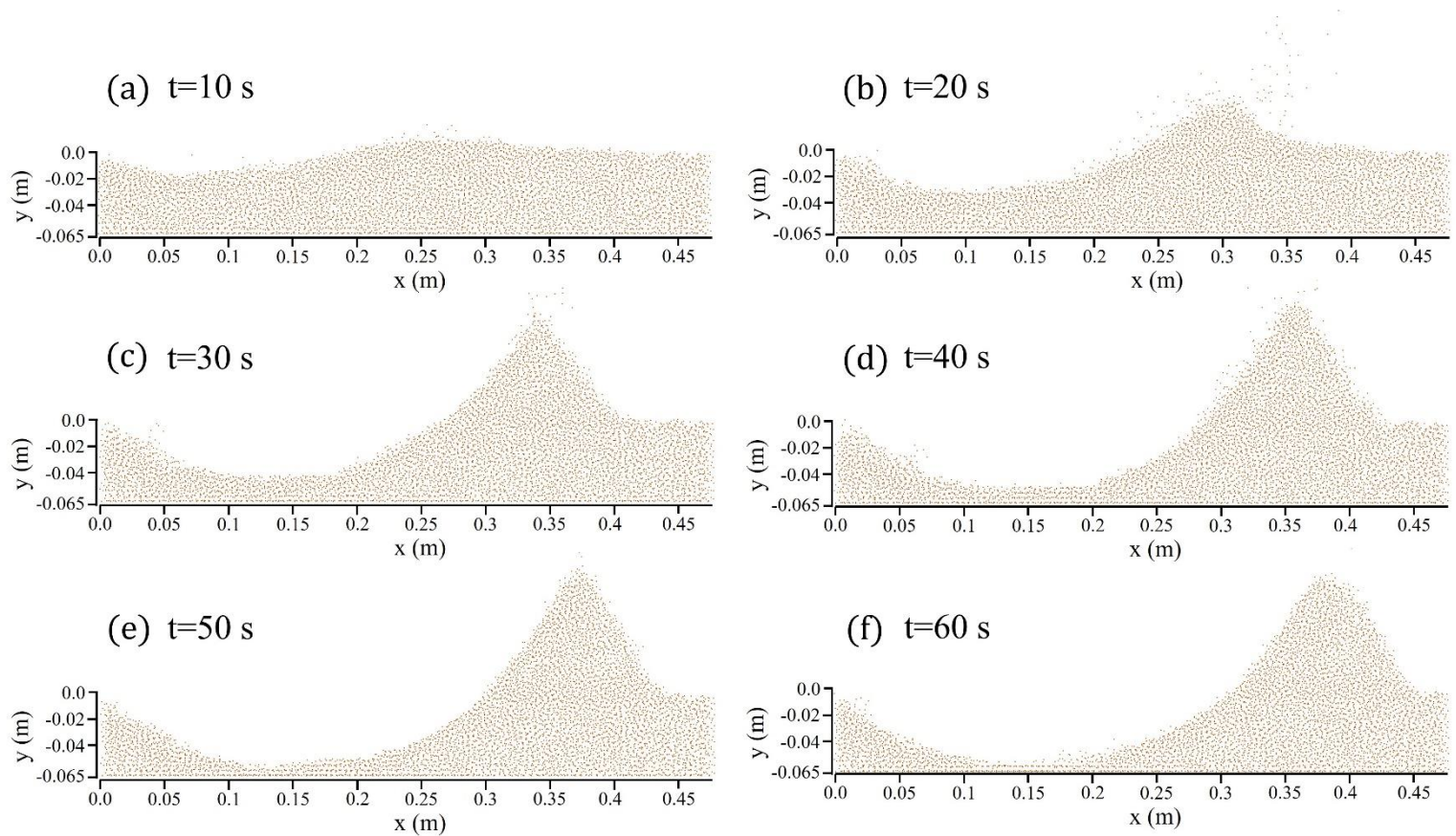


Figure 36. Bedform changes over time in CaseNA.

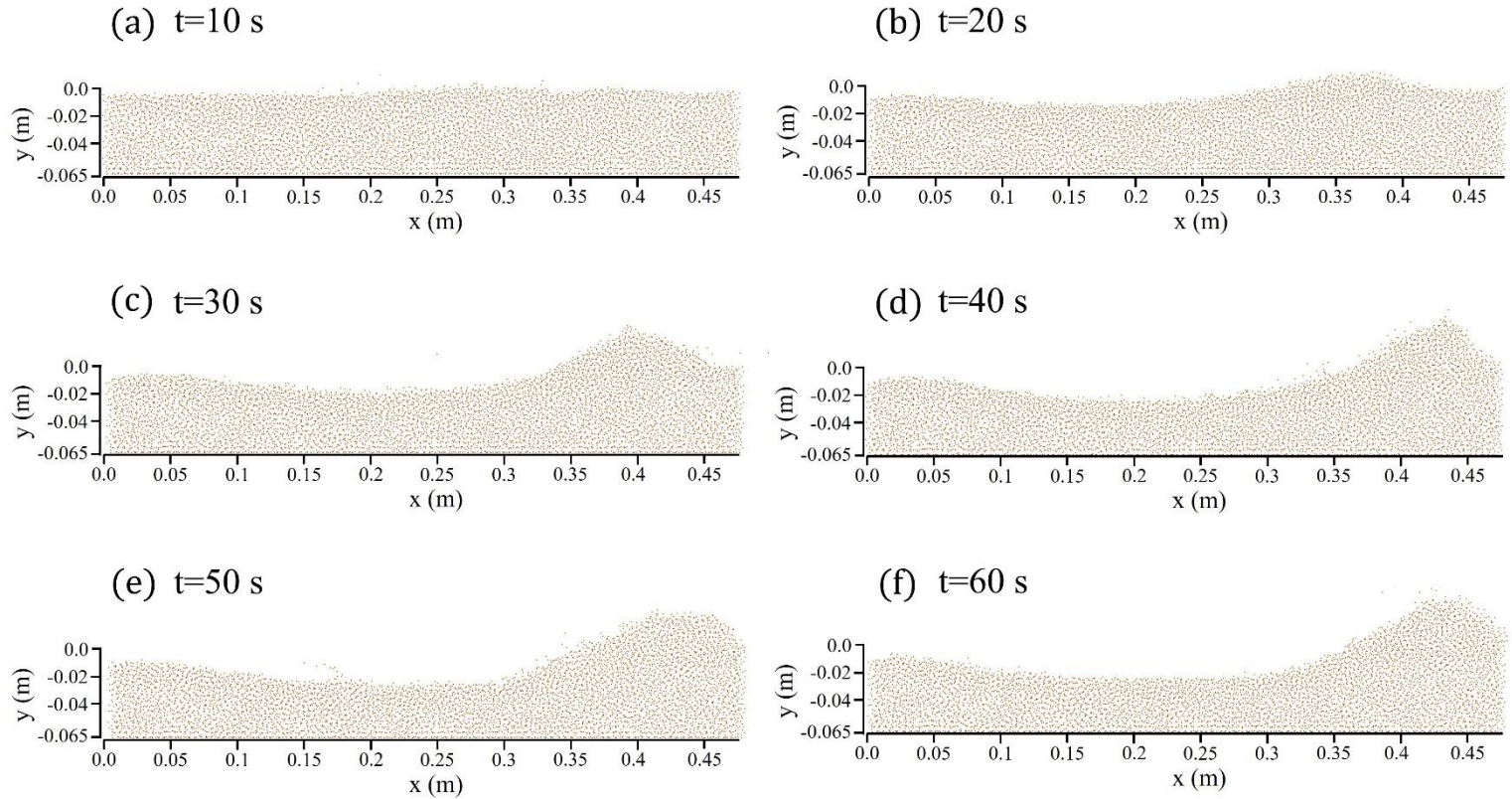


Figure 37. Bedform changes over time in CaseRA2Q025.

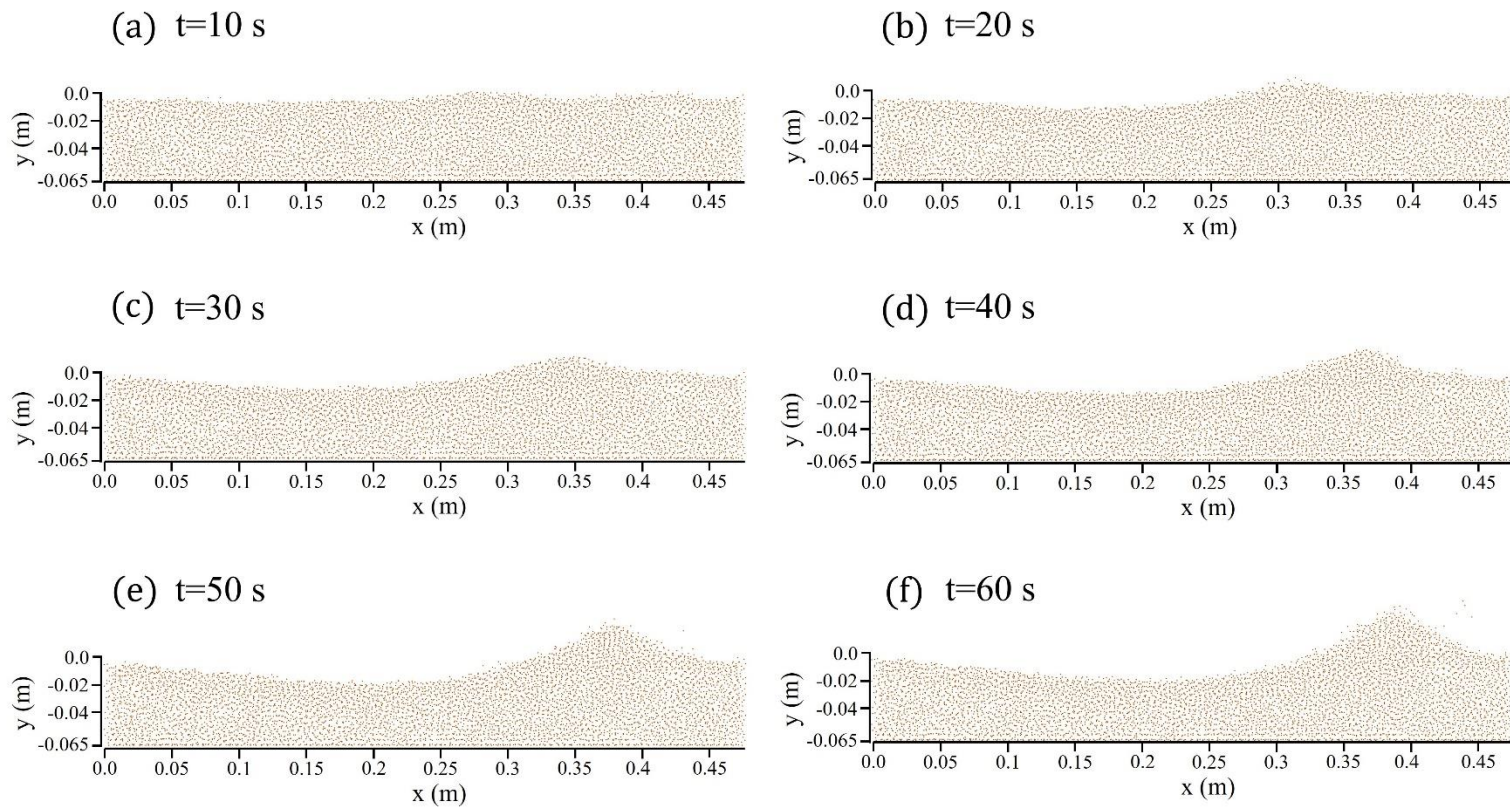


Figure 38. Bedform changes over time in CaseRA2Q05.

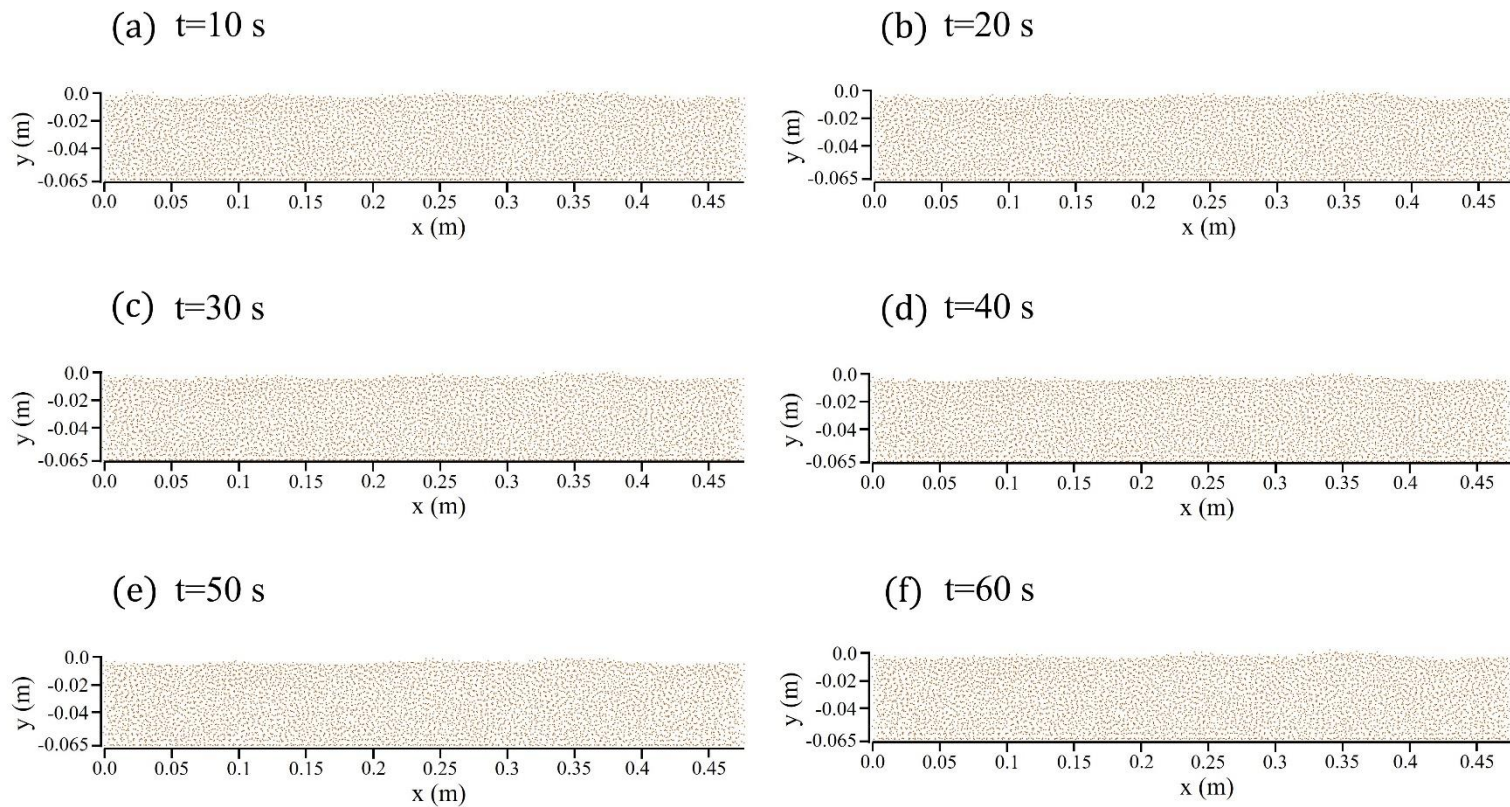


Figure 39. Bedform changes over time in CaseRA2Q1.

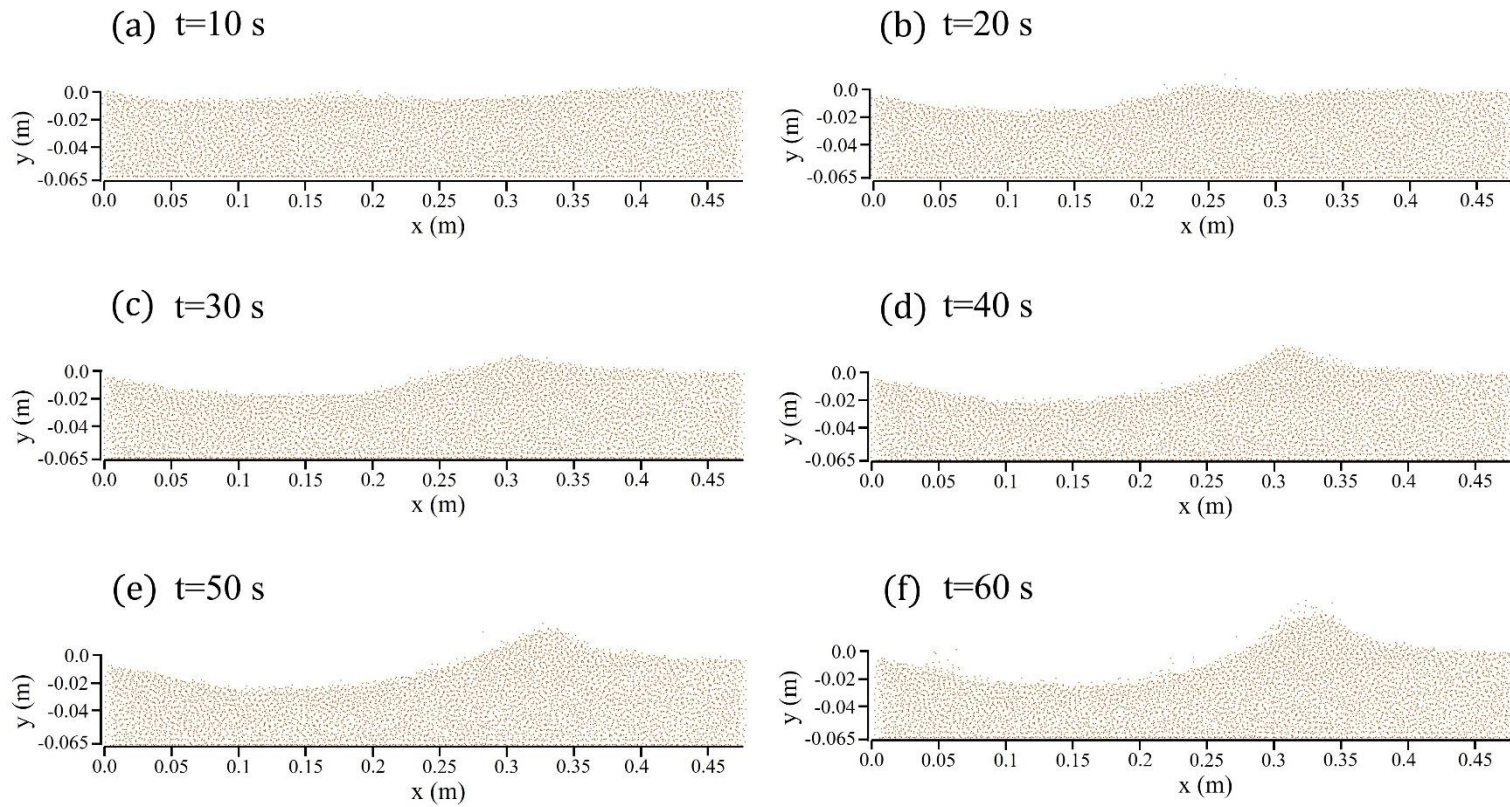


Figure 40. Bedform changes over time in CaseRA20Q025.

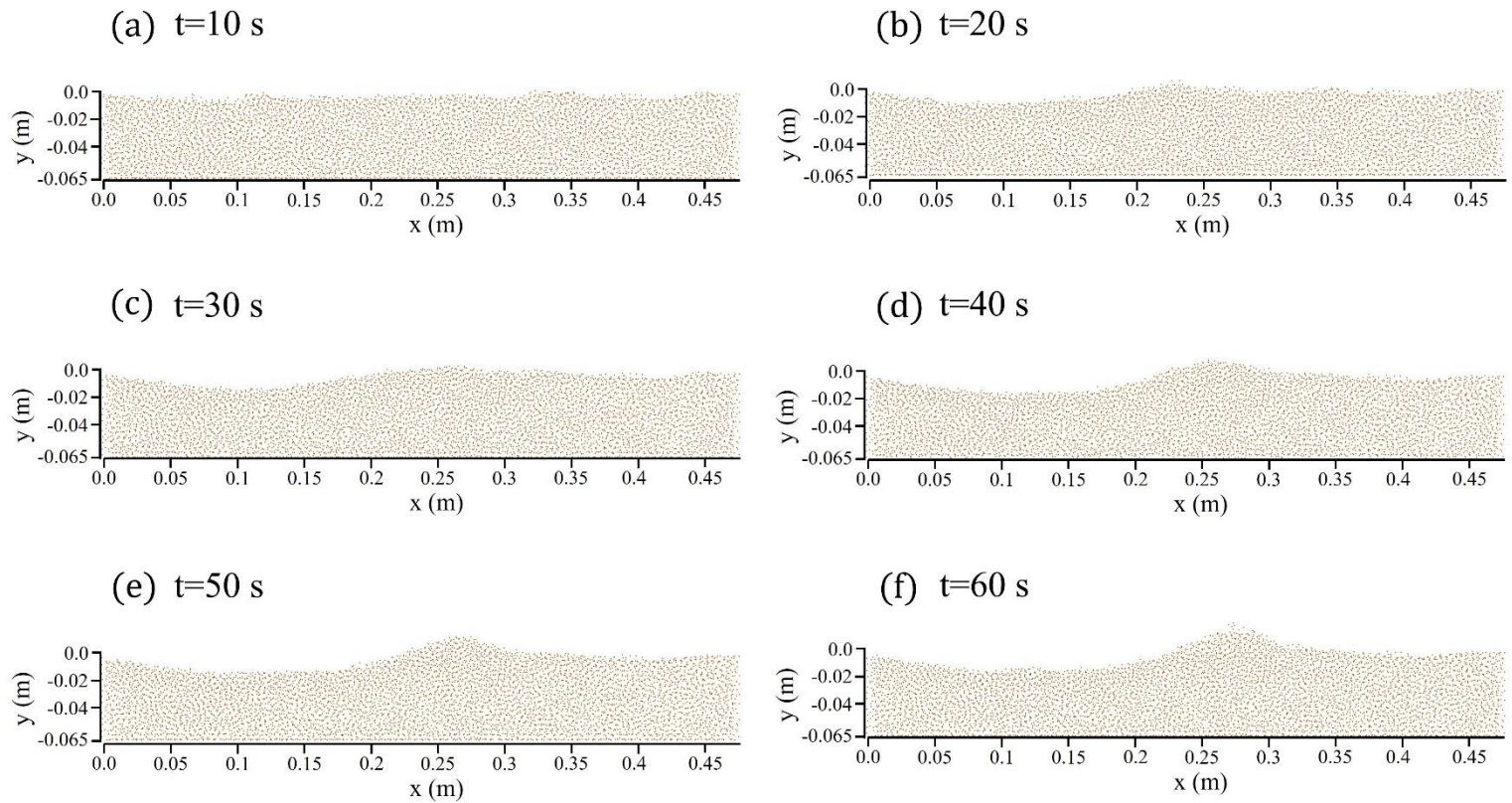


Figure 41. Bedform changes over time in CaseRA20Q05.

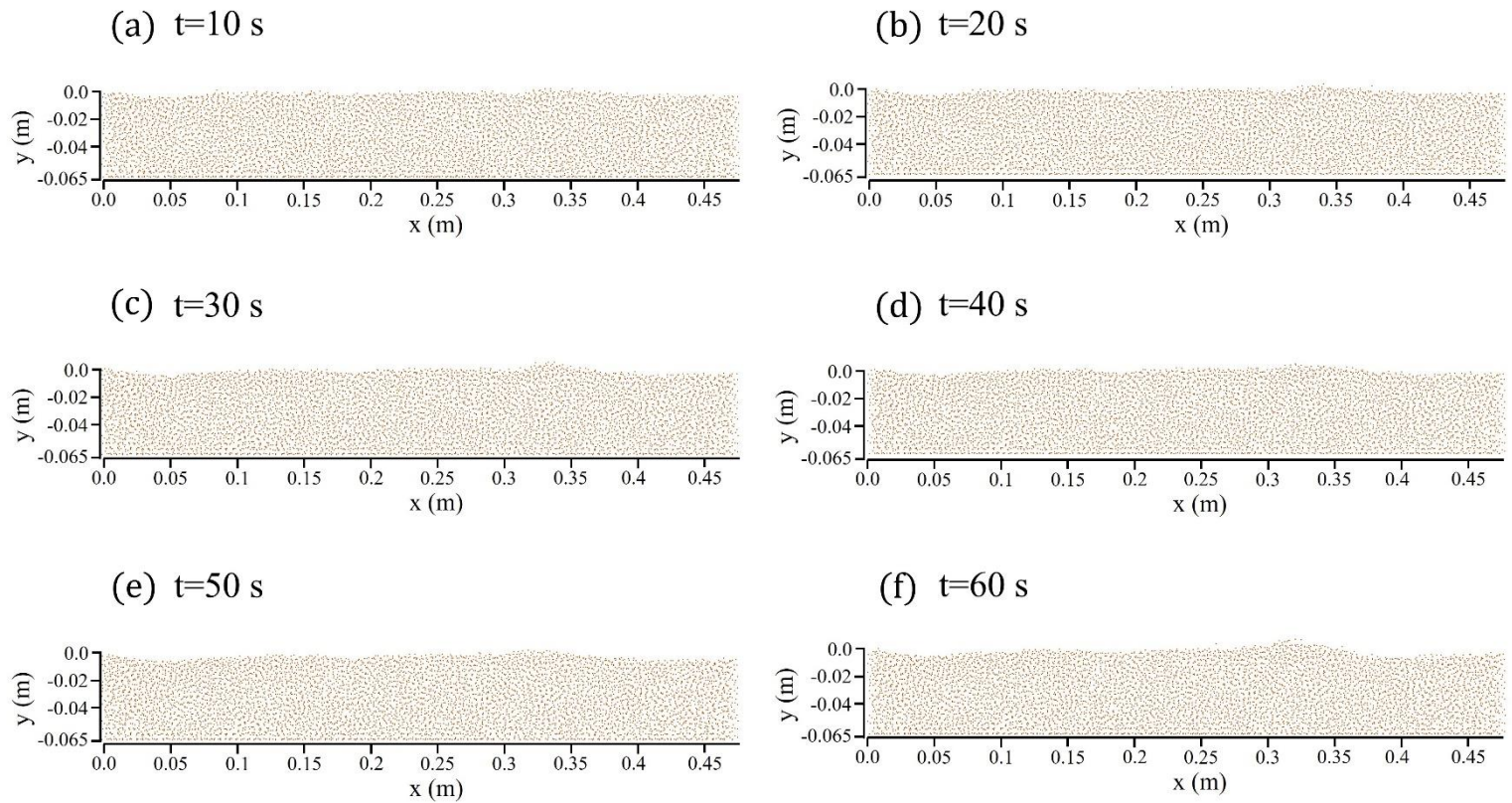


Figure 42. Bedform changes over time in CaseRA20Q1.

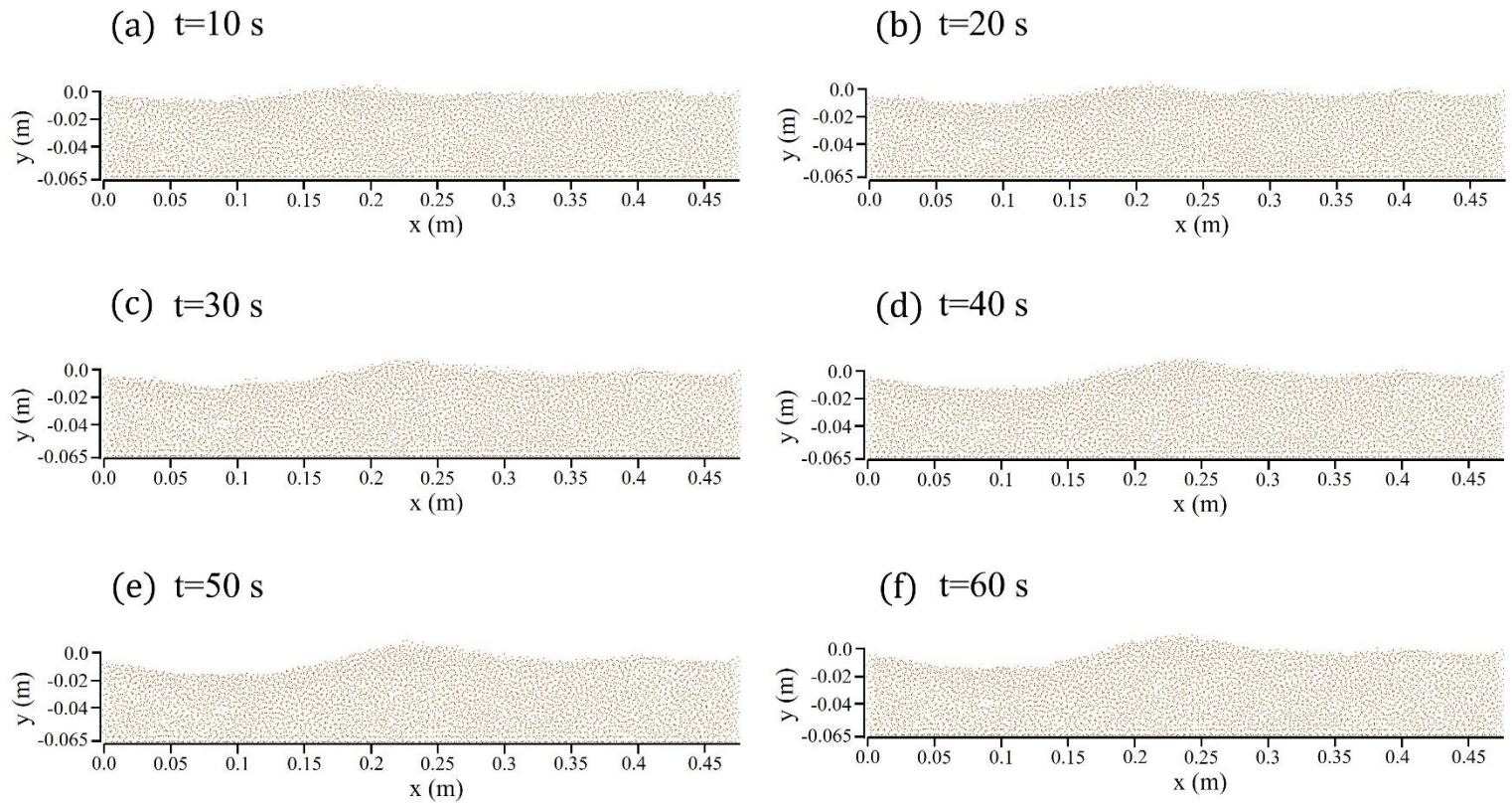


Figure 43. Bedform changes over time in CaseRA40Q025.

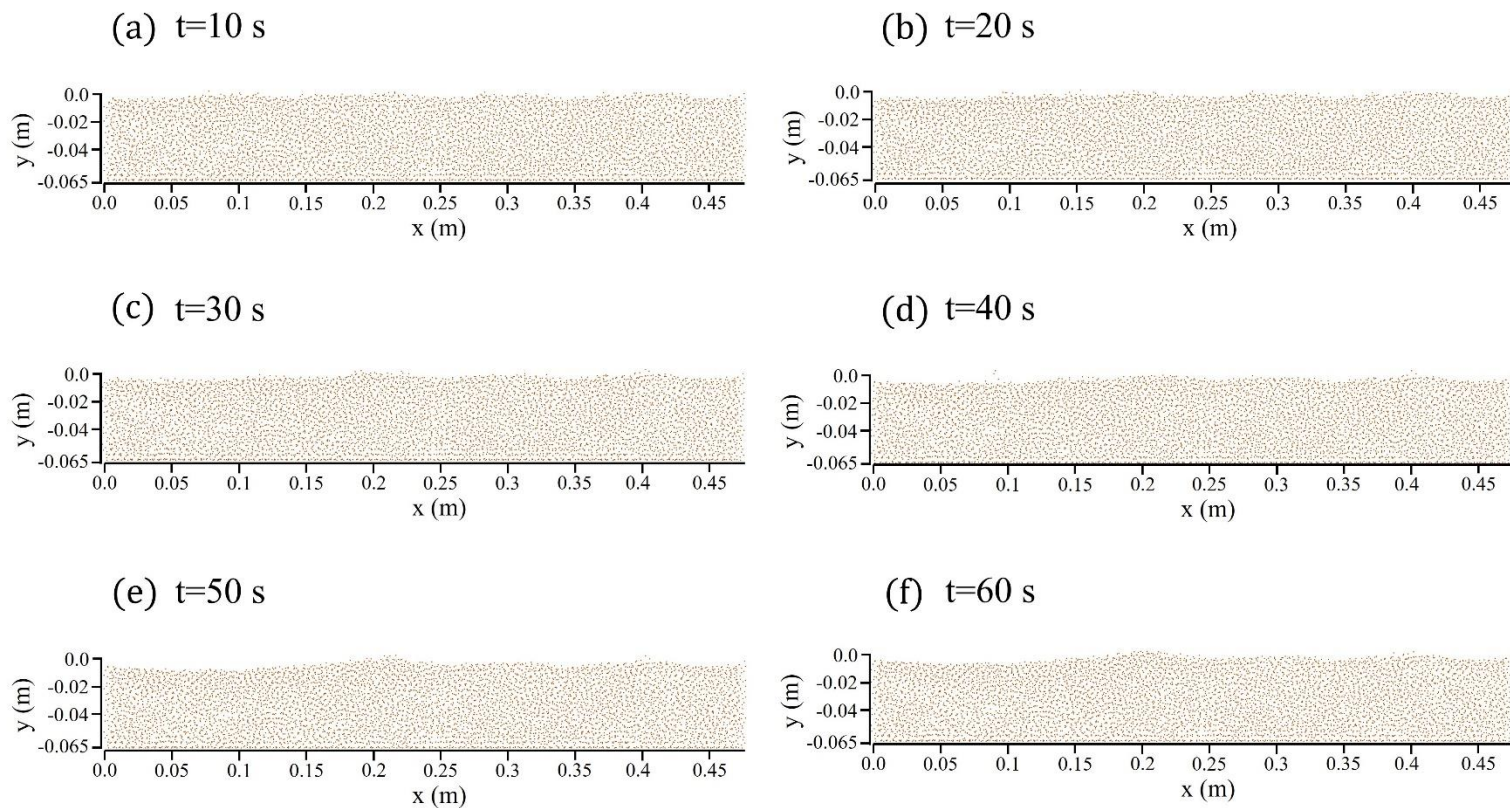


Figure 44. Bedform changes over time in CaseRA40Q05.

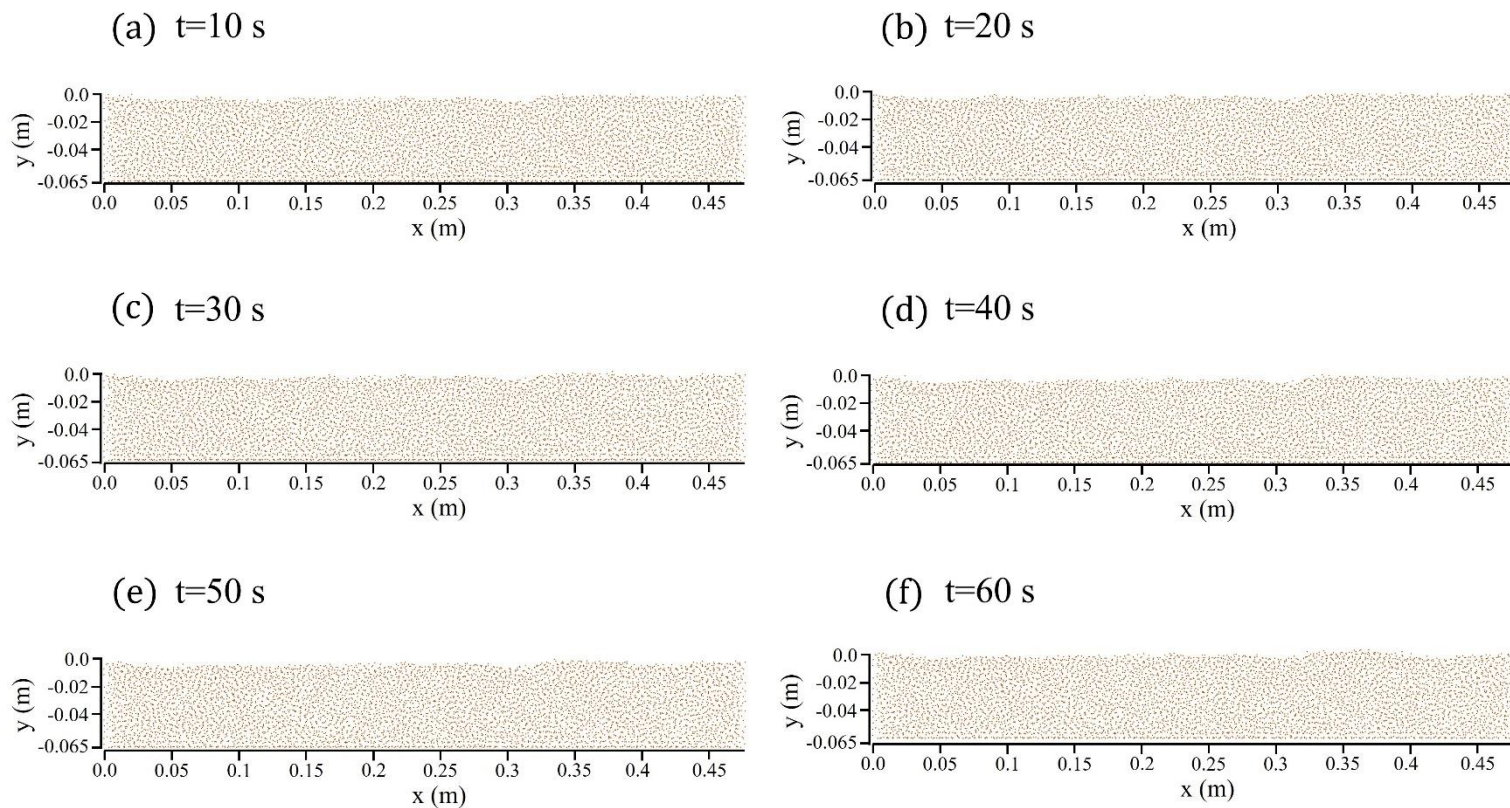


Figure 45. Bedform changes over time in CaseRA40Q1.

Figures 46-48 depict the spatial distribution of mean bedload transport rate Q_x at 10-second intervals (averaged over 10 seconds) for $RA=2, 4$, and 40 cm, respectively. For CaseNA where there is no air injection, Q_x fluctuates considerably as the local scour occurs quickly. In this case, the bedload transport rate reached its maximum between 10 and 20 s. This period is the time when the initial scouring occurs rapidly, as shown in Figures 36a and 36b. As the air injection flow rate and injection length increases, the bedload transport rate was shown to be decreased significantly at all time intervals. In CaseRA2Q025 and CaseRA2Q05, which feature the shortest air injection lengths among all the simulation cases, Q_x was quantified significantly high downstream, with respect to Figure 46. This result is consistent with the bed profiles in Figures 37 and 38, where X_d is relatively longer than in the other simulation cases. For CaseRA2Q1, the bedload transport rate was quantified as the smallest compared to CaseRA2Q025 and CaseRA2Q05, leading to significantly small scour depth, as shown in Figure 39.

In CaseRA20, Q_x was shown to be smaller than CaseRA2 for all the air injection flow rates, as shown in Figure 47. The peak of Q_x is observed upstream of $x = 0.33$ m, which results in X_d before that point, as shown in Figure 41. For CaseRA20Q1, Q_x was quantified as very small, with quite small scour, as shown in Figure 42. In CaseRA40, Q_x was quantified considerably lower than in CaseRA2 and CaseRA20 for all the air injection flow rates, as shown in Figure 48. It is noteworthy that Q_x is notably small in CaseRA40Q025 compared to Q_x in CaseRA2Q025 and CaseRA20Q025. This implies that the wide-area air injection approach can substantially reduce sediment flux with a low air injection flow rate. Similar to CaseRA2Q1 and CaseRA20Q1, Q_x in CaseRA40Q1 was calculated as significantly small.

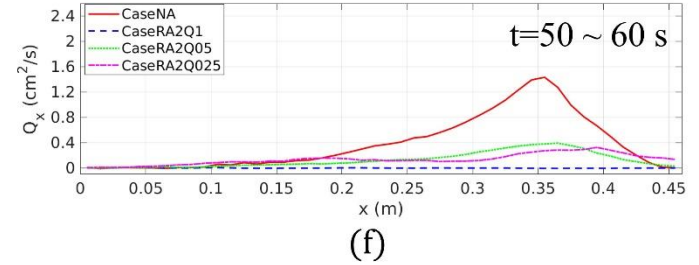
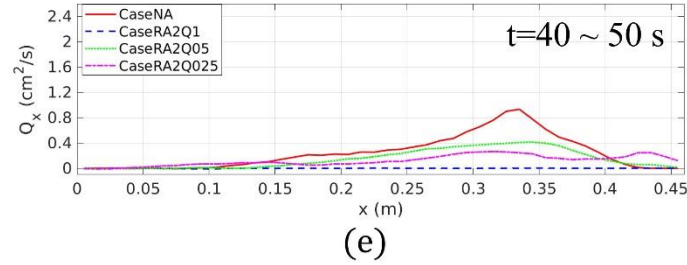
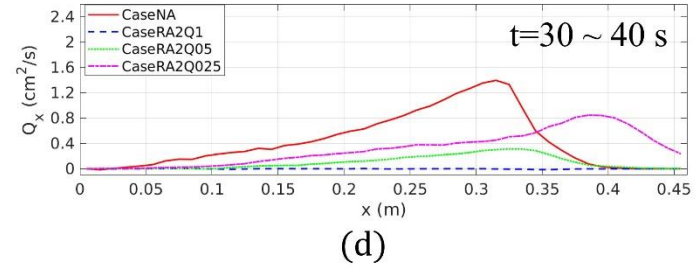
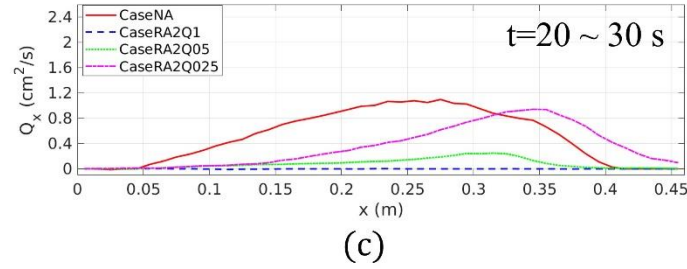
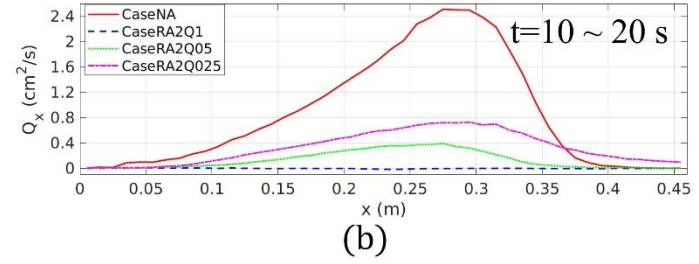
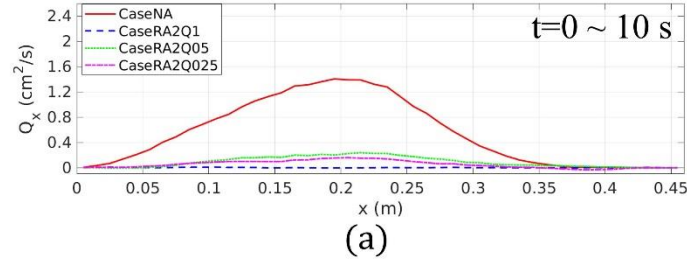


Figure 46. Comparison of bedload transport rate at various time intervals for CaseNA and CaseRA2Q025-Q1.

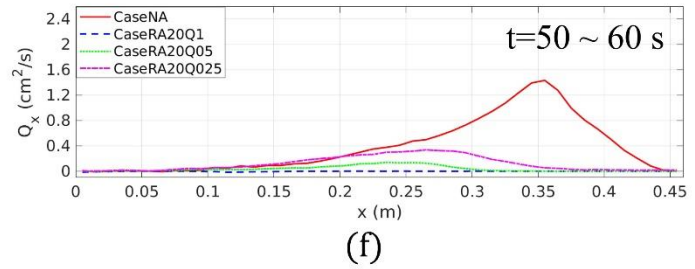
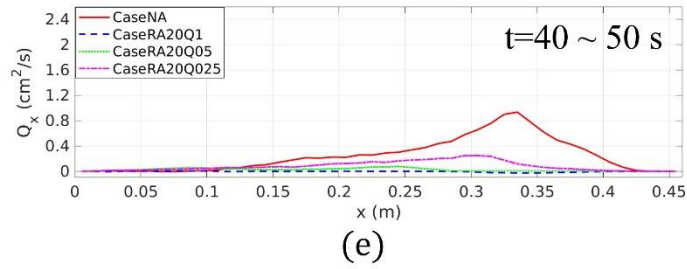
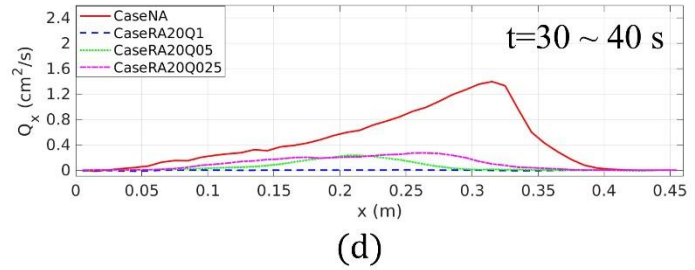
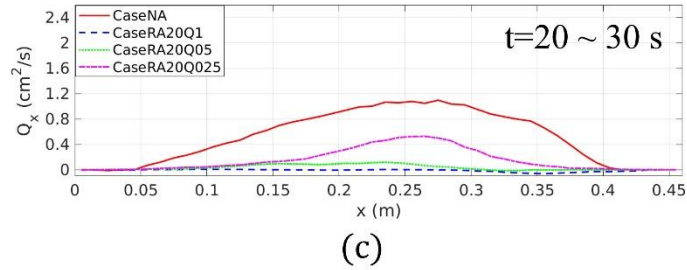
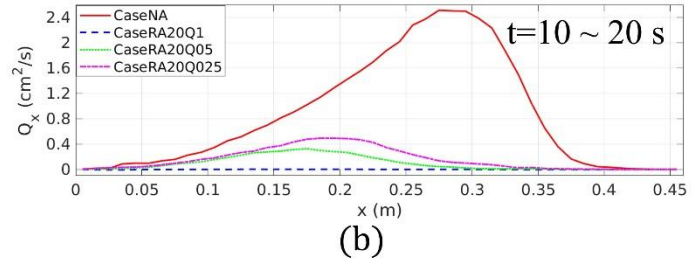
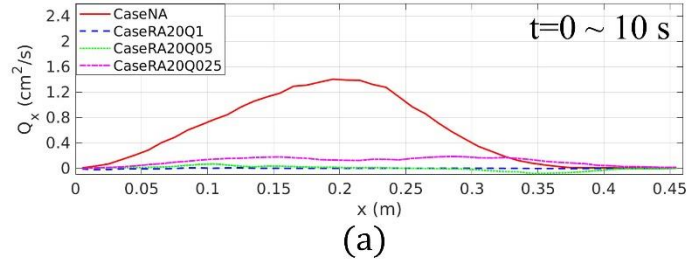


Figure 47. Comparison of bedload transport rate at various time intervals for CaseNA and CaseRA20Q025-Q1.

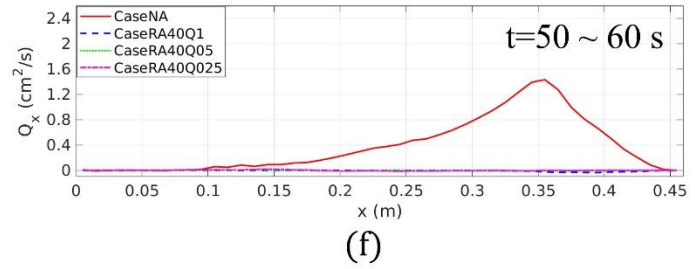
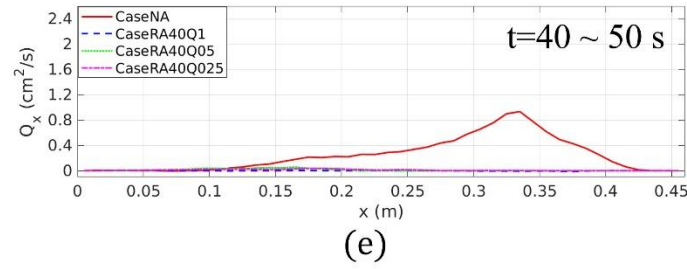
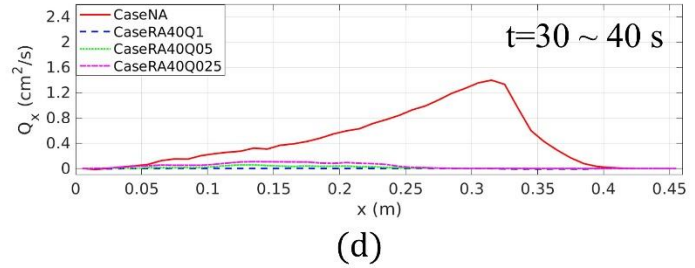
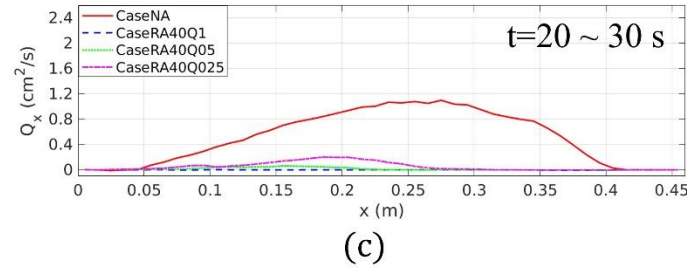
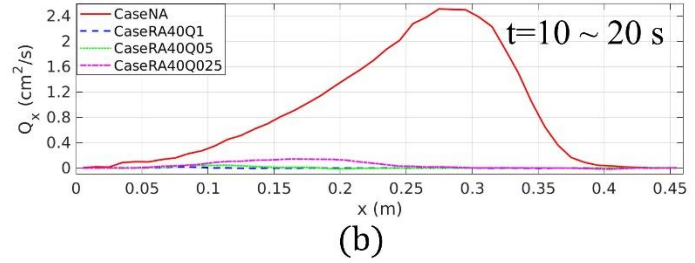
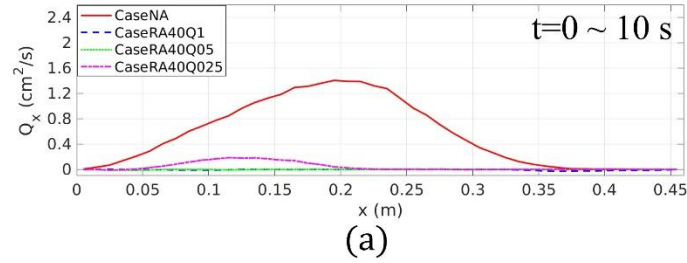


Figure 48. Comparison of bedload transport rate at various time intervals for CaseNA and CaseRA40Q025-Q1.

Table 14. Dimensions of scour hole with and without air injection in the central vertical plane.

RUN	X _m (m) Rate of change (%)	X _d (m) Rate of change (%)	h _m (m) Rate of change (%)	V _s (cm ³) Rate of change (%)
CaseNA	0.151	0.371	0.054	1.041
	-	-	-	-
CaseRA2Q025	0.21	0.418	0.026	0.518
	39.07	12.67	-51.85	-50.24
CaseRA2Q05	0.206	0.374	0.021	0.325
	36.42	0.81	-61.11	-68.78
CaseRA2Q1	0.166	0.33	0.005	0.035
	9.93	-11.05	-90.74	-96.64
CaseRA20Q025	0.154	0.31	0.025	0.363
	1.99	-16.44	-53.70	-65.13
CaseRA20Q05	0.134	0.27	0.016	0.18
	-11.26	-27.22	-70.37	-82.71
CaseRA20Q1	0.046	0.106	0.007	0.027
	-69.54	-71.43	-87.03	-97.41
CaseRA40Q025	0.102	0.226	0.015	0.126
	-32.45	-39.08	-72.22	-87.90
CaseRA40Q05	0.09	0.19	0.008	0.043
	-40.40	-48.79	-85.19	-95.87
CaseRA40Q1	0.046	0.07	0.006	0.037
	-69.54	-81.13	-88.89	-96.45

7.2.2 Flow and turbulence structures

To properly understand the mechanism of the mitigation of local scour due to air injection presented in the previous chapters, it is necessary to investigate the flow and turbulence structure over the apron and sediment zone. Figures 49a and 49b respectively represent the mean streamwise velocity U and turbulent kinetic energy (TKE) contours over the scour hole at the end of the simulation in CaseNA. As the wall jet flow passes over the apron and enters the scour hole, flow separation occurs at the front of the stoss side. The propagating jet flow moves along the stoss side of the dune and gradually subsides thereafter. On the stoss side, a large TKE zone is formed along with the flow velocity, promoting the scour process. On the lee side, it is observed that both flow velocity and TKE are minimal. A more detailed analysis of the flow structure is presented including the air injection cases.

Figures 50-59 display the streamwise and vertical mean velocities U and V , and turbulence intensities $TI_x \left(\sqrt{\langle u'^2 \rangle} / U_a \right)$ and $TI_y \left(\sqrt{\langle v'^2 \rangle} / U_a \right)$ for all the simulation cases. In the vector diagram without air injection (Figure 50a), two circular flows (in red circles) are formed: the first one is created at the midpoint of the apron due to the water jet discharged from the gate (inlet), and the second one is formed in the scour zone due to the flow that climbs up the stoss side of the dune crest. In CaseNA, as the bed slope increases due to the initial scouring process, flow separation is observed near the bed from $x=0$ to $x=0.1\text{m}$ (indicated by the blue circle in Figure 50a). It can be inferred that the scour process is accelerated by the development of the backflow occurring in this separation zone. The

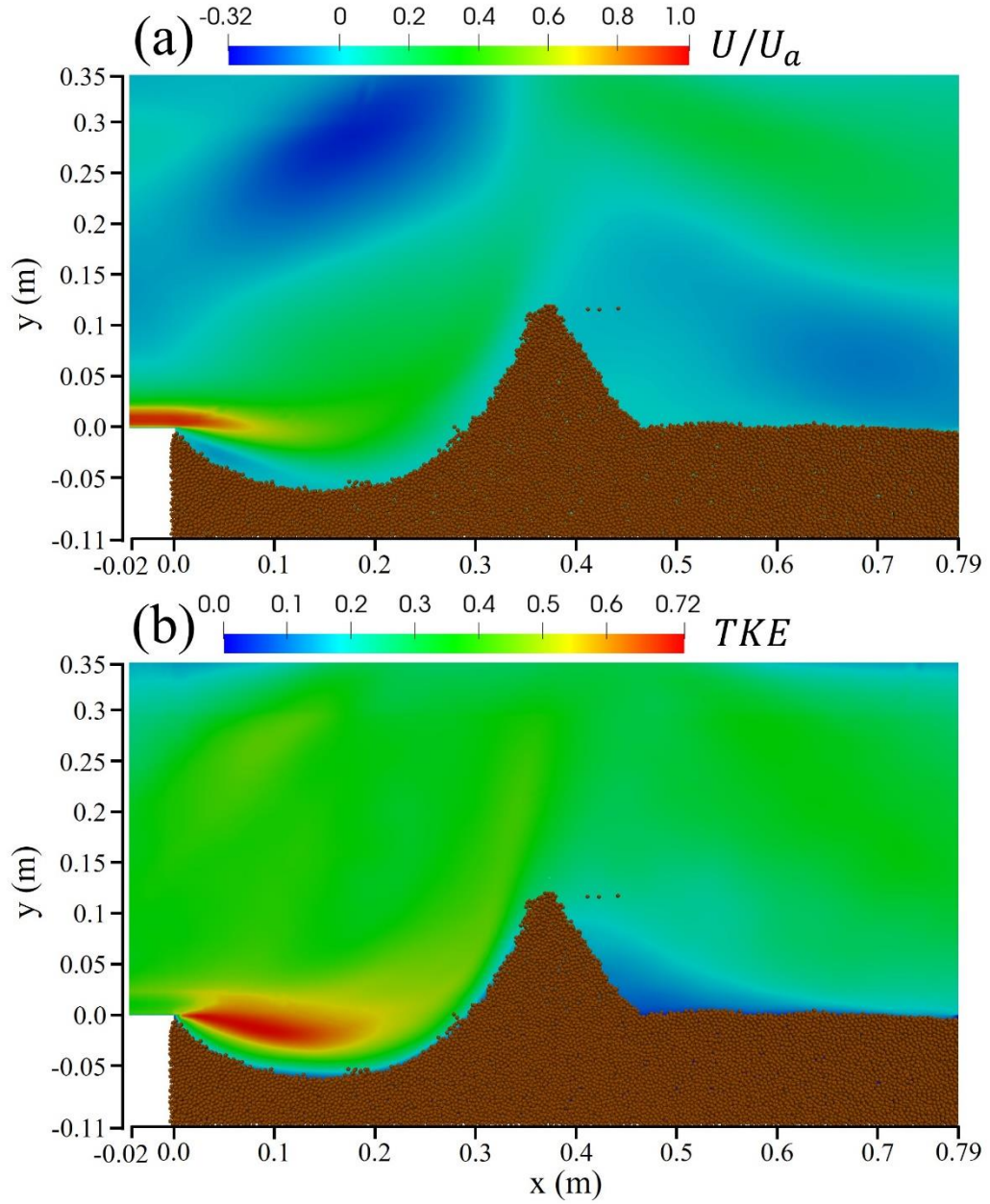


Figure 49. Comparison of mean velocity (a) and turbulent kinetic energy (b) contours in the central vertical plane ($z/W=0.5$) for CaseNA.

mean vertical velocity V is increased on the right side and decreased on the left side of the second vortex core. The turbulence intensities TI_x and TI_y reach their maximum right behind the apron due to the flow separation.

As shown in Figures 51-53 for CaseRA2, two primary vortex cores, indicated by red circles, are observed, similar to CaseNA. The second vortex core exhibited a tendency to move slightly upstream as the air injection rate increased from Q025 to Q1. This can be interpreted as the result of the propagating flow near the apron being deflected upward due to the vertical air injection, which promotes vortex formation. As shown in the figures, the mean streamwise velocity U at the end of the apron ($x = 0$) significantly decreased due to the air injection, especially in CaseRA2Q1 where the air injection flow rate is equal to the inflowing water flow rate. It was shown that TI_x also notably decreased, as shown in Figure 53c. It can be conjectured that the significant mitigation of the scour in Figure 39 is attributed to this decreased U and TI_x at $x = 0$. V is shown to increase along the upward flow on the right side of the second vortex core and decreases on the left side of the core, with reference to Figures 51b-53b. TI_y develops above the sediment zone due to the air injection, as shown in Figures 51d-53d.

The velocity vectors in Figures 54a-56a for CaseRA20 also demonstrate two primary vortex cores. Similar to CaseRA2, the second vortex core exhibited a tendency to move slightly upstream as the air injection flow rate increased. The mean streamwise velocity near the wall decreased notably compared to CaseRA2, which can be attributed to the pre-agitation of the jet flow due to the early air injection. In CaseRA20Q025 and CaseRA20Q05, TI_x near the wall exhibited strong development beyond the end of the

apron, inducing scour process to some extent, as indicated in Figures 40 and 41. However, in CaseRA20Q1, TI_x was found to not strongly develop beyond the end of the apron, leading to significant scour mitigation, as shown in Figure 42. V is found to increase along the upward flow on the right side of the second vortex core and decreases on the left side of the core, regarding Figures 54b-56b. TI_y develops above the sediment zone in larger area than CaseRA2 due to the wider air injection (from $x = -20$ cm to 0), as shown in Figures 54d-56d.

In CaseRA40, it was observed that both the first and second vortex cores are positioned even further upstream compared to CaseRA2 and CaseRA20, as shown in Figures 57a-59a. This can be attributed to the faster deflection of the wall jet flow due to the longer air injection length (from $x = -40$ cm to 0), beginning further upstream than CaseRA2 and CaseRA20. Due to the faster disruption of the wall jet caused by the wide-area injection, both U and TI_x significantly decreased, as indicated in Figures 57a-59a and Figures 57c-59c, compared to CaseRA2 and CaseRA20 at all the air injection flow rate Q025, Q05, and Q1. V is shown to increase along the upward flow on the right side of the second vortex core and decreases on the left side of the core, with reference to Figures 57b-59b. TI_y shows high values above the sediment zone due to the air injection, similar to CaseRA20, as shown in Figures 57d-59d.

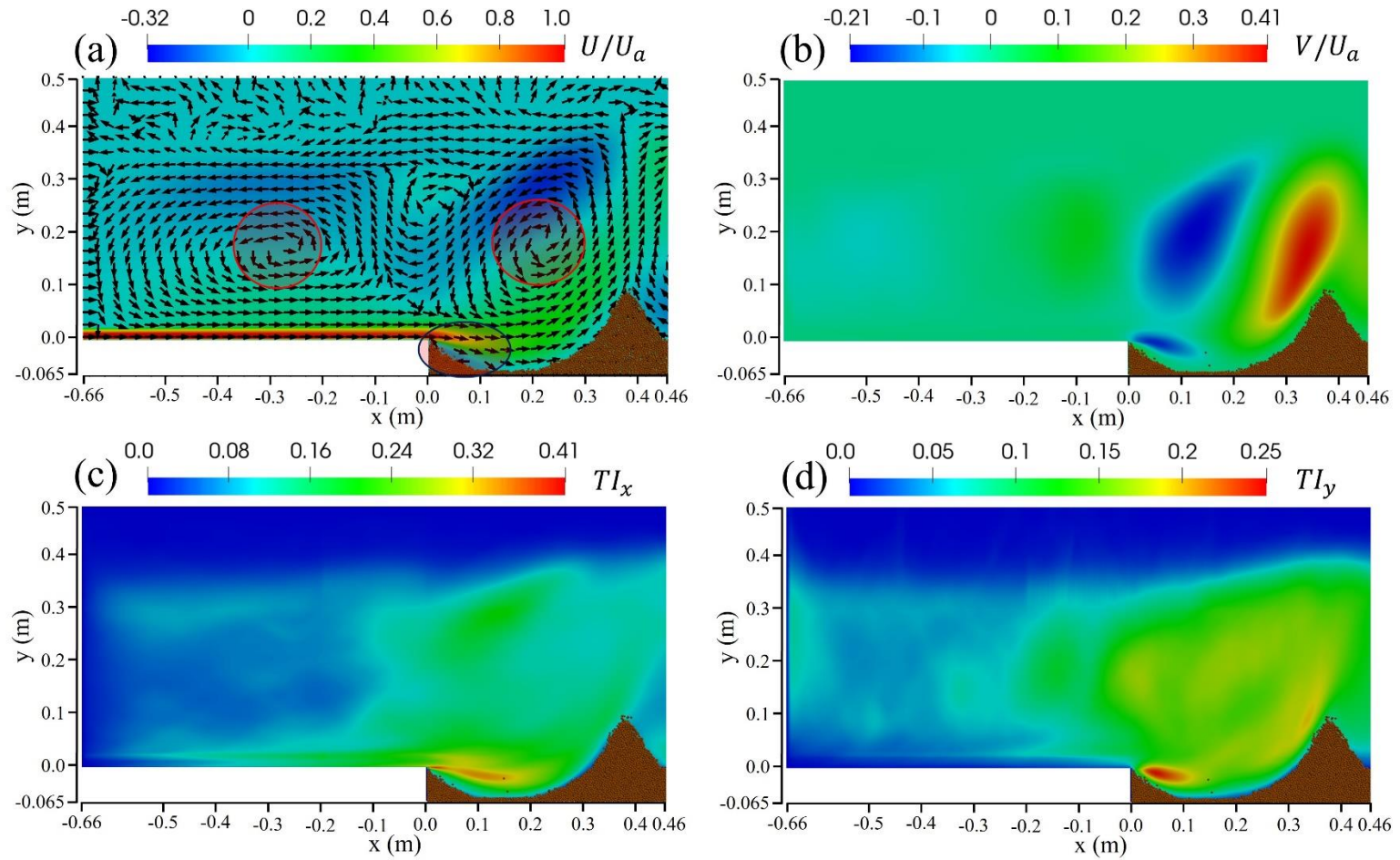


Figure 50. Comparison of mean velocity (a) and turbulent kinetic energy (b) contours in the central vertical plane ($z/W=0.5$) for CaseNA.

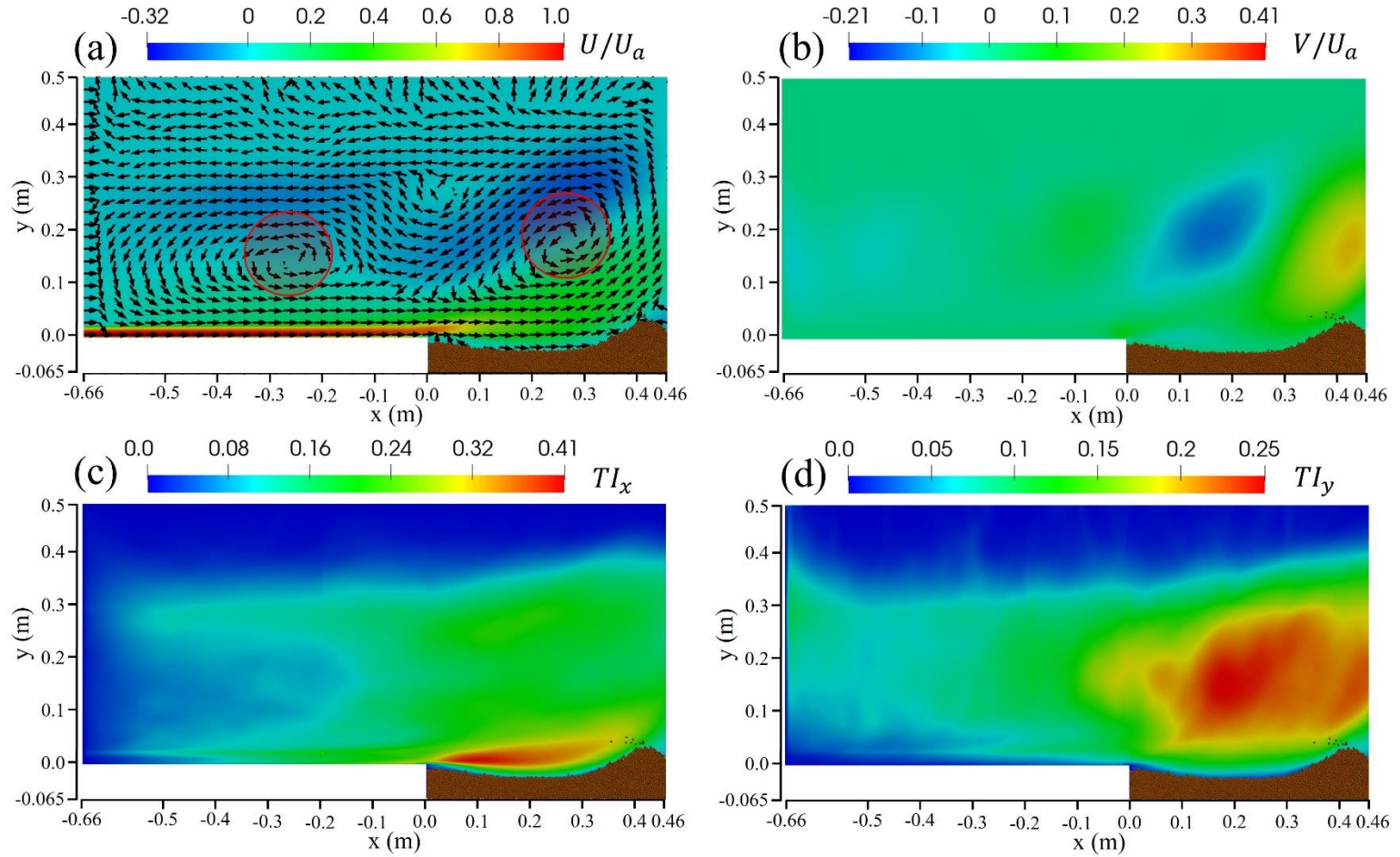


Figure 51. Comparison of mean velocity (a, b) and turbulence intensity (c, d) contours in the central vertical plane ($z/W=0.5$) for CaseRA2Q025.

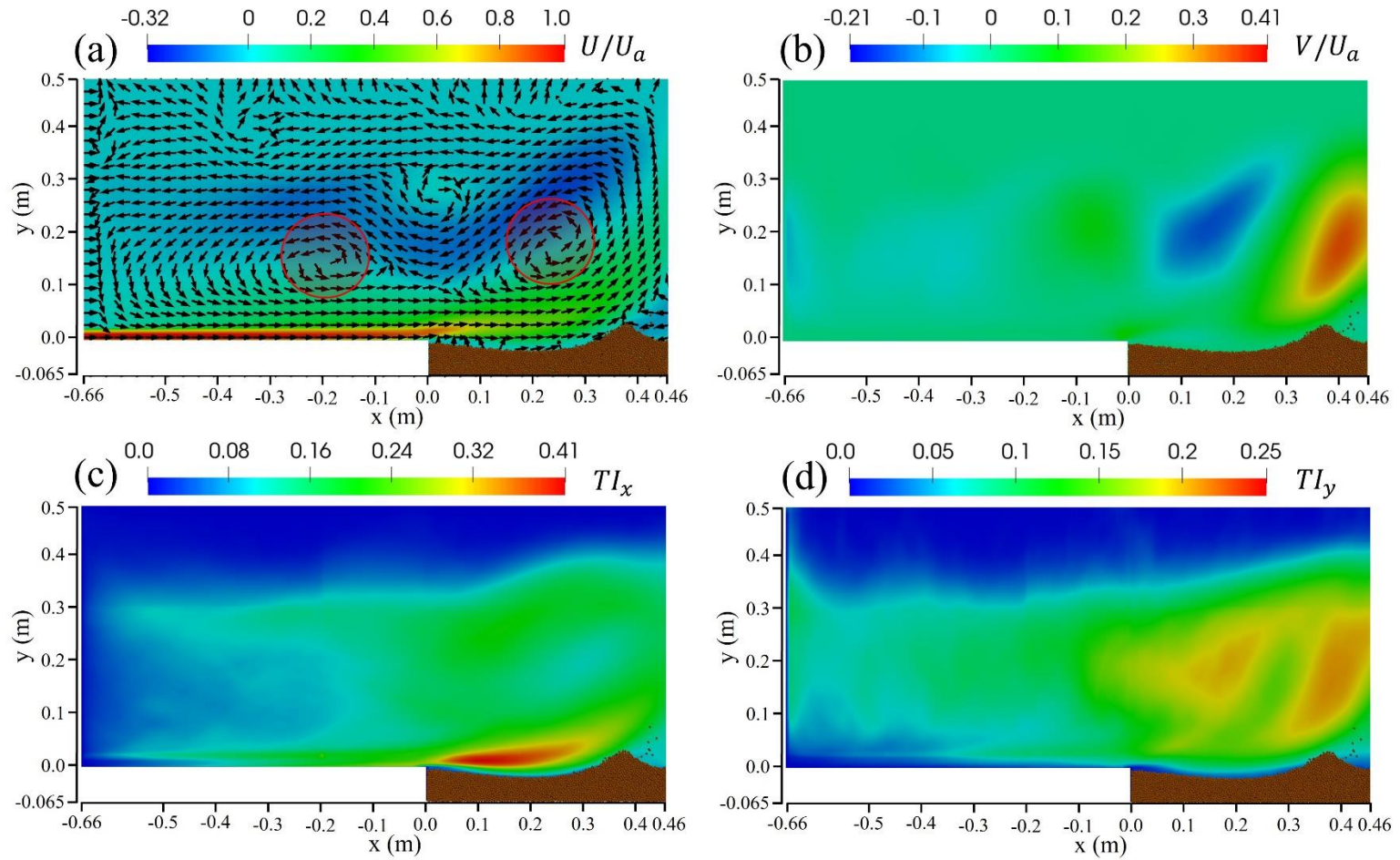


Figure 52. Comparison of mean velocity (a, b) and turbulence intensity (c, d) contours in the central vertical plane ($z/W=0.5$) for CaseRA2Q05.

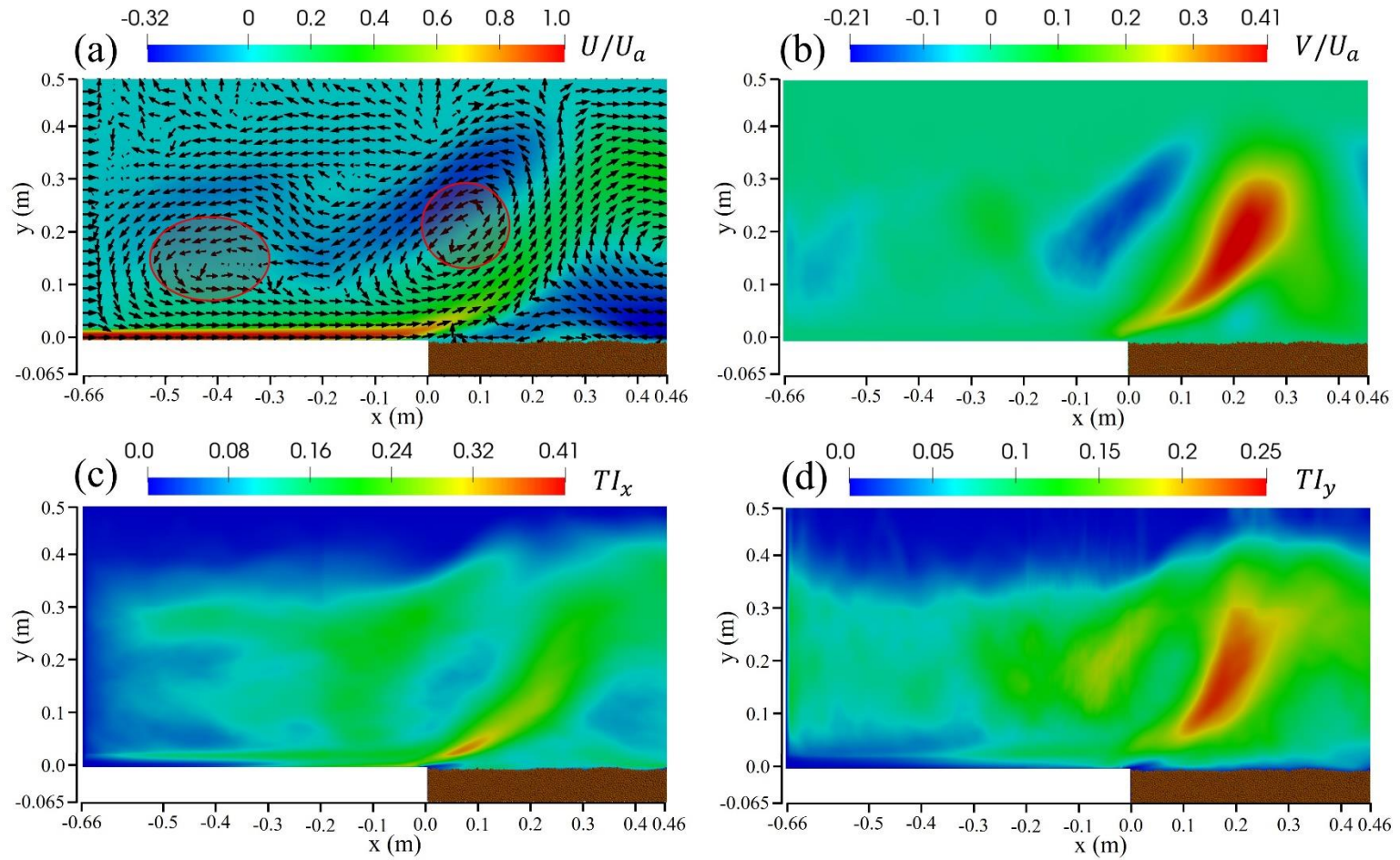


Figure 53. Comparison of mean velocity (a, b) and turbulence intensity (c, d) contours in the central vertical plane ($z/W=0.5$) for CaseRA2Q1.

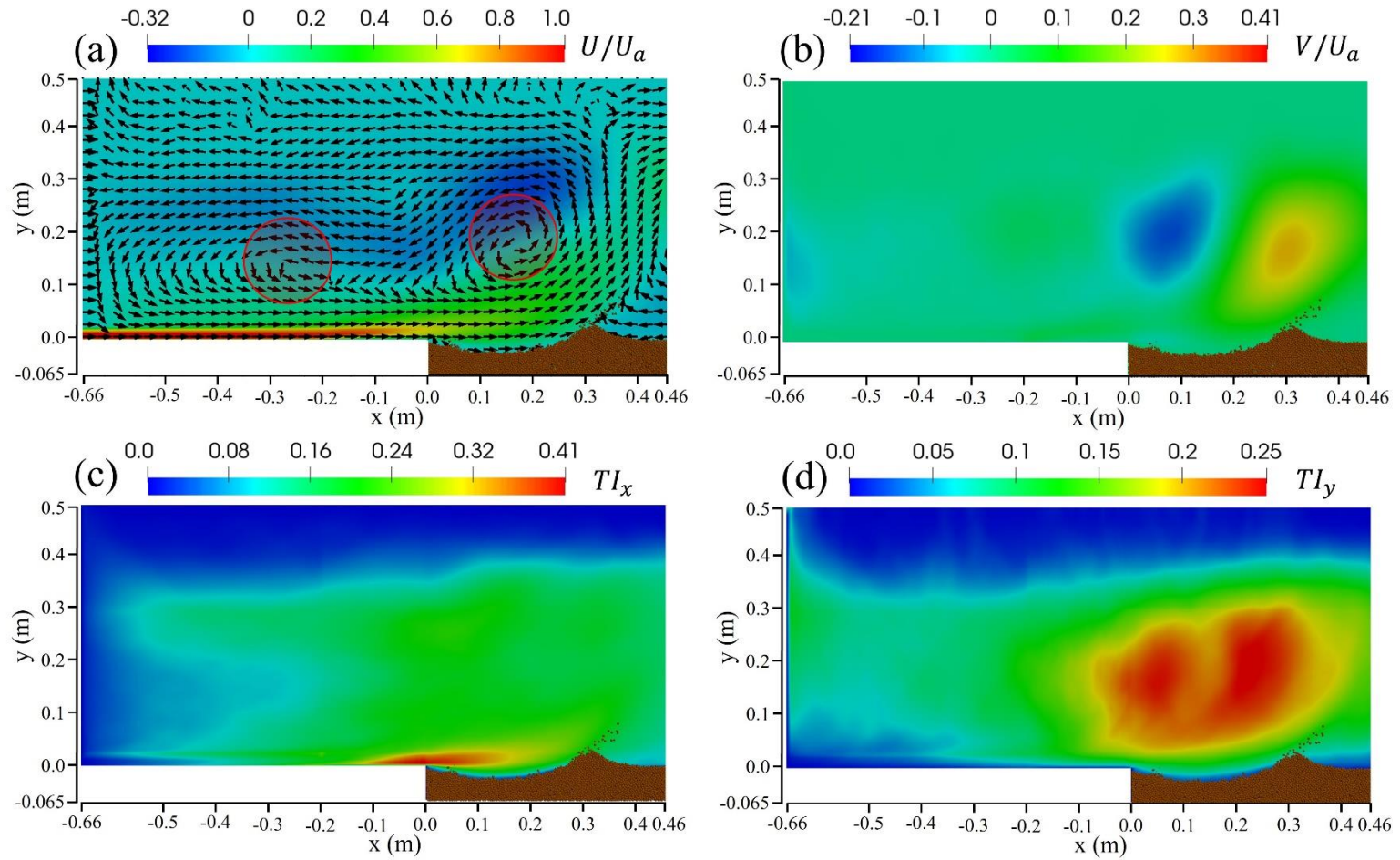


Figure 54. Comparison of mean velocity (a, b) and turbulence intensity (c, d) contours in the central vertical plane ($z/W=0.5$) for CaseRA20Q025.

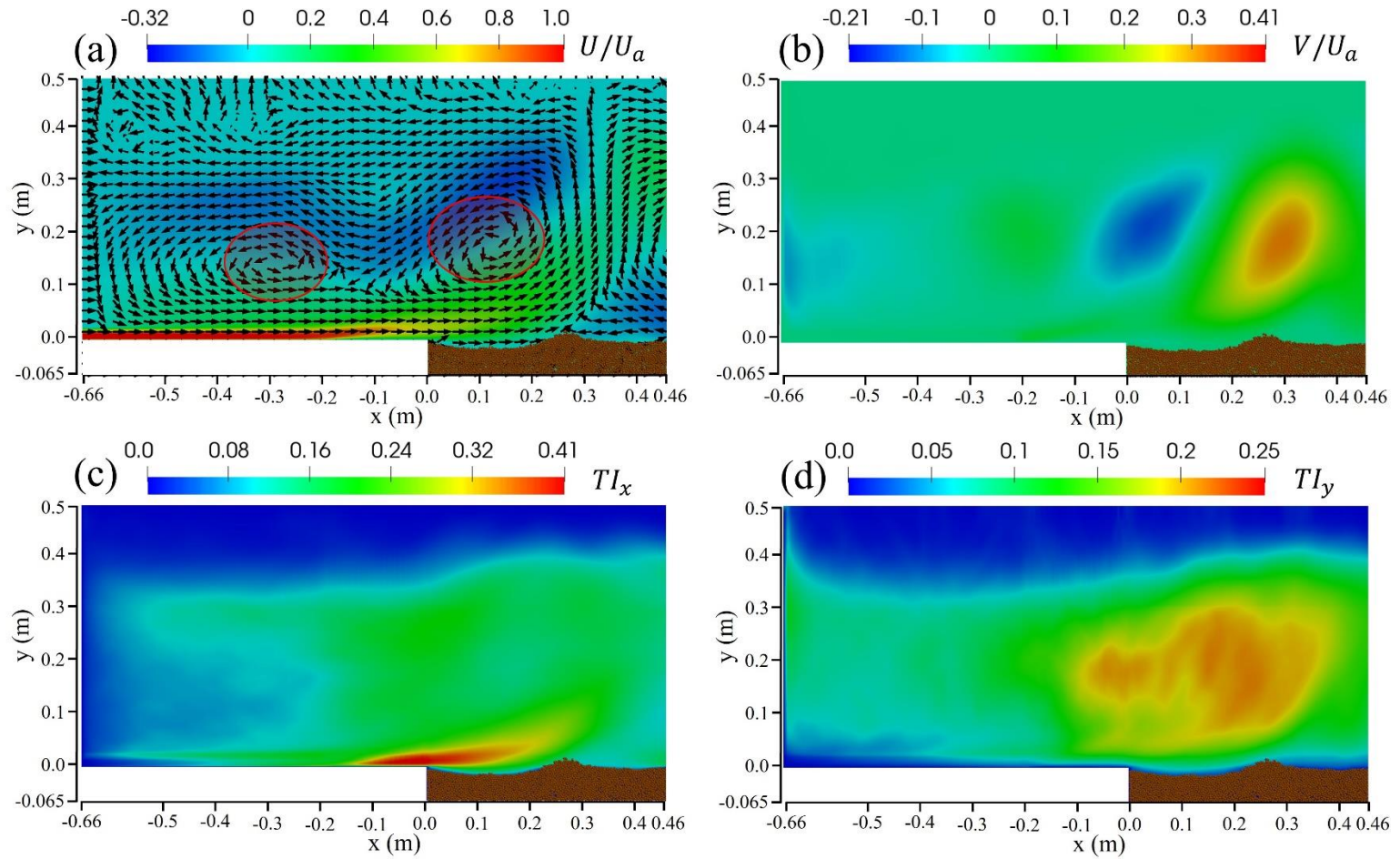


Figure 55. Comparison of mean velocity (a, b) and turbulence intensity (c, d) contours in the central vertical plane ($z/W=0.5$) for CaseRA20Q05.

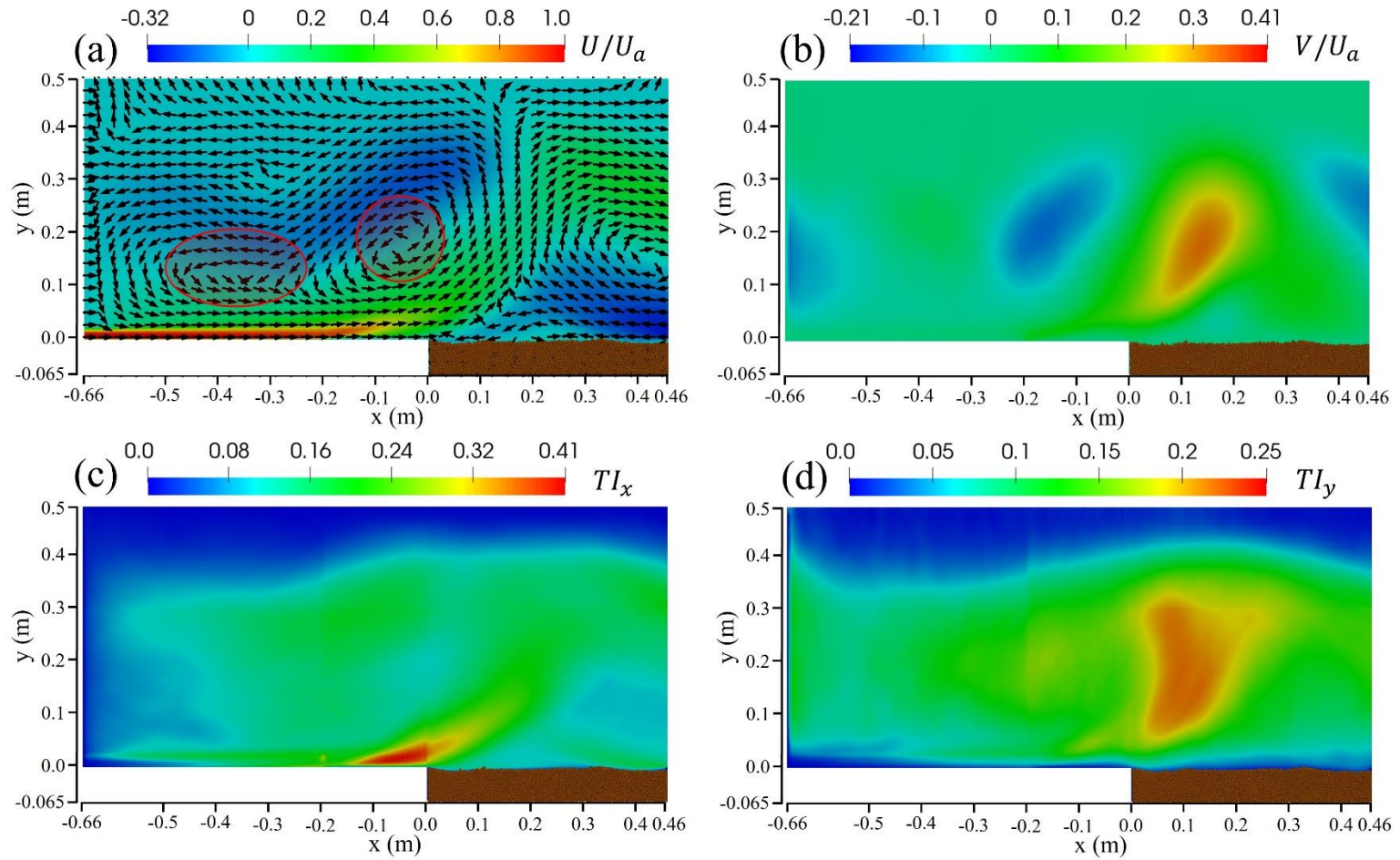


Figure 56. Comparison of mean velocity (a, b) and turbulence intensity (c, d) contours in the central vertical plane ($z/W=0.5$) for CaseRA20Q1.

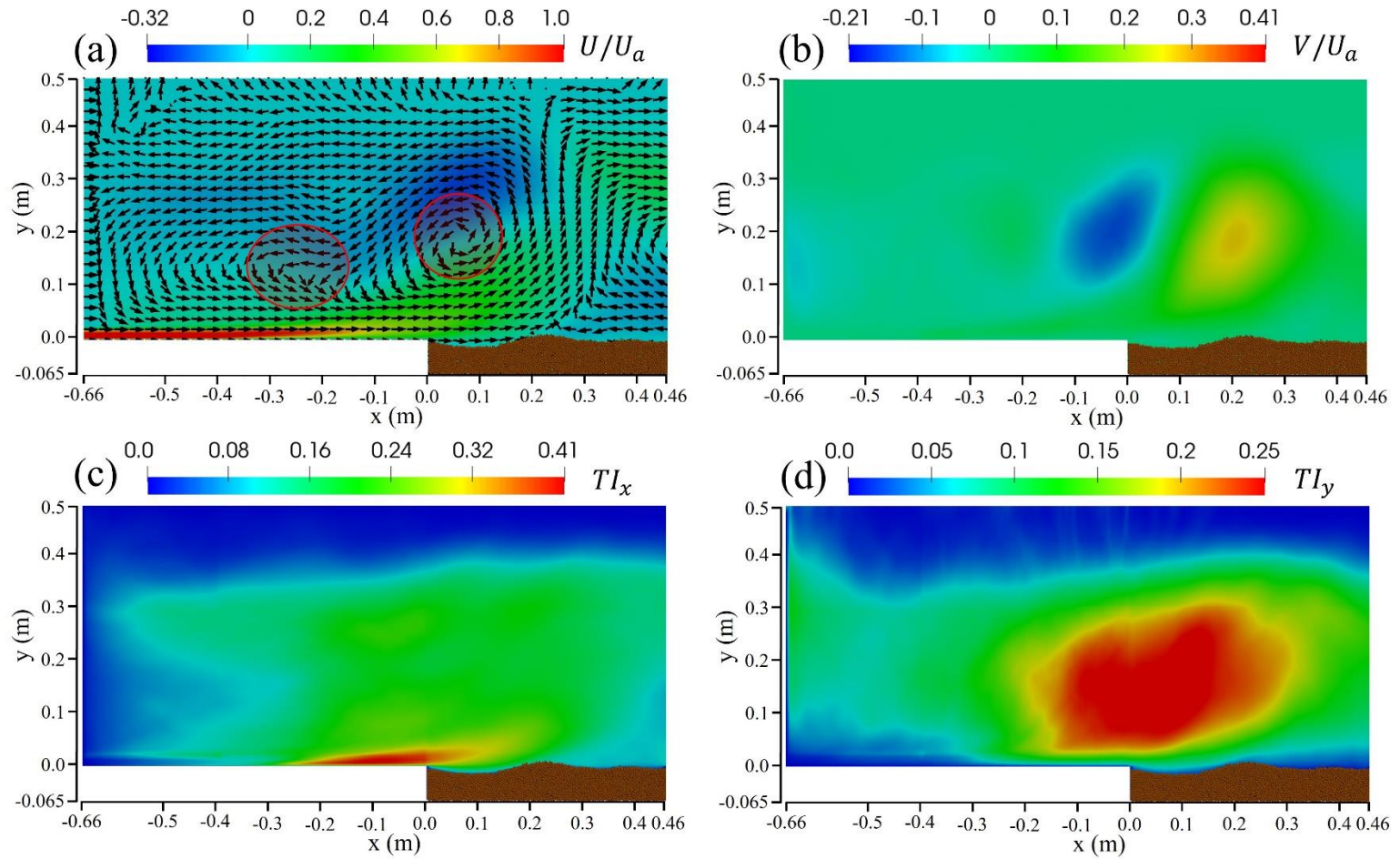


Figure 57. Comparison of mean velocity (a, b) and turbulence intensity (c, d) contours in the central vertical plane ($z/W=0.5$) for CaseRA40Q025.

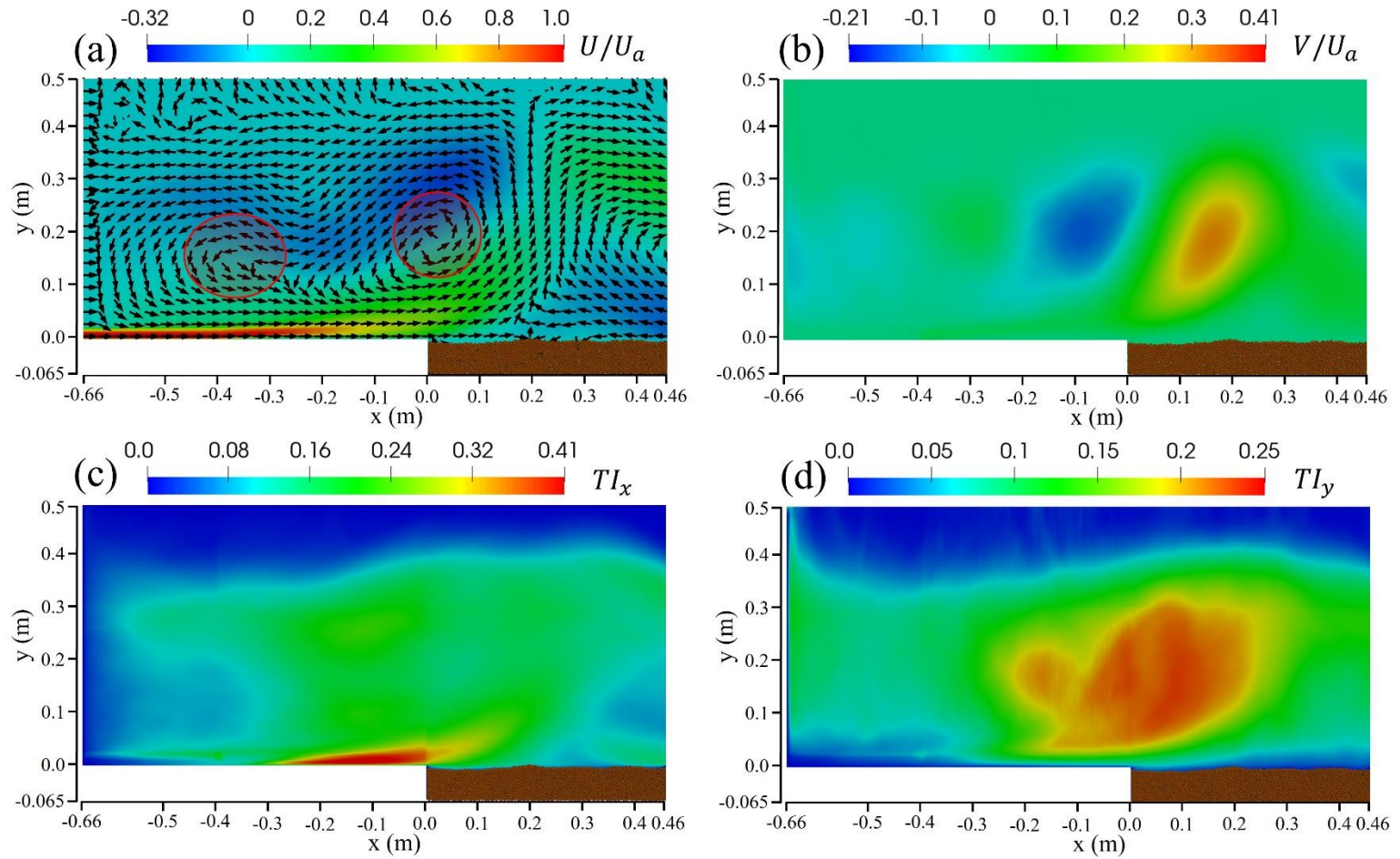


Figure 58. Comparison of mean velocity (a, b) and turbulence intensity (c, d) contours in the central vertical plane ($z/W=0.5$) for CaseRA40Q05.

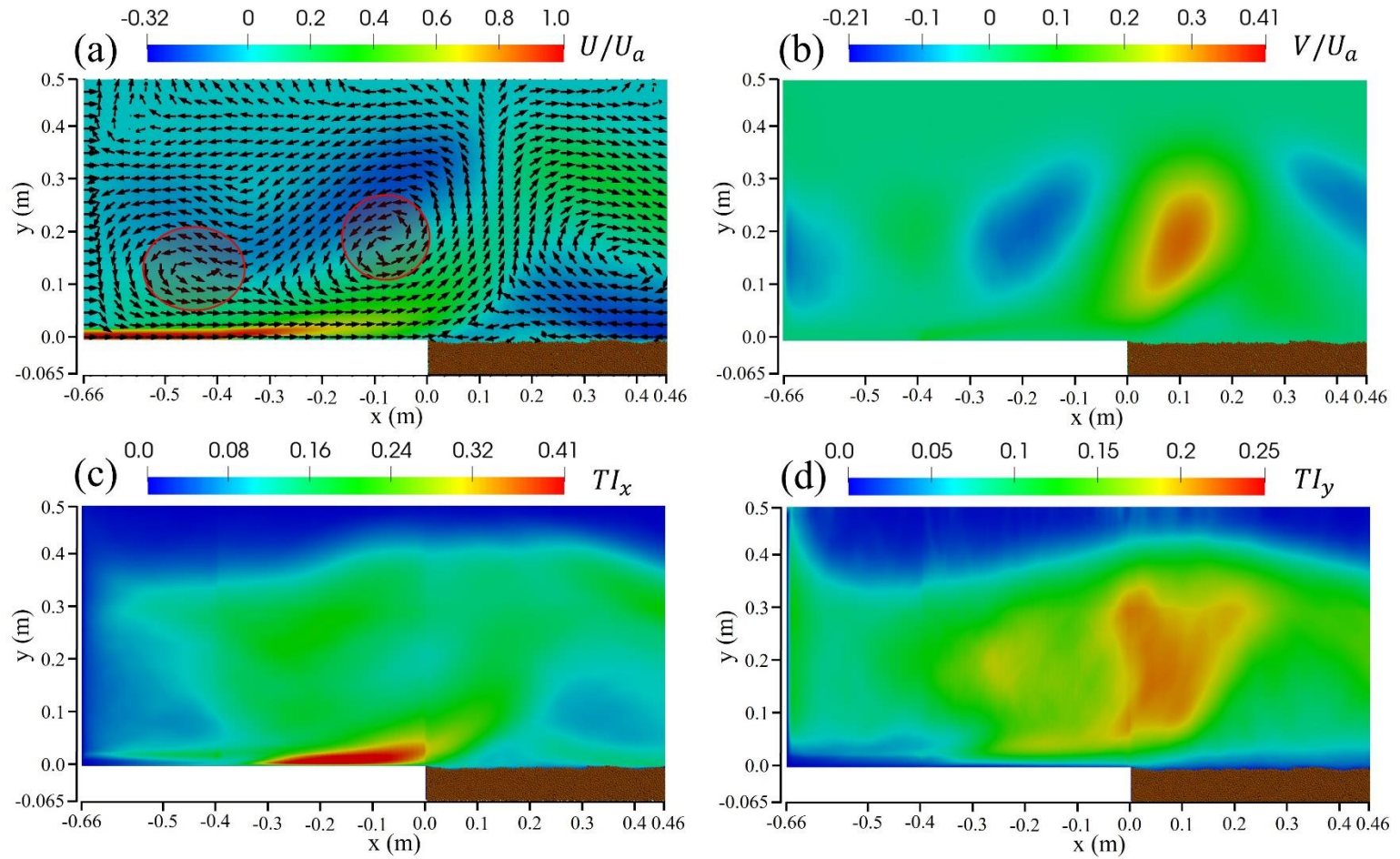


Figure 59. Comparison of mean velocity (a, b) and turbulence intensity (c, d) contours in the central vertical plane ($z/W=0.5$) for CaseRA40Q1.

Figures 60-62 compare the vertical distribution of U , V , TI_x , and TI_y above $x = 0$ for all the simulation cases. For the same air injection length (RA2, RA4, and RA40), it was found that the mean streamwise velocity, U , decreases as the air injection rate increases, and the vertical position of the maximum velocity was shown to be also increased for all the simulation cases. Similarly, for the same air injection flow rate (Q025, Q05, and Q1), U decreases, and the vertical location of the maximum velocity increases as the air injection length increases. This increase is simply due to the vertical directionality of the injected air, and it serves as a barrier to prevent sediment transport. This trend is closely consistent with the findings of Dey et al. (2010), in which they found the effect of injection on reducing streamwise velocity by bending the flow upward. The streamwise mean velocity U in CaseRA2 was found to be significantly higher for all the air injection flow rate compared to CaseRA20 and CaseRA40. However, the maximum and near-wall TI_x were shown to be relatively lower than the other cases. This lower turbulence intensity allows for a similar level of scour reduction as in CaseRA20 despite the relatively higher streamwise mean velocity, as shown in Table 14. V increases as the air injection flow rate increases for the same air injection length, while the vertical turbulence intensity TI_y decreases. All the information of mean velocities and turbulence intensities discussed here is summarized in Tables 15 and 16. The near-wall flow variables presented in Table 16 were numerically obtained at $y = 6$ mm, which is the thickness of the inner layer of the jet without air injection at $x = 0$. The findings above indicate that the decreased near-bed mean streamwise velocity due to the air injection can play a significant role in preventing local scouring. The correlation between the flow structures and maximum scour depth can clearly be seen in Figures 63-65. We can confirm that the decreases in the near-bed mean

streamwise velocity contribute the most to scour reduction, as shown in Figures 63a-65a. The maximum mean velocity and turbulence intensities are also somewhat associated with scour reduction, but their correlation is not as consistent as that of the mean streamwise velocity with the scour reduction.

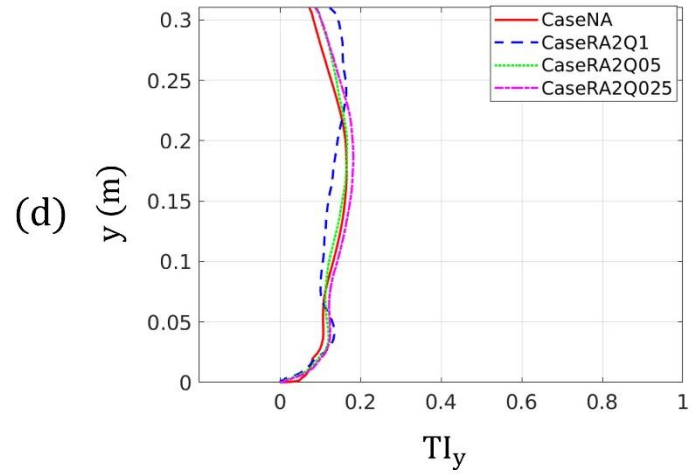
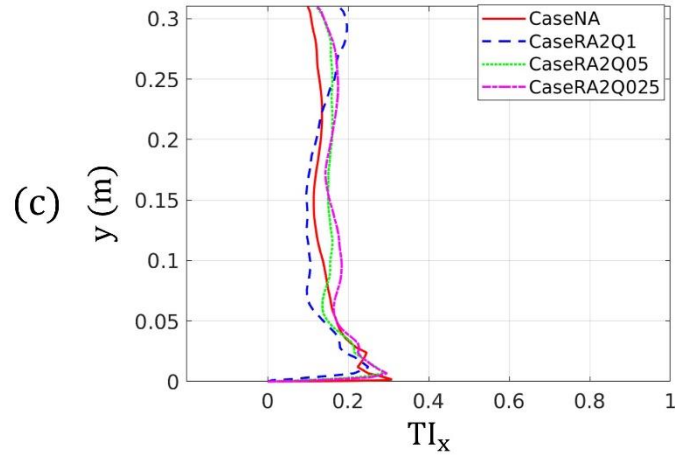
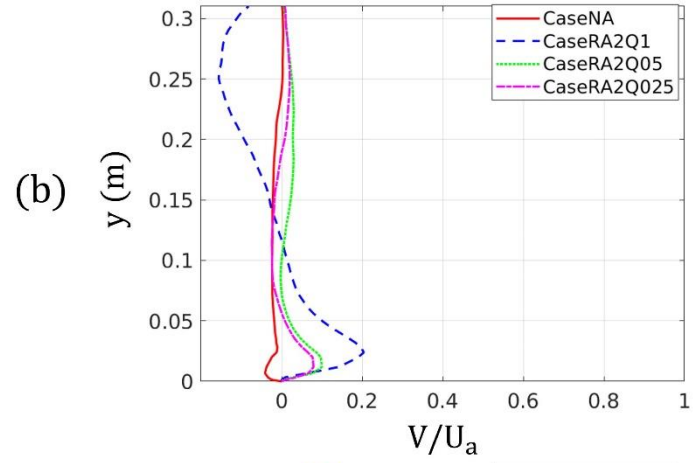
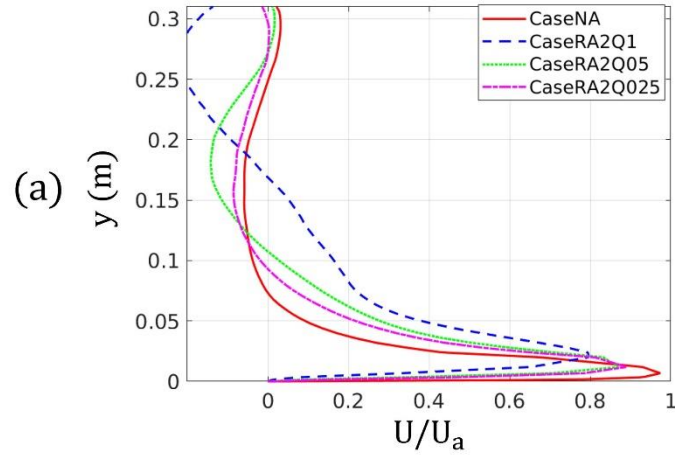


Figure 60. Comparison of mean velocity (a, b) and turbulence intensity (c, d) profiles in the central vertical plane ($z/W=0.5$) between CaseNA and CaseRA2Q025-Q1.

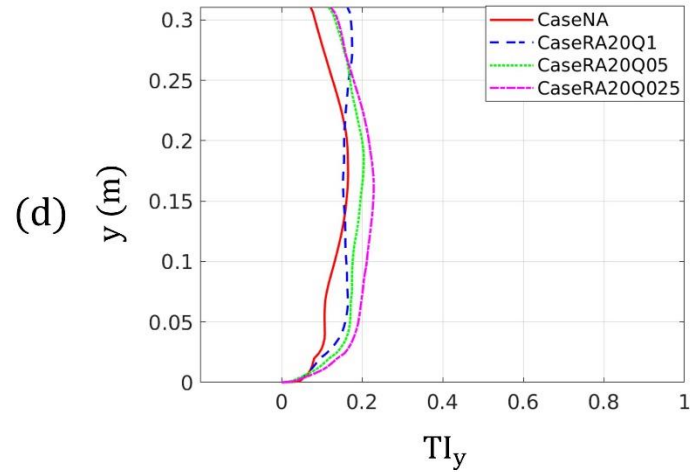
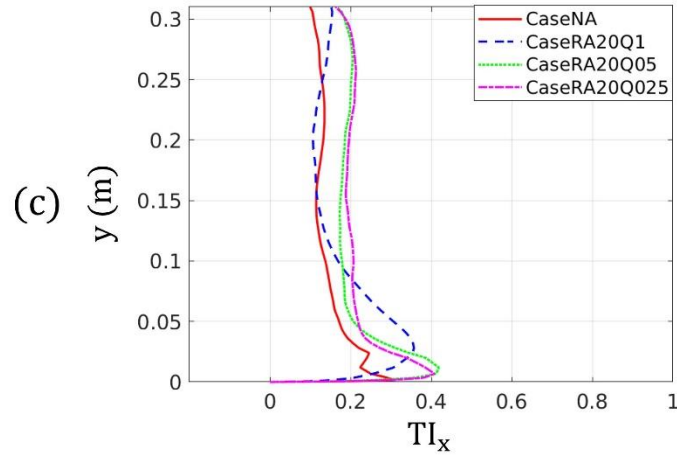
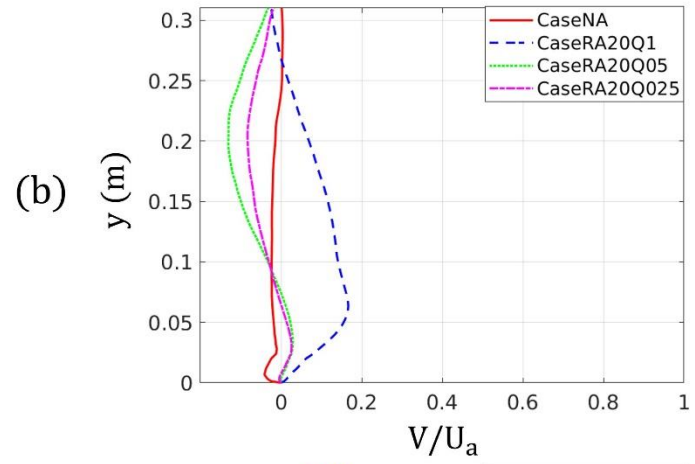
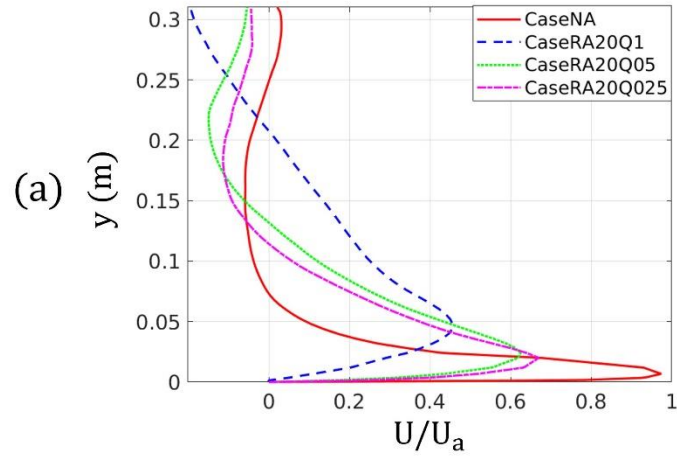


Figure 61. Comparison of mean velocity (a, b) and turbulence intensity (c, d) profiles in the central vertical plane ($z/W=0.5$) between CaseNA and CaseRA20Q025-Q1.

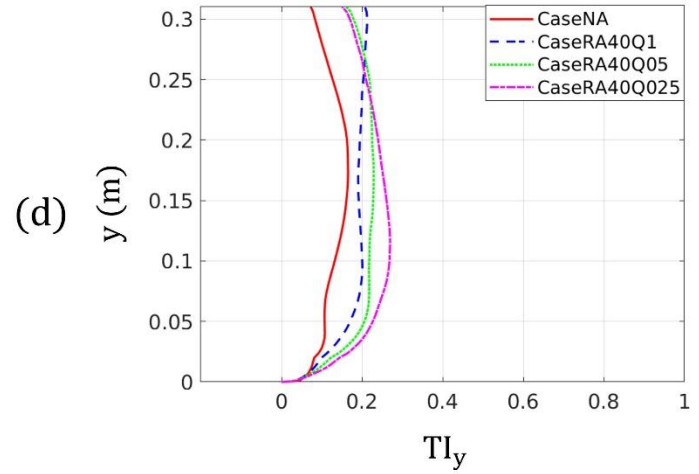
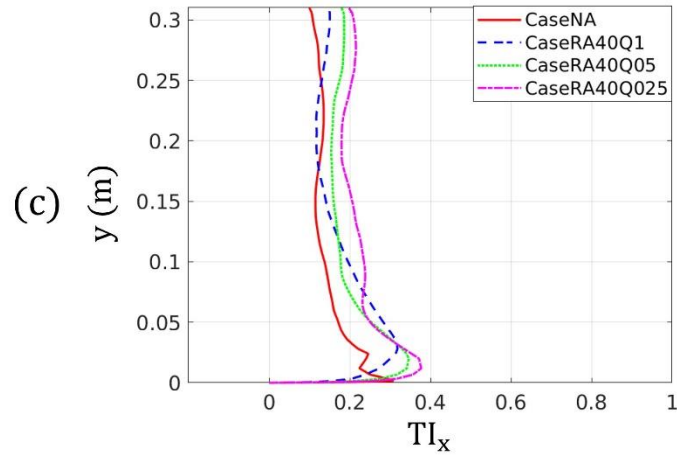
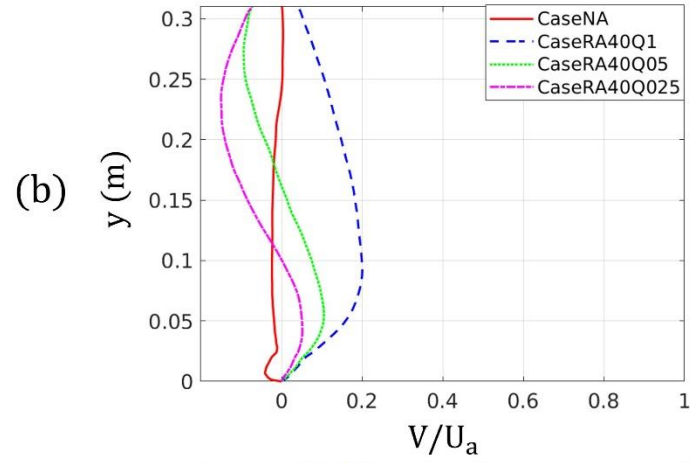
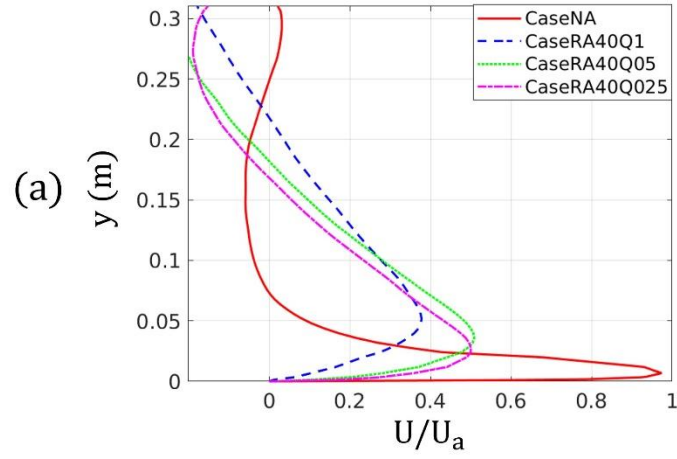


Figure 62. Comparison of mean velocity (a, b) and turbulence intensity (c, d) profiles in the central vertical plane ($z/W=0.5$) between CaseNA and CaseRA40Q025-Q1.

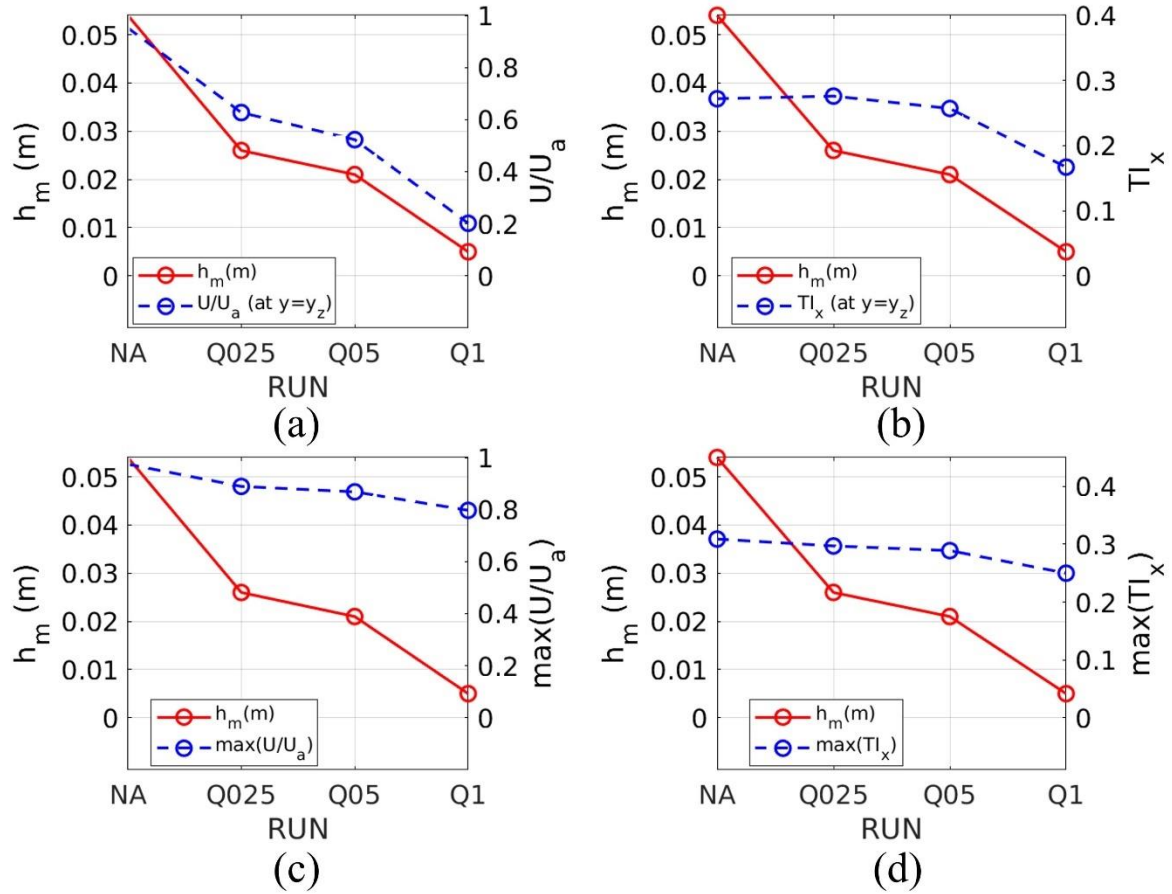


Figure 63. Relation between the maximum scour depth and near-bed mean velocity (a), turbulence intensity (b), maximum mean velocity (c), and turbulence intensity (d) in the central vertical plane at $x = 0$ between CaseNA and CaseRA2.

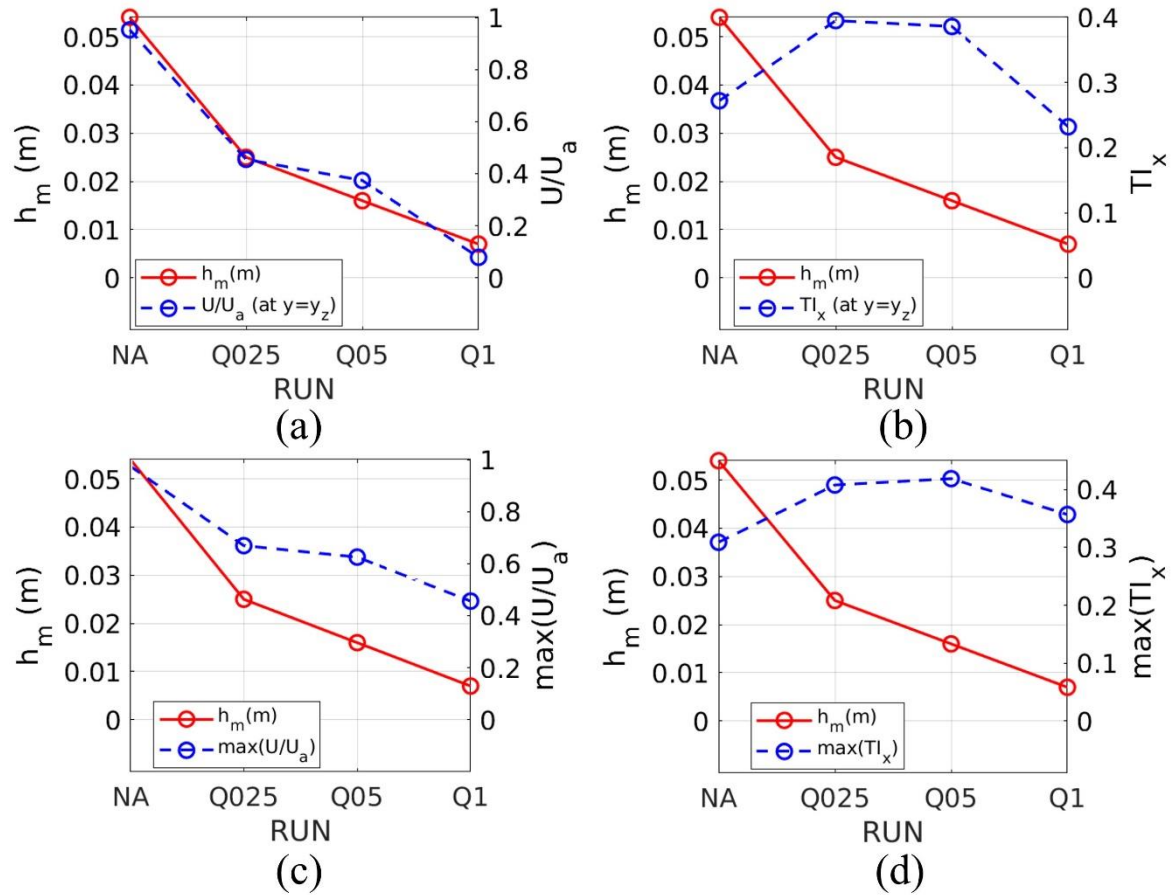


Figure 64. Relation between the maximum scour depth and near-bed mean velocity (a), turbulence intensity (b), maximum mean velocity (c), and turbulence intensity (d) in the central vertical plane at $x = 0$ between CaseNA and CaseRA20.

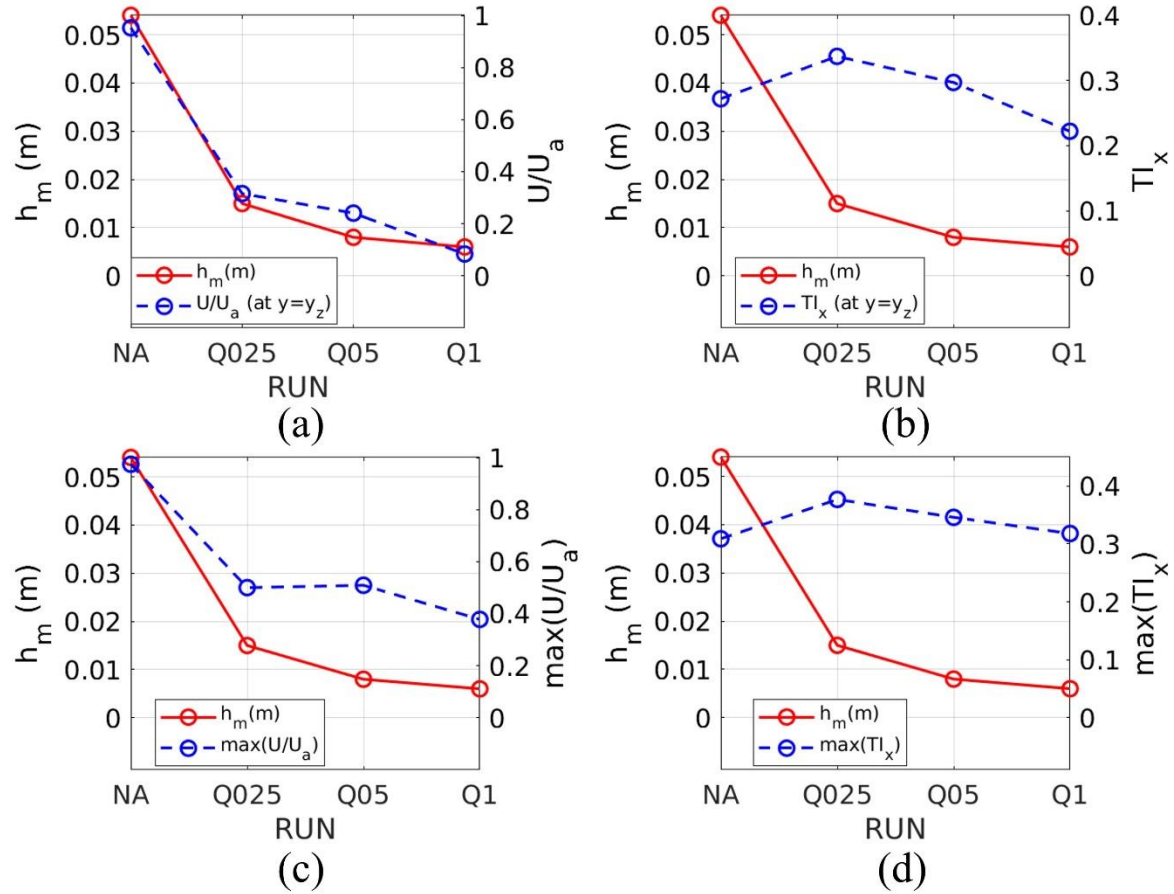


Figure 65. Relation between the maximum scour depth and near-bed mean velocity (a), turbulence intensity (b), maximum mean velocity (c), and turbulence intensity (d) in the central vertical plane at $x = 0$ between CaseNA and CaseRA40.

Figure 66 illustrates the vortex structures visualized by Q-criterion (isosurface: $Q=600$) at a time instant for CaseNA and CaseRA20Q1, serving as representative examples. As illustrated in the figure, air injection leads to a more active generation of vortices. However, when air injection is applied, the roller vortices near the apron exhibit a shorter duration compared to CaseNA. Given that the maximum scour depth h_m was significantly reduced at 87.03 %, it can be conjectured that scour mitigation can be achieved by agitating the jet flow structure by injecting vertical air to prevent forming such vortex structures near the wall.

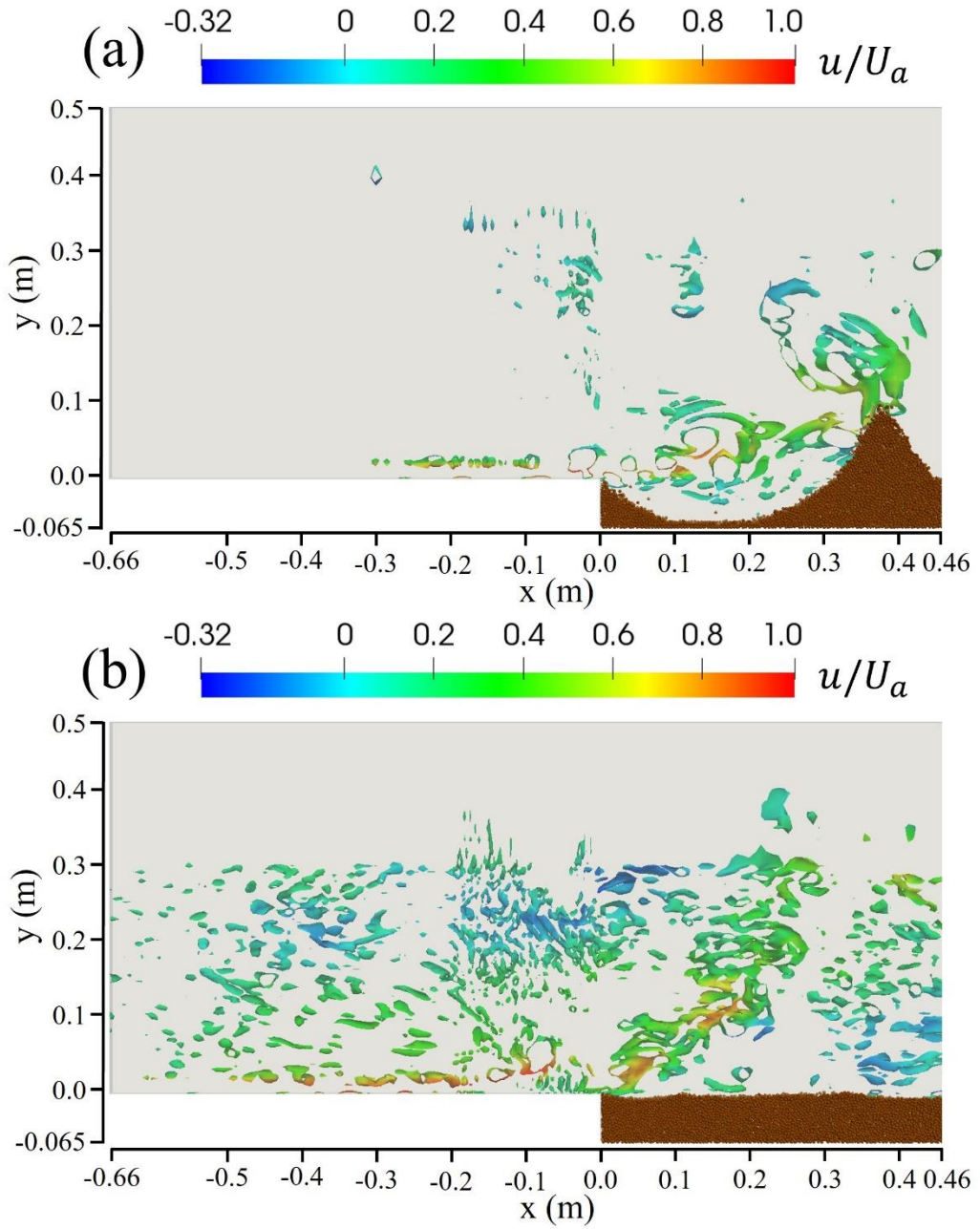


Figure 66. Vortex structures visualized by Q-criterion (isosurface: $Q=300$) at a time instant for CaseNA (a) and CaseRA20Q1 (b).

Table 15. Maximum mean velocity and turbulence intensity in y axis at x = 0 in the central vertical plane.

	Max (U/U_a) Rate of change (%)	Max (V/U_a) Rate of change (%)	Max (TI_x) Rate of change (%)	Max (TI_y) Rate of change (%)
CaseNA	0.974	0.004	0.309	0.165
	-	-	-	-
CaseRA2Q025	0.889	0.079	0.297	0.182
	-8.760	1883.3	-3.982	10.332
CaseRA2Q05	0.868	0.100	0.289	0.167
	-10.886	2398.5	-6.406	0.949
CaseRA2Q1	0.797	0.204	0.250	0.165
	-18.208	4991.7	-19.075	-0.254
CaseRA20Q025	0.669	0.026	0.408	0.229
	-31.326	552.07	32.095	38.868
CaseRA20Q05	0.625	0.029	0.419	0.204
	-35.883	633.53	35.582	23.849
CaseRA20Q1	0.456	0.167	0.357	0.176
	-53.183	4075	15.534	6.667
CaseRA40Q025	0.500	0.052	0.377	0.270
	-48.636	1196.1	22.084	63.458
CaseRA40Q05	0.509	0.105	0.346	0.229
	-47.745	2537.3	12.092	38.811
CaseRA40Q1	0.378	0.201	0.318	0.213
	-61.179	4914.4	2.986	28.943

Table 16. Near-bed mean velocity and turbulence intensity at $x = 0$ and $y = 5$ mm in the central vertical plane.

	U/U_a Rate of change (%)	V/U_a Rate of change (%)	TI_x Rate of change (%)	TI_y Rate of change (%)
CaseNA	0.952	-0.038	0.272	0.060
	-	-	-	-
CaseRA2Q025	0.627	0.052	0.276	0.046
	-34.178	-237.19	1.592	-23.310
CaseRA2Q05	0.523	0.523	0.257	0.040
	-45.067	-1491.9	-5.386	-34.081
CaseRA2Q1	0.202	0.036	0.167	0.032
	-78.739	-196.79	-38.637	-45.985
CaseRA20Q025	0.455	-0.003	0.395	0.066
	-52.164	-91.42	45.175	9.436
CaseRA20Q05	0.374	0.001	0.386	0.053
	-60.765	-103.32	41.824	-11.103
CaseRA20Q1	0.079	0.018	0.232	0.055
	-91.753	-148.97	-14.563	-7.664
CaseRA40Q025	0.316	0.009	0.337	0.068
	-66.790	-123.67	24.055	13.517
CaseRA40Q05	0.241	0.017	0.297	0.062
	-74.653	-144.82	9.164	3.610
CaseRA40Q1	0.084	0.020	0.222	0.058
	-91.223	-152.85	-18.230	-3.085

7.2.3 Quadrant analysis for bedload transport

The quadrant analysis for bedload transport was conducted to investigate flow-sediment interactions near the sediment bed at the initial stage of local scouring near the apron ($x < 0.18$ m) due to the wall jet flow, representatively for CaseNA and CaseRA20Q1. The detail of the analysis is elucidated in Chapter 4.9. The fluctuating velocities u' and v' of water phase, as well as q_x , were measured during the first 10 s during which the bed profile does not significantly change. This ensured that the vertical distance to the measurement point remained relatively constant. Table 17 includes the quadrant analysis results at various measurement points from $x = 0$ to $x = 0.175$ m. Figure 67 illustrates the quadrant analysis by weighting the instantaneous bedload transport rate q_x with the frequency distribution of velocity pair of u' and v' at three representative measurement points, $x = 0.015$ m, 0.075 m, and 0.175 m. The vertical position of the measurement points is located at $y=6$ mm, which corresponds to the inner jet layer thickness y_z in this study.

The quadrant analysis results in CaseNA indicate that the sweep event is the most responsible turbulence event for moving the sediment forward until $x = 0.075$ m, as shown in Figures 67a and 67b. The high ratio of the sweep events near the apron edge is consistent with the high initial scour during the first 10 s, as depicted in Figure 36a. From $x = 0.075$ m, the outward interactions become the most dominant events for moving the sediment until the last measurement point $x = 0.175$ m, as depicted in Figure 67c. The ratio of bedload transport rate occupied by the outward interaction increases along the streamwise direction, as indicated in Table 17. This upward movement of the sediment can be attributed to the gradual formation of the stoss side of the scour hole over time.

In the air injection case CaseRA20Q1, the results of the quadrant analysis reveal that outward interaction is the most influential turbulence events for sediment transport until $x = 0.075$ m, as illustrated in Figures 67d and 67e. The dominance of the outward interaction can be attributed to the effect of the nearby vertical air injection. The area of the q_x -weighted frequency distribution in the figures is determined by the fluctuating velocity of u' and v' , rather than by the sediment flux. Due to the flow agitation caused by the nearby air injection, the areas of the frequency distribution in Figures 67d and 67e was quantified to be similar to those in Figures 67a and 67b. From $x = 0.105$ m to $x = 0.135$ m, where the sediment is farther away from the air-injecting position, the inward interaction was identified as the primary turbulence event responsible for moving the particles, as indicated in Table 17. At the farthest measurement point at $x = 0.175$ m, the burst was found to be the most dominant turbulence event in terms of the sediment movement to upstream. However, as can be seen in Figures 42a and 47, the amount of sediment movement is not significant. Upon summarizing the results from the quadrant analysis of bedload transport, it's evident that sweep is the most influential type of turbulence for moving sediment forward, thereby leading to local scour. By injecting air, the sediment near the apron moves along the outward and inward interactions, although only a small amount of sediment movement is involved in this process.

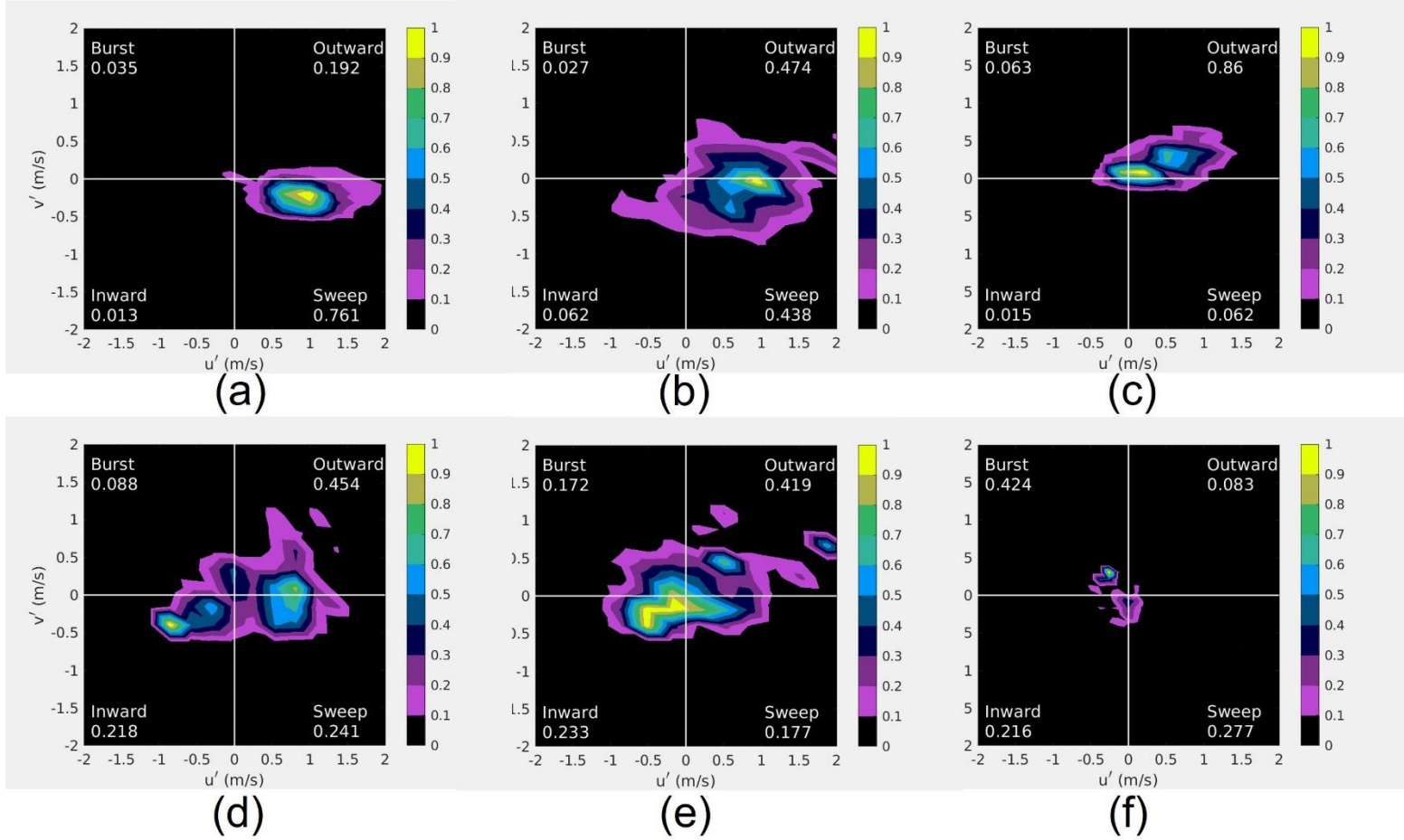


Figure 67. Joint frequency distributions of u' and v' weighted by q_x measured at $x = 0.015$ m (a, d), 0.075 m (b, e), and 0.175 m (c, f) for CaseNA (a, b, c) and CaseRA20Q1 (d, e, f).

Table 17. Ratio (in percentage) of bedload transport rate during each turbulence event with and without air injection in wall jet flow.

Measurement point	Case	Burst	Sweep	Outward Interaction	Inward interaction
x = 0.015 m	CaseNA	0.035	0.761	0.192	0.013
	CaseR20Q1	0.088	0.241	0.454	0.218
x = 0.045 m	CaseNA	0.011	0.688	0.274	0.027
	CaseR20Q1	0.119	0.183	0.462	0.236
x = 0.075 m	CaseNA	0.027	0.438	0.474	0.062
	CaseR20Q1	0.172	0.177	0.419	0.233
x = 0.105 m	CaseNA	0.046	0.272	0.629	0.054
	CaseR20Q1	0.234	0.164	0.274	0.328
x = 0.135 m	CaseNA	0.028	0.152	0.782	0.037
	CaseR20Q1	0.213	0.209	0.176	0.402
x = 0.175 m	CaseNA	0.063	0.062	0.86	0.015
	CaseR20Q1	0.424	0.277	0.083	0.216

CHAPTER 8. CONCLUSIONS

This thesis first investigates the flow and turbulence structures downstream of various inclined BFSs, as well as their interactions with sediment behaviors under surface jet flow. The effect of various inclined BFSs on near-bed flow characteristics, sediment behaviors, and their interaction in the surface jet flow were numerically investigated. A combined numerical model of LES and DEM, based on the open sources OpenFOAM framework, was used to reproduce the separation flow and sediment behaviors. The numerical model was extensively validated against various experimental data with different angles of inclined BFSs. The good agreement between the numerical and experimental results confirmed that the numerical model can be used as a reliable tool to study the turbulent flow structures and bedload motions around the separation zone. The near-bed mean velocity, turbulence intensity, and bedload transport rate downstream of the BFSs were numerically quantified. The coherent vortices behind the BFSs were visualized using the Q-criterion. The quadrant analysis for flow structure and bedload transport rate was applied to examine the near-bed flow-sediment interactions. From the simulation results, the following conclusions and remarks can be summarized:

- For the small BFS angle (10°), a flow separation did not form up. Although the mean streamwise velocity near bed is largest in comparison to that in the other larger BFS angles (20° , 30° , and 90°), the near-bed turbulence intensity was smaller to induce a sediment movement. The coherent vortices visualized by the

Q-criterion were barely generated with relatively small vorticity. The quadrant analysis for flow structure and bedload transport revealed that the dominant turbulence events to move the sediments were mainly burst and sweep events.

- When the BFS angle increased to 20° , a small separation zone was formed, and the reattachment point was located right downstream of the step. It showed that the near-bed mean velocity decreased slightly, but the near-bed turbulence intensity was considerably increased in comparison with that in BFS angle of 10° . The large-scale coherent vortices began to actively generate along the SSL. Therefore, a reasonable conjecture can be made that the significant increment of turbulence intensity resulted from the splat effect is caused by the collision of the hairpin vortices with the bed. A peak of the mean bedload transport rate was found at a short distance downstream of the reattachment point. As determined by the quadrant analysis, the dominant turbulence events downstream of the BFS were mainly burst and sweep, which are similar to the results obtained from the step angle of 10° . However, the significant turbulence event at the reattachment point was prominently sweep event, which is indicating that the colliding eddies at the reattachment point contribute to drag the majority of sediment in the flow direction.
- As the BFS angle further increases to 30° and 90° , the separation zone was enlarged, consequently the reattachment length is extended to the downstream; and the mean backflow velocity within the separation zone was increased. An overall near-bed mean velocity and turbulence intensity were not notably altered.

However, the distance over which the high near-bed turbulence persists downstream was found to increase as the step angle increased. The near-bed mean velocity became zero at the reattachment point, and then the flow was gradually recovered further downstream. The maximum turbulence intensity was measured at the vicinity of the reattachment point. The large-scale vortex structures were formed more actively and lasted longer at these higher BFS angles. The negative and positive peaks of the mean bedload transport rate were respectively observed at upstream and downstream of the reattachment point. According to the quadrant analysis for bedload transport, the sweep event was the most dominant turbulence event to drag the majority of the sediment toward downstream at the reattachment point. While the burst event located just right upstream of the reattachment point was the most significant turbulence event to eject most sediment backward.

Overall, the numerical results revealed the significant effect of BFS angles on the near-bed turbulent flow structures, sediment behaviors, and their interactions. The flow separation is not observed at a small BFS angle (10° in this study), consequently leading to very small turbulence intensity and sediment movement behind the step. The flow begins to be separated on the step, and its reattachment point is extended as the BFS angle increases (20°), wherein the near-bed turbulence intensities reach their maximum. The increased turbulent diffusion in the separation zone is attributed to the large-scale hairpin vortex structures that are organized along the SSL. The stretching process of the hairpin vortices provides significant instantaneous impinging force on the bed materials to be moved away from the bed. The coherent vortices are extended further downstream as the BFS angle is increased, while the maximum turbulence intensities are unnoticeable

changed. Accordingly, the distance needed to stabilize the sediment motions is extended to downstream along with the increased BFS angles. Conforming to the opposite directions of near-bed mean velocity, two peaks of time-averaged bedload flux are observed. The location of these peaks also moves toward downstream as the BFS angle increases. Burst and sweep motions were found to play important roles in sediment movements at short distances upstream and downstream of the reattachment point, respectively; the former moves the particles backward (toward upstream), while the latter transports the particles forward (toward downstream).

Furthermore, numerical investigations were performed to analyze flow structures and sediment behaviors induced by horizontal wall jet flow behind a sluice gate, both with and without wide-area air injection on the apron. The two-phase (water-sediment) LES-DEM coupling was expanded to incorporate air phase by introducing VOF concept to implement free surface and air injection. The altered bed profile for 60 s without air injection, simulated by the LES-DEM model, exhibited good agreement with laboratory experiment results. The mean velocity, turbulence intensity, and bedload transport rate downstream of the apron were numerically quantified, and the vortex structures over the scour hole were visualized using the Q-criterion. Based on the simulation results, the following conclusions and observations can be summarized:

- The air phase was successfully integrated into the existing two-phase (water-sediment) LES-DEM coupling model, introducing VOF concept to the solver. The good agreement between the experimental and numerical results for the eroded

bed profile by the wall jet confirmed that the expanded LES-DEM model can serve as a reliable tool for simulating local scour due to submerged wall jets.

- Bedload transport rate and scour dimensions with and without wide-area air injection upon the apron was investigated. When air was injected, the bedload transport rate in the sediment zone significantly decreased during the entire simulation time, resulting in minimal changes to the bed profile. By the end of the simulation, the maximum scour depth was found to be decreased by 51.85 % to 90.74 %, depending on the air injection flow rate and injection length. In summary, it is shown that an increase in both the air injection flow rate and the injection length leads to a significant mitigation of scour.
- As the air injection length increases while maintaining the same volumetric flow rate, the airflow velocity from each air slot decreases. Accordingly, the momentum of the injected air decreases. As the momentum of the airflow decreases, the maximum scour depth also decreases. This implies that not only the volumetric flow rate but also the momentum should be considered an important factor when studying the effects of air injection on scour reduction.
- To analyze the cause of the decrease in sediment transport due to air injection, the flow and turbulence structures were examined for cases with and without air injection. The near-bed mean streamwise velocity at the end of apron decreased significantly by 91.75 %, depending on the air injection flow rate and injection length. In contrast, the near-wall vertical velocity substantially increased along with longer air injection length. In contrast, the near-wall vertical velocity

substantially increased with air injection. The vertical turbulence intensity barely changed by air injection. Based on the simulation results, the reduced near-bed streamwise velocity mainly contributes to the scour mitigation behind the apron.

- Quadrant analysis for bedload transport reveals that sweep is the most responsible turbulence event for driving forward movement of sediment near the apron, thereby inducing local scouring. Upon air injections, the most dominant turbulence event to move sediment near the apron becomes outward interactions with large flow fluctuations, but small sediment transport rate.

In summary of the simulation results, it is observed that the decrease in near-wall streamwise velocity played a major role in mitigating the scouring process behind an apron. The significant reduction of the streamwise velocity due to air injection substantially aided in mitigating both the bedload transport rate and the maximum scour depth throughout the evolution of the scour hole. The injected air is thought to serve as a barrier that contribute to reducing sediment transport by blocking near-bed horizontal flow. It was found that an increase in both the air injection flow rate and the injection length results in substantial mitigation of scour.

The finding that the near-bed mean streamwise velocity is the most influential factor in scour process of wall jet flow contradicts the result that the turbulence intensity is the predominant factor influencing sediment flux in surface jet flow under flow separation. This leads to a reasonable conclusion that when analyzing the interaction between flow structures and sediment behaviors, different key flow variables must be considered, depending on the specific flow condition and regime.

For future research, it is worth considering the investigation of flow-sediment interactions in different flow regimes using the established LES-DEM model in this study and evaluation of various countermeasures against sediment transport that was not covered in the current research scope in this thesis. Additionally, it is important to note that this study focused solely on evaluating the effects of scour reduction on sediment particles of a single size. This limitation highlights the need for future research to examine how varying sediment particle sizes impact the rate of scour reduction. Moreover, the present study assumed a uniform particle size with a relatively low standard deviation. To better reflect real-world river conditions, it is recommended that numerical simulations be expanded to include a wider distribution of particle sizes. By doing so, a more comprehensive understanding of scour reduction can be attained, considering the diverse range of sediment particle sizes typically encountered in rivers. In this regard, obtaining quantitative data on flow conditions, sediment distribution, and the extent of scour near real hydraulic structures would greatly enhance the validity of the numerical model proposed in this study and broaden the research's scope.

Furthermore, for the practical application of this research, it is crucial to investigate the flow conditions that trigger active sediment transport at sites where sediment movement becomes problematic. This entails examining the location, size, air injection flow rate, and distribution of air injection areas. The study on determining the optimal spacing between air slots is also important, as it can affect the merging of air flows with different air injection velocities. In addition, environmental issues related to change of water temperature and variation in the amount of oxygen should also be discussed before implementing the air injection.

Even though air injection can create a strong buoyancy force and mitigate scouring, as verified in this study, it is still worth investigating the effects of water on scour mitigation. For instance, Tamoradi and Ahadiyan (2022) identified scour reduction through water injection at a river bend. This reduction was attributed to the strong momentum and turbulence generated by the water injection. Their findings confirmed that scouring was diminished through the water injection method. Based on these findings, exploring water injection or a mixed-phase water-air injection in future studies could present significant opportunities to further our understanding and capabilities in scour mitigation.

Moreover, considering that this study reveals that the principal mechanism for scour mitigation is the prevention of downward flow, also known as a sweep event, by diverting the near-bed mean flow upward through air injection, it is worth exploring alternative erosion reduction strategies, such as the incorporation of an inclined structure like a ramp at the beginning of the sediment zone. However, the angles and lengths of this structure should be optimized to reduce flow separation to avoid extensive turbulent diffusion that could accelerate scouring behind the structure.

REFERENCES

ADAMS, E. W. (1984). Experiments on the structure of turbulent reattaching flow (Doctoral dissertation, Stanford University).

Adams, E. W., & Johnston, J. P. (1988). Effects of the separating shear layer on the reattachment flow structure part 2: Reattachment length and wall shear stress. *Experiments in Fluids*, 6(7), 493-499.

Alam, M., & Sandham, N. D. (2000). Direct numerical simulation of 'short' laminar separation bubbles with turbulent reattachment. *Journal of Fluid Mechanics*, 410, 1-28.

Ali, K. H. M., & Lim, S. Y. (1986). Local scour caused by submerged wall jets. *Proceedings of the Institution of Civil Engineers*, 81(4), 607-645.

Amsler, M. L., Prendes, H. H., Montagnini, M. D., Szupiany, R., & Garcia, M. H. (2003). Prediction of dune height in sand-bed rivers: The case of the Paraná River, Argentina. In *Proceedings of the 3rd IAHR Symposium on River, Coastal and Estuarine Morphodynamics* (pp. 1104-1113). Madrid: IAHR Secret..

Armaly, B. F., Durst, F., Pereira, J. C. F., & Schönung, B. (1983). Experimental and theoretical investigation of backward-facing step flow. *Journal of fluid Mechanics*, 127, 473-496.

ASCE Task Committee on Flow and Transport over Dunes. (2002). Flow and transport over dunes. *Journal of Hydraulic Engineering*, 128(8), 726-728.

Babaeyan-Koopaei, K.; Ervine, D.A.; Carling, P.A.; Cao, Z. Velocity and turbulence measurements for two overbank flow events in River Severn. *J. Hydraul. Eng. ASCE* 2002, 128, 891–900.

Back, L. H., & Roschke, E. J. (1972). Shear-layer flow regimes and wave instabilities and reattachment lengths downstream of an abrupt circular channel expansion.

Balachandar, R., & Reddy, H. P. (2011). Bed forms and flow mechanisms associated with dunes. *Sediment Transport-Flow and Morphological Processes*, 1, 35-69.

Balachandar, R., Hyun, B. S., & Patel, V. C. (2007). Effect of depth on flow over a fixed dune. *Canadian Journal of Civil Engineering*, 34(12), 1587-1599.

Balachandar, R., & Patel, V. C. (2008). Flow over a fixed rough dune. *Canadian Journal of Civil Engineering*, 35(5), 511-520.

Ban, C., & Choi, S. U. (2022). Characteristics of instantaneous flow structures of the surface jet over a submerged weir. *Journal of Hydraulic Research*, 60(3), 476-486.

Ben Meftah, M., & Mossa, M. (2006). Scour holes downstream of bed sills in low-gradient channels. *Journal of Hydraulic Research*, 44(4), 497-509.

Ben Meftah, M., & Mossa, M. (2020). New approach to predicting local scour downstream of grade-control structure. *Journal of Hydraulic Engineering*, 146(2), 04019058.

Bennett, S. J., & Best, J. L. (1995). Mean flow and turbulence structure over fixed, two-dimensional dunes: implications for sediment transport and bedform stability. *Sedimentology*, 42(3), 491-513.

Best, J. L. (1996). The fluid dynamics of small-scale alluvial bedforms. *Advances in fluvial dynamics and stratigraphy*, 67-125.

Best, J. L., Kirkbride, A. D., & Peakall, J. (2001). Mean flow and turbulence structure of sediment-laden gravity currents: new insights

Best, J., & Kostaschuk, R. (2002). An experimental study of turbulent flow over a low-angle dune. *Journal of Geophysical Research: Oceans*, 107(C9), 18-1. using ultrasonic Doppler velocity profiling. *Particulate gravity currents*, 157-172.

Biswas, G., Breuer, M., & Durst, F. (2004). Backward-facing step flows for various expansion ratios at low and moderate Reynolds numbers. *J. Fluids Eng.*, 126(3), 362-374.

Blanckaert, K. D. V. H., & De Vriend, H. J. (2004). Secondary flow in sharp open-channel bends. *Journal of Fluid Mechanics*, 498, 353-380.

Bormann, N. E., & Julien, P. Y. (1991). Scour downstream of grade-control structures. *Journal of hydraulic engineering*, 117(5), 579-594.

Boussinesq, J. (1877). *Essai sur la théorie des eaux courantes*. Impr. nationale.

Carling, P. A., Golz, E., Orr, H. G., & Radecki-Pawlik, A. (2000). The morphodynamics of fluvial sand dunes in the River Rhine, near Mainz, Germany. I. Sedimentology and morphology. *Sedimentology*, 47(1), 227-252.

Carling, P. A., Williams, J. J., Golz, E., & Kelsey, A. D. (2000). The morphodynamics of fluvial sand dunes in the River Rhine, near Mainz, Germany. II. Hydrodynamics and sediment transport. *Sedimentology*, 47(1), 253.

Champagne, T. M., Barkdoll, B. D., Gonzalez-Castro, J. A., & Deaton, L. (2016a). Scour reduction by air injection: Flow patterns and turbulence. *Journal of Hydraulic Engineering*, 142(3), 06015023.

Champagne, T. M., Barlock, R. R., Ghimire, S. R., Barkdoll, B. D., Gonzalez-Castro, J. A., & Deaton, L. (2016b). Scour reduction by air injection downstream of Stilling Basins: Optimal configuration determination by experimentation. *Journal of Irrigation and Drainage Engineering*, 142(12), 04016067.

Chang, W. Y., Constantinescu, G., Tsai, W. F., & Lien, H. C. (2011). Coherent structure dynamics and sediment erosion mechanisms around an in-stream rectangular cylinder at low and moderate angles of attack. *Water Resources Research*, 47(12).

Chapman, D. R., Kuehn, D. M., & Larson, H. K. (1958). Investigation of separated flows in supersonic and subsonic streams with emphasis on the effect of transition.

Chatterjee, S. S., & Ghosh, S. N. (1980). Submerged horizontal jet over erodible bed. *Journal of the Hydraulics Division*, 106(11), 1765-1782.

Chatterjee, S. S., Ghosh, S. N., & Chatterjee, M. (1994). Local scour due to submerged horizontal jet. *Journal of Hydraulic Engineering*, 120(8), 973-992.

Chen, L., Asai, K., Nonomura, T., Xi, G., & Liu, T. (2018). A review of Backward-Facing Step (BFS) flow mechanisms, heat transfer and control. *Thermal Science and Engineering Progress*, 6, 194-216.

Chen, Y. T., Nie, J. H., Hsieh, H. T., & Sun, L. J. (2006). Three-dimensional convection flow adjacent to inclined backward-facing step. *International Journal of Heat and Mass Transfer*, 49(25-26), 4795-4803.

Chiew, Y. M. (1995). Mechanics of riprap failure at bridge piers. *Journal of hydraulic engineering*, 121(9), 635-643.

Choi, H. H., & Nguyen, J. (2016). Numerical investigation of backward facing step flow over various step angles. *Procedia Engineering*, 154, 420-425.

Coleman, S. E., Nikora, V. I., McLean, S. R., Clunie, T. M., Schlicke, T., & Melville, B. W. (2006). Equilibrium hydrodynamics concept for developing dunes. *Physics of Fluids*, 18(10), 105104.

Cox, G. N. (1928). The submerged weir as a measuring device: A method for making accurate stream flow measurements that involve small loss of head (No. 67). University of Wisconsin--Madison.

Das G.K. (2016) Sediment Grain Size. In: Kennish M.J. (eds) *Encyclopedia of Estuaries*. *Encyclopedia of Earth Sciences Series*. Springer, Dordrecht. https://doi.org/10.1007/978-94-017-8801-4_148

Dey, S., & Barbhuiya, A. K. (2004, June). Clear water scour at abutments. In *Proceedings of the Institution of Civil Engineers-Water Management* (Vol. 157, No. 2, pp. 77-97). Thomas Telford Ltd.

Dey, S., Nath, T. K., & Bose, S. K. (2010). Submerged wall jets subjected to injection and suction from the wall. *Journal of fluid mechanics*, 653, 57-97.

Dey, S., & Sarkar, A. (2006). Scour downstream of an apron due to submerged horizontal jets. *Journal of hydraulic engineering*, 132(3), 246-257.

Dey, S., & Sarkar, A. (2008). Characteristics of submerged jets in evolving scour hole downstream of an apron. *Journal of Engineering Mechanics*, 134(11), 927-936.

Dey, S., & Westrich, B. (2003). Hydraulics of submerged jet subject to change in cohesive bed geometry. *Journal of Hydraulic Engineering*, 129(1), 44-53.

Di Felice, R. (1994). The voidage function for fluid-particle interaction systems. *International journal of multiphase flow*, 20(1), 153-159.

Durst, F., & Tropea, C. (1981, September). Turbulent, backward-facing step flows in two-dimensional ducts and channels. In *Proc. 3rd Int. Symp. on Turbulent Shear Flows* (pp. 18-1).

Durst, F., & Tropea, C. (1983). Flows over two-dimensional backward—facing steps. In *Structure of Complex Turbulent Shear Flow* (pp. 41-52). Springer, Berlin, Heidelberg.

Eaton, J. K. (1980). Turbulent flow reattachment: an experimental study of the flow and structure behind a backward-facing step. Stanford University.

Eaton, J. K., & Johnston, J. P. (1981). A review of research on subsonic turbulent flow reattachment. *AIAA journal*, 19(9), 1093-1100.

Einstein, H. A. (1950). The bed-load function for sediment transportation in open channel flows (No. 1026). US Government Printing Office.

Engelund, F., & Fredsøe, J. (1976). A sediment transport model for straight alluvial channels. *Hydrology Research*, 7(5), 293-306.

Engelund, F., & Fredsoe, J. (1982). Sediment ripples and dunes. *Annual Review of Fluid Mechanics*, 14(1), 13-37.

Farhoudi, J., & Smith, K. V. (1985). Local scour profiles downstream of hydraulic jump. *Journal of hydraulic research*, 23(4), 343-358.

Faulhaber, P. (1983). Ein Beitrag zur Anwendung aerodynamischer Modelle im wasserbaulichen Versuchswesen. *Wasserwirtschaft-Wassertechnik*, (8), 274-276.

Faulhaber, P. (1986). Aerodynamische Modellierung hydraulischer Abflüsse mit freier Oberfläche, *Mitteilungen der Forschungsanstalt für Schluffahrt, Wasser-und Grundbau*.

Fedele, J. J., & García, M. H. (2001). Alluvial roughness in streams with dunes: A boundary-layer approach. In *River, coastal and estuarine morphodynamics* (pp. 37-60). Springer, Berlin, Heidelberg.

Fredsoe, J., & Deigaard, R. (1992). *Mechanics of coastal sediment transport* (Vol. 3). World scientific publishing company.

Frings, R. M., & Kleinhans, M. G. (2008). Complex variations in sediment transport at three large river bifurcations during discharge waves in the river Rhine. *Sedimentology*, 55(5), 1145-1171.

Garcia, M. (Ed.). (2008, May). *Sedimentation engineering: processes, measurements, modeling, and practice*. American Society of Civil Engineers.

Gaudio, R., Marion, A., & Bovolin, V. (2000). Morphological effects of bed sills in degrading rivers. *Journal of hydraulic research*, 38(2), 89-96.

Gessler, J. (1968). The beginning of bedload movement of mixtures investigated as natural armoring in channels.

Giri, S., & Shimizu, Y. (2006). Numerical computation of sand dune migration with free surface flow. *Water Resources Research*, 42(10).

Gnanadesikan, Ramanathan, and Martin B. Wilk. "Probability plotting methods for the analysis of data." *Biometrika* 55.1 (1968): 1-17.

Goll, A. (2017). 3D numerical modelling of dune formation and dynamics in inland waterways. *3D Numerical Modelling of Dune Formation and Dynamics in Inland Waterways*, (103).

Goniva, C., Kloss, C., Deen, N. G., Kuipers, J. A., & Pirker, S. (2012). Influence of rolling friction on single spout fluidized bed simulation. *Particuology*, 10(5), 582-591.

Gomez, B., Hubbell, D. W., & Stevens Jr, H. H. (1990). At-a-point bed load sampling in the presence of dunes. *Water Resources Research*, 26(11), 2717-2731.

Guan, D., Melville, B. W., & Friedrich, H. (2014). Flow patterns and turbulence structures in a scour hole downstream of a submerged weir. *Journal of Hydraulic Engineering*, 140(1), 68-76.

Guy, H. P., Simons, D. B., & Richardson, E. V. (1966). Summary of alluvial channel data from flume experiments, 1956-61. US Government Printing Office.

HINCU, S., & FINKELSTEIN, A. (1963). Unele probleme ale analogiei hidroaerodinamice in modelarea proceselor de albii (Einige Fragen der hydroaerodynamischen Analogie bei der Modellierung von Flussbettprozessen). Studii de hidraulica V, Bukarest.

Hirt, C. W., & Nichols, B. D. (1981). Volume of fluid (VOF) method for the dynamics of free boundaries. *Journal of computational physics*, 39(1), 201-225.

Hoffmans, G. J., & Pilarczyk, K. W. (1995). Local scour downstream of hydraulic structures. *Journal of hydraulic engineering*, 121(4), 326-340.

Hogg, A. J., Huppert, H. E., & Dade, W. B. (1997). Erosion by planar turbulent wall jets. *Journal of Fluid Mechanics*, 338, 317-340.

Hunt, J. C., Wray, A. A., & Moin, P. (1988). Eddies, streams, and convergence zones in turbulent flows. *Studying turbulence using numerical simulation databases*, 2. Proceedings of the 1988 summer program.

Iseya, F. & Ikeda, H. (1986). Effect of dune development on sediment suspension under unsteady flow conditions. In *PROCEEDINGS OF THE JAPANESE CONFERENCE ON HYDRAULICS* (Vol. 30, pp. 505-510). Japan Society of Civil Engineers.

Jacobsen, N. G. (2011). A full hydro-and morphodynamic description of breaker bar development.

JCR, H., Wray, A., & Moin, P. (1988). Eddies, stream, and convergence zones in turbulent flows. *Studying Turbulence Using Numerical Simulation Databases-II*, 193.

Jerolmack, D. J., & Mohrig, D. (2005). Frozen dynamics of migrating bedforms. *Geology*, 33(1), 57-60.

Johnston, A. J. (1990). Scourhole developments in shallow tailwater. *Journal of hydraulic research*, 28(3), 341-354.

Jovic, S., & Driver, D. (1995). Reynolds number effect on the skin friction in separated flows behind a backward-facing step. *Experiments in Fluids*, 18(6), 464-467.

gaudio, P. Y. (2010). *Erosion and sedimentation*. Cambridge university press.

Kadota, A., & Nezu, I. (1999). Three-dimensional structure of space-time correlation on coherent vortices generated behind dune crest. *Journal of Hydraulic Research*, 37(1), 59-80.

Karim, O. A., & Ali, K. H. M. (2000). Prediction of flow patterns in local scour holes caused by turbulent water jets. *Journal of Hydraulic Research*, 38(4), 279-287.

Ke, F., Liu, Y. Z., Wang, W. Z., & Chen, H. P. (2006). Wall pressure fluctuations of turbulent flow over backward-facing step with and without entrainment: microphone array measurement. *Journal of Hydrodynamics*, 18(4), 393-396.

Khaleel, M. S., & Othman, K. I. (1997). Degradation downstream from a sluice gate; variation of bed and sediment characteristics with time and discharge. *Journal of hydrology*, 191(1-4), 349-363.

Kim, J., Kline, S. J., & Johnston, J. P. (1978). Investigation of Separation and Reattachment of a Turbulent Shear Layer: Flow over a Backward-Facing Step; Thermosciences Div., Dept. of Mechanical Engineering.

Kim S-C, Friedrichs CT, Maa JP-Y, Wright LD. 2000. Estimating bottom stress in tidal boundary layer from acoustic Doppler velocimeter data. *Journal of Hydraulic Engineering*, ASCE 126(6): 399–406.

Kim, S. J. (2020). Flow Characteristics through the Singok Submerged Weir in Downstream of the Han River. In *Proceedings of the Korea Water Resources Association Conference* (pp. 20-20). Korea Water Resources Association.

Kim, S. J., & Kim, C. S. (2020). Analysis of bed changes of the Nakdong River with opening the weir gate. *Ecology and Resilient Infrastructure*, 7(4), 353-365.

Kiya, M., & Sasaki, K. (1985). Structure of large-scale vortices and unsteady reverse flow in the reattaching zone of a turbulent separation bubble. *Journal of Fluid Mechanics*, 154, 463-491.

Khaleel, M. S., & Othman, K. I. (1997). Degradation downstream from a sluice gate; variation of bed and sediment characteristics with time and discharge. *Journal of hydrology*, 191(1-4), 349-363.

Khosronejad, A., & Sotiropoulos, F. (2014). Numerical simulation of sand waves in a turbulent open channel flow. *Journal of Fluid Mechanics*, 753, 150-216.

Kuehn, D. M. (1980). Effects of adverse pressure gradient on the incompressible reattaching flow over a rearward-facing step. *AIAA journal*, 18(3), 343-344.

Kwon, Y., Ji, U., & Jang, E. K. (2019). Numerical Analysis on Channel Width Variation for River Bed Stabilization Upstream of the Weir. *KSCE Journal of Civil Engineering*, 23, 2524-2531.

Laursen, E. M. (1952). Observations on the nature of scour. *Proceedings of 5th Hydraulics Conference.*, state University of Iowa. *Bulletin*, 34, 179-197.

Le Couturier, M. N., Grochowski, N. T., Heathershaw, A., Oikonomou, E., & Collins, M. B. (2000). Turbulent and macro-turbulent structures developed in the benthic boundary layer downstream of topographic features. *Estuarine, Coastal and Shelf Science*, 50(6), 817-833.

Lefebvre, A., & Winter, C. (2016). Predicting bed form roughness: the influence of lee side angle. *Geo-Marine Letters*, 36(2), 121-133.

Le, H., Moin, P., & Kim, J. (1997). Direct numerical simulation of turbulent flow over a backward-facing step. *Journal of fluid mechanics*, 330, 349-374.

Lilly, D. K. (1966). On the application of the eddy viscosity concept in the inertial sub-range of turbulence. *NCAR manuscript*, 123.

Liu, C. R., Huhe, A., & Tao, L. B. (2007). Experiment study on sediment incipience in backward-facing step flow. *Journal of Hydrodynamics*, 19(2), 173-179.

LJATCHER, W. M.; PRUDOVSKI, A.M. (1984): *Gidravliticheskoje modelirovanije* (Hydraulische Modellierung), Energoatomisdat, Moskau.

- Lu, S. S., & Willmarth, W. W. (1973). Measurements of the structure of the Reynolds stress in a turbulent boundary layer. *Journal of Fluid Mechanics*, 60(3), 481-511.
- Lyn, D. A. (1993). Turbulence measurements in open-channel flows over artificial bed forms. *Journal of Hydraulic Engineering*, 119(3), 306-326.
- Ma, H., Nittrouer, J. A., Naito, K., Fu, X., Zhang, Y., Moodie, A. J., ... & Parker, G. (2017). The exceptional sediment load of fine-grained dispersal systems: Example of the Yellow River, China. *Science advances*, 3(5), e1603114.
- McLean, S. R., Nelson, J. M., & Wolfe, S. R. (1994). Turbulence structure over two-dimensional bed forms: Implications for sediment transport. *Journal of Geophysical Research: Oceans*, 99(C6), 12729-12747.
- McLean, S. R., & Smith, J. D. (1979). Turbulence measurements in the boundary layer over a sand wave field. *Journal of Geophysical Research: Oceans*, 84(C12), 7791-7808.
- McLean, S. R., Wolfe, S. R., & Nelson, J. M. (1999). Predicting boundary shear stress and sediment transport over bed forms. *Journal of Hydraulic Engineering*, 125(7), 725-736.
- McLean, S. R., Wolfe, S. R., & Nelson, J. M. (1999). Spatially averaged flow over a wavy boundary revisited. *Journal of Geophysical Research: Oceans*, 104(C7), 15743-15753.
- Melville, B. W., & Coleman, S. E. (2000). *Bridge scour*. Water Resources Publication.
- Menter, F. R. (1992). Improved two-equation k-omega turbulence models for aerodynamic flows. *Nasa Sti/recon Technical Report N*, 93, 22809.

Moriasi, D.N.; Gitau, M.W.; Daggupati, P. Hydrologic and Water Quality Models: Performance Measures and Evaluation. *Trans. ASBE* 2015, 58, 1763–1785.

Müller, A., & Gyr, A. (1986). On the vortex formation in the mixing layer behind dunes. *Journal of Hydraulic Research*, 24(5), 359-375.

Müller, A., Grass, E., Wüest, A., & Gyr, A. (1987). Modelling of bubble plumes. In *Proc. Tech. Session B: Topics in Hydraulic Modelling*, 23rd IAHR Congress (pp. 348-353).

Nabi, M., De Vriend, H. J., Mosselman, E., Sloff, C. J., & Shimizu, Y. (2013). Detailed simulation of morphodynamics: 3. Ripples and dunes. *Water resources research*, 49(9), 5930-5943.

Nabi, M., Giri, S., Iwasaki, T., Kimura, I., & Shimizu, Y. (2014). Multi-scale modelling of river morphodynamics. *Proceedings of River Flow-2014*, Lausanne, Switzerland.

Nabi, M., Kimura, I., Hsu, S. M., Giri, S., & Shimizu, Y. (2015). Computational modeling of dissipation and regeneration of fluvial sand dunes under variable discharges. *Journal of Geophysical Research: Earth Surface*, 120(7), 1390-1403.

Nadge, P. M., & Govardhan, R. N. (2014). High Reynolds number flow over a backward-facing step: structure of the mean separation bubble. *Experiments in fluids*, 55(1), 1-22.

Nakagawa, H., & Nezu, I. (1981). Structure of space-time correlations of bursting phenomena in an open-channel flow. *Journal of Fluid Mechanics*, 104, 1-43.

Nakagawa, H., & Nezu, I. (1987). Experimental investigation on turbulent structure of backward-facing step flow in an open channel. *Journal of Hydraulic Research*, 25(1), 67-88.

Nelson, J. M., McLean, S. R., & Wolfe, S. R. (1993). Mean flow and turbulence fields over two-dimensional bed forms. *Water Resources Research*, 29(12), 3935-3953.

Nelson, J. M., McLean, S. R., & Wolfe, S. R. (1993). Mean flow and turbulence fields over two-dimensional bed forms. *Water Resources Research*, 29(12), 3935-3953.

Nelson, J. M., Shreve, R. L., McLean, S. R., & Drake, T. G. (1995). Role of near-bed turbulence structure in bed load transport and bed form mechanics. *Water resources research*, 31(8), 2071-2086.

Nestmann, F. (1992). Aerodynamische Modelle, eine strömungsmechanische Untersuchungsmethode zur Planung wasserbaulicher Maßnahmen. *Mitteilungen des Franzius-Instituts für Wasserbau und Küstenwesen, Hannover*, (73).

Nestmann, F., & Bachmeier, G. (1987). Anwendung von Luftmodellen im strömungsmechanischen Versuchswesen des Flussbaus. *Ehrenkolloquium für Herrn Prof. Gehrig am 27. März 1987*, (61), 65-98.

Nezu, I., & Nakagawa, H. (1987). Numerical calculation of turbulent open-channel flows in consideration of free-surface effect. *Memoirs of the Faculty of Engineering, Kyoto University*, 49(2), 111-145.

Nezu, I., & Nakagawa, H. (1989a). Accurate measurements of space-time correlations of coherent vortex behind dunes in turbulent open-channel flows with combination of laser-

Doppler anemometer and hot-film anemometer. In Proc. Workshop on Instrumentation for Hydraulics Laboratories, IAHR, Burlington, Canada (pp. 29-44).

Nezu, I., & Nakagawa, H. (1989b). Turbulent structure of backward-facing step flow and coherent vortex shedding from reattachment in open-channel flows. In *Turbulent shear flows 6* (pp. 313-337). Springer, Berlin, Heidelberg.

Nezu, I., Nakagawa, H., & Jirka, G. H. (1994). Turbulence in open-channel flows. *Journal of Hydraulic Engineering*, 120(10), 1235-1237.

Nguyen, V. T., Moreno, C. S., & Lyu, S. (2015). Numerical simulation of sediment transport and bedmorphology around Gangjeong Weir on Nakdong River. *KSCE Journal of Civil Engineering*, 19, 2291-2297.

Nie, J. H., & Armaly, B. F. (2004). Reverse flow regions in three-dimensional backward-facing step flow. *International journal of heat and mass transfer*, 47(22), 4713-4720.

Nik Hassan, N. M. K., & Narayanan, R. (1985). Local scour downstream of an apron. *Journal of Hydraulic Engineering*, 111(11), 1371-1384.

Niemann, S. L., Fredsøe, J., & Jacobsen, N. G. (2011). Sand dunes in steady flow at low Froude numbers: Dune height evolution and flow resistance. *Journal of Hydraulic Engineering*, 137(1), 5-14.

Nittrouer, J. A., Allison, M. A., & Campanella, R. (2008). Bedform transport rates for the lowermost Mississippi River. *Journal of Geophysical Research: Earth Surface*, 113(F3).

OpenCFD, L. T. D. (2009). OpenFOAM: The open source CFD toolbox.

Ötügen, M. V. (1991). Expansion ratio effects on the separated shear layer and reattachment downstream of a backward-facing step. *Experiments in fluids*, 10(5), 273-280.

Pagliara, S., & Palermo, M. (2015). Scour Problems Downstream of Low-Head Hydraulic Structures. In *Rivers—Physical, Fluvial and Environmental Processes* (pp. 99-119). Springer, Cham.

Park, J. H., & Lee, J. J. (2015). Analysis on the Water Level Variation due to Removing the Singok Submerged Weir in the Lower Han River. In *Proceedings of the Korea Water Resources Association Conference* (pp. 101-101). Korea Water Resources Association.

Perot, B., & Moin, P. (1995). Shear-free turbulent boundary layers. Part 1. Physical insights into near-wall turbulence. *Journal of Fluid Mechanics*, 295, 199-227.

Pope, S. B., & Pope, S. B. (2000). *Turbulent flows*. Cambridge university press.

Ra, S. H., & Chang, P. K. (1990). Effects of pressure gradient on reattaching flow downstream of a rearward-facing step. *Journal of aircraft*, 27(1), 93-95.

Rajaratnam, N., & Muralidhar, D. (1969). Flow below deeply submerged rectangular weirs. *Journal of Hydraulic Research*, 7(3), 355-374.

Raudkivi, A. J. (1966). Bed forms in alluvial channels. *Journal of Fluid Mechanics*, 26(3), 507-514.

Rodi, W., Constantinescu, G., & Stoesser, T. (2013). *Large-eddy simulation in hydraulics*.

Roulund, A., Sumer, B. M., Fredsøe, J., & Michelsen, J. (2005). Numerical and experimental investigation of flow and scour around a circular pile. *Journal of Fluid Mechanics*, 534, 351-401.

Roos, F. W., & Kegelman, J. T. (1986). Control of coherent structures in reattaching laminar and turbulent shear layers. *AIAA journal*, 24(12), 1956-1963.

Ruck, B., & Makiola, B. (1993). Flow separation over the inclined step. In *Physics of Separated Flows—Numerical, Experimental, and Theoretical Aspects* (pp. 47-55). Vieweg+ Teubner Verlag, Wiesbaden.

Schlichting H. 1987. *Boundary Layer Theory* (7th edition). McGraw-Hill: New York.

Schmeeckle, M. W. (2015). The role of velocity, pressure, and bed stress fluctuations in bed load transport over bed forms: numerical simulation downstream of a backward-facing step. *Earth Surface Dynamics*, 3(1), 105-112.

Shields, A. (1936). *Anwendung der Aehnlichkeitsmechanik und der Turbulenzforschung auf die Geschiebebewegung*. PhD Thesis Technical University Berlin.

Shimizu, Y., Giri, S., Yamaguchi, S., & Nelson, J. (2009). Numerical simulation of dune–flat bed transition and stage-discharge relationship with hysteresis effect. *Water Resources Research*, 45(4).

Smagorinsky, J. (1963). General circulation experiments with the primitive equations: I. The basic experiment. *Monthly weather review*, 91(3), 99-164.

Smith, J. D., & McLean, S. R. (1977). Spatially averaged flow over a wavy surface. *Journal of Geophysical research*, 82(12), 1735-1746.

Smith, J. D., & McLean, S. R. (1977). Boundary layer adjustments to bottom topography and suspended sediment. In *Elsevier oceanography series* (Vol. 19, pp. 123-151). Elsevier.

Sodja, J. (2007). *Turbulence models in CFD*. University of Ljubljana, 1-18.

Song, S., & Eaton, J. K. (2004). Reynolds number effects on a turbulent boundary layer with separation, reattachment, and recovery. *Experiments in fluids*, 36(2), 246-258.

Soulsby RL. 1983. The bottom boundary-layer in shelf seas. In *Physical Oceanography of Coastal and Shelf Areas*, Johns B (ed.). Elsevier: Amsterdam; 189–266.

Spazzini, P. G., Iuso, G., Onorato, M., Zurlo, N., & Di Cicca, G. M. (2001). Unsteady behavior of back-facing step flow. *Experiments in fluids*, 30(5), 551-561.

Sterling, M., Beaman, F., Morvan, H., & Wright, N. (2008). Bed-shear stress characteristics of a simple, prismatic, rectangular channel. *Journal of engineering mechanics*, 134(12), 1085-1094.

Stoesser, T., Braun, C., Garcia-Villalba, M., & Rodi, W. (2008). Turbulence structures in flow over two-dimensional dunes. *Journal of Hydraulic Engineering*, 134(1), 42-55.

Sumbal, J. (1966). Problematika podobnosti pri aerodynamickom modelovaní riečnych procesov.

Sun, R., & Xiao, H. (2016). CFD–DEM simulations of current-induced dune formation and morphological evolution. *Advances in water resources*, 92, 228-239.

- Syms, G. F. (2008). Simulation of simplified-frigate airwakes using a lattice-Boltzmann method. *Journal of Wind Engineering and Industrial Aerodynamics*, 96(6-7), 1197-1206.
- Tamoradi, Z., Ahadiyan, J., Najarchi, M., Hasounizadeh, H., & Najafizadeh, M. M. (2019). Reducing bend scour using in-phase and out-of-phase hydraulic jets. *Water Supply*, 19(5), 1446-1453.
- Tarapore, Z. S. (1956). Scour below a submerged sluice gate. University of Minnesota..
- Tjerry, S., & Fredsøe, J. (2005). Calculation of dune morphology. *Journal of Geophysical Research: Earth Surface*, 110(F4).
- Tipireddy, R. T., & Barkdoll, B. D. (2019). Scour reduction by air injection at a cylindrical bridge pier: Experimental determination of optimal configuration. *Journal of Hydraulic Engineering*, 145(1), 06018016.
- Tregnaghi, M., Marion, A., & Gaudio, R. (2007). Affinity and similarity of local scour holes at bed sills. *Water Resources Research*, 43(11).
- Tropea, C. D. (1982). Turbulent step flow in flat channels and open mouldings. *Die turbulente Stufenstroemung in Flachkanaelen und offenen Gerinnen*.
- Tylli, N., Kaiktsis, L., & Ineichen, B. (2002). Sidewall effects in flow over a backward-facing step: Experiments and numerical simulations. *Physics of Fluids*, 14(11), 3835-3845.

Uchida, T., & Fukuoka, S. (2013). Quasi 3D numerical simulation for flow and bed variation with various sand waves. *Advances in River Sediment Research—Fukuoka et al.(eds)*, 221-229.

Van Driest, E. R. (1956). On turbulent flow near a wall. *Journal of the aeronautical sciences*, 23(11), 1007-1011.

Van Mierlo, M. C. L. M., & De Ruiter, J. C. C. (1988). Turbulence measurements above artificial dunes. Q0789.

Vanoni, V. A. (Ed.). (2006, March). *Sedimentation engineering*. American Society of Civil Engineers.

Venditti, J. G., & Bennett, S. J. (2000). Spectral analysis of turbulent flow and suspended sediment transport over fixed dunes. *Journal of Geophysical Research: Oceans*, 105(C9), 22035-22047.

Venditti, J. G., Church, M., & Bennett, S. J. (2005). Morphodynamics of small-scale superimposed sand waves over migrating dune bed forms. *Water resources research*, 41(10).

Villard, P., & Kostaschuk, R. (1998). The relation between shear velocity and suspended sediment concentration over dunes: Fraser Estuary, Canada. *Marine Geology*, 148(1-2), 71-81.

Wang, F., Gao, A., Wu, S., Zhu, S., Dai, J., & Liao, Q. (2019). Experimental Investigation of Coherent Vortex Structures in a Backward-Facing Step Flow. *Water*, 11(12), 2629.

Westphal, R. V., Johnston, J. P., & Eaton, J. K. (1984). Experimental study of flow reattachment in a single-sided sudden expansion (pp. 1932-1932). NASA.

Williams, P. T., & Baker, A. J. (1997). Numerical simulations of laminar flow over a 3D backward-facing step. *International Journal for Numerical Methods in Fluids*, 24(11), 1159-1183.

Wu, F. C., & Lin, Y. C. (2002). Pickup probability of sediment under log-normal velocity distribution. *Journal of Hydraulic Engineering*, 128(4), 438-442.

Wu, S., & Rajaratnam, N. (1996). Submerged flow regimes of rectangular sharp-crested weirs. *Journal of Hydraulic Engineering*, 122(7), 412-414.

Wu, S., & Rajaratnam, N. (1998). Impinging jet and surface flow regimes at drop. *Journal of Hydraulic Research*, 36(1), 69-74.

Yalin, M. S.~1977!.Mechanics of sediment transport, Pergamon, Oxford.946/ JOURNAL OF HYDRAULIC ENGINEERING / OCTOBER 2002

유인상, 오국열, 진기현, & 정상만. (2012). 공주보 건설에 따른 하상변동 모니터링. *한국수자원학회/ 학술발표회*, 685-685.

Appendix

1. Terminologies

This chapter briefly defines the terminologies related to this study.

- Surface flow: the flow at a velocity that is not sufficient to create a plunging flow. The free-surface effect is normally negligible. This type of flow can occur in both natural and man-made channels, such as rivers, streams, and canals, as well as in open channels of hydraulic structures like weirs and spillways. The free-surface effect is normally negligible for this flow regime.
- Submerged wall jet flow: the near-bed jet flow when a sluice gate is opening. This flow is typically bounded by two shear layers, one at the outer edge of the flow and another at the wall. This flow type can cause significant scouring of the bed due to the high velocity and turbulence of the flow.
- Backward-Facing Step (BFS): a BFS is a sudden expansion in a channel where the flow separates. It is commonly used as a benchmark flow problem in computational fluid dynamics (CFD) and experimental studies. The study of BFS flows can provide insights into the flow and turbulence characteristics of hydraulic structures.
- Separated Shear Layer (SSL): the boundary layer which is separated at the step edge due to the sudden change of cross-sectional area. In turbulence regime, the vortices along this SSL grow and fluctuate near the bed giving rise to large turbulent intensity and sediment transport.

- Separation zone: the area in which the fluctuating streamline along the SSL covers on the bed.
- Reattachment length: the distance from the step edge to the point where the mean streamwise velocity changes from negative to positive sign on the vicinity of the bed. In other words, it denotes the point at which the mean dividing streamline impacts the bed.
- Bedload: the sediment flux of the grains moving along the bed. It moves close to the bed in rolling, dragging, and saltation. The bed load consists of the larger sediment compared to suspended load.
- Incipient motion: the threshold at which the sediment begins to move. Conventionally, this incipient motion have been determined following Shields diagram, but in this study, the incipient motion of each particle is determined by DEM, a lagrangian approach.
- Sediment transport: the term used in a broad sense defined as the movement of sediment by flow field.
- Scour: the term used in a wide sense to indicate erosion of bed material or sediment transport, but more frequently used in a narrower sense as local bed erosion.

2. Turbulence concepts

In numerical simulations, Reynolds-Averaged Navier-Stokes (RANS), Large Eddy Simulation (LES), and Direct Numerical Simulation (DNS) are commonly used to simulate turbulent flows. They differ in their complexity, computational cost, and the amount of turbulent flow detail they can capture.

RANS is a widely used method that simplifies the Navier-Stokes equations by averaging the flow variables over time, separating them into mean and fluctuating components. The time-averaging process results in the appearance of additional stress terms known as Reynolds stresses, which need to be modeled using turbulence models like k-epsilon or k-omega. RANS is computationally efficient, making it suitable for practical engineering applications. However, it has limitations in capturing unsteady flow features and complex flow structures.

LES is an intermediate approach between RANS and DNS. It filters the flow field, separating it into large-scale, resolved turbulent structures (eddies) and smaller, unresolved scales. The large-scale motions are directly resolved in the simulation, while the smaller-scale motions are modeled using subgrid-scale (SGS) models. LES is more computationally expensive than RANS but provides greater accuracy in capturing unsteady flow features and complex flow structures, making it suitable for studying turbulent flow phenomena.

DNS is the most accurate but computationally expensive method among the three. It directly solves the Navier-Stokes equations for all turbulent scales without any turbulence

model, requiring very fine spatial and temporal discretization. This makes DNS impractical for most real-world engineering applications but highly valuable for fundamental turbulence research and validating other turbulence models.

In this study, the Large Eddy Simulation (LES) approach is employed to accurately reproduce turbulent flow structures. The advantages of using LES can be summarized as follows:

1. LES captures a wider range of turbulent scales compared to RANS, providing better insight into the complex flow structures.
2. LES is capable of simulating unsteady and transient flow phenomena that are often missed by RANS.
3. LES can provide more accurate and detailed flow predictions, especially for complex geometries and flow regimes.
4. While more computationally expensive than RANS, LES is still less demanding than DNS, making it a practical choice for studying turbulent flows in many engineering applications.

In summary, Reynolds-Averaged Navier-Stokes (RANS), Large Eddy Simulation (LES), and Direct Numerical Simulation (DNS) differ in terms of complexity, computational cost, and the level of detail they can capture in turbulent flow. LES provides a balance between accuracy and computational cost, making it a valuable tool for replicating turbulent flow structures and investigating unsteady flow phenomena. Figure 68 presents a schematic representation of the turbulence length scales resolved and modeled by these three turbulence models.

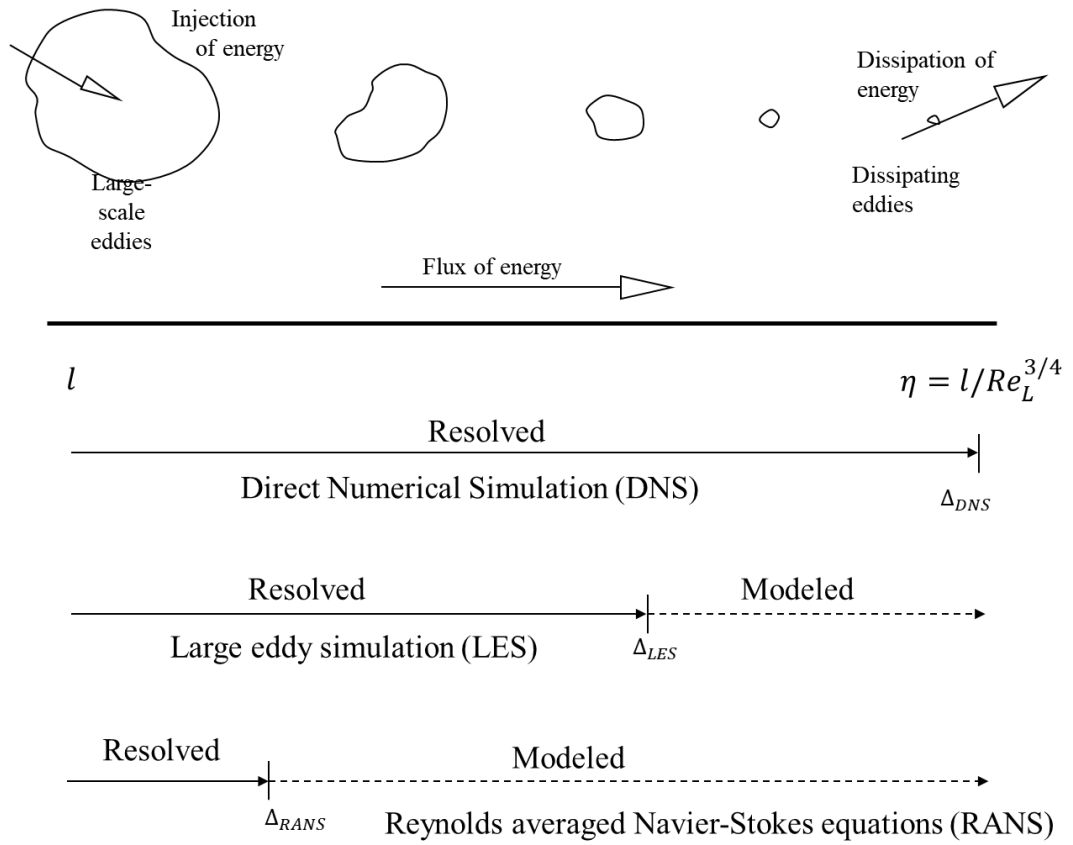


Figure 68. Schematic diagram of backward-facing step flow, re-adapted from Sodja, (2007).

초 록

수공구조물 인근 흐름에 대한 연구는 흐름 특성과 유사 거동의 복잡성으로 인해 여전히 많은 관심을 받고 있다. 이러한 측면에서 본 논문은 다양하게 경사진 후향 계단과 수문과 같은 수공구조물 배후의 흐름 및 유사 거동을 수치모의를 통해 규명하였다. 우선 표면 제트 흐름에서 후향 계단 각도가 벽 근처 난류 흐름 구조 및 소류사 이송률, 그리고 이들의 상호작용에 미치는 영향을 분석하였다. 오픈 소스 3 차원 유동해석 프로그램인 OpenFOAM 에 기반한 large eddy simulation (LES)과 discrete element method (DEM)의 결합 모델이 수치모형으로 차용되었다. 해당 수치모형은 수치모의 결과와 다양한 실험에서 취득한 데이터 간의 높은 상관성을 확인함으로써 적절히 검증되었다. 수치모의 결과는 후향 계단 각도가 20° 보다 작을 때 유동 박리가 발생하지 않으며, 이러한 경우 벽 근처 난류 강도가 유사를 활발히 이송시키기에는 충분히 크지 않다는 것을 나타냈다. 후향 계단 각도가 20° 보다 커졌을 때 유동 박리현상이 관측되었으며 결과적으로 벽 근처 난류 강도가 splat 효과로 인해 현저히 증가하였고, 이에 따라 유사 이송률도 급격히 증가하였다. 후향 계단 각도가 30° 와 90° 로 더욱 증가하였을 때, 재부착 길이 또한 증가하는 경향을 보였지만 벽 근처 최대 난류 강도는 거의 변하지 않았다. 평균 소류사 이송률의 최고점은 재부착 길이가 증가함에 따라 더 하류에서 관측되었다. 또한 벽 근처 흐름 구조와 소류사 이송의 상호작용을 규명하기 위해 사분면 분석이 수행되었다. 사분면 분석 수행 결과, 재부착 지점 직전에는

sweep 이, 직후에는 burst 가 소류사를 각각 흐름 방향, 흐름 반대 방향으로 이송시키는 주요한 난류 사건이라는 것이 규명되었다. 더 나아가, 본 논문에서는 수문 열림에 의한 벽 제트 흐름에서 바닥보호공 배후 흐름 및 유사 거동의 특성 또한 수치적 방법으로 조사하였다. 이 흐름 영역에서는 넓은 면적 공기주입법이 세굴 완화에 미치는 영향이 평가되었다. 이를 위해 LES-DEM 결합 모형의 지배 방정식에 대한 소스 코드를 공기상을 포함하도록 수정하였다. 수치모의를 통해 산출된 벽 근처 평균 유속과 바닥보호공 배후 저면 형상은 실험에서 관측된 데이터와 적절하게 일치하는 것을 확인하였다. 수치모의 결과, 소류사 이송률과 최대 세굴심은 벽 근처 흐름 방향 평균 유속을 감소시키는 공기 주입에 의해 현저하게 감소하는 것으로 판명되었다. 이러한 결과는 흐름 방향 평균 유속을 감소시키는 것이 직접적으로 세굴을 완화시키는 가장 주요한 요인이라는 것을 암시한다. 이에 반해, 연직 방향 평균 유속과 난류 강도는 공기 주입으로 인해 현저하게 증가하였지만, 이들은 유사 거동에 기여하는 바는 거의 없는 것으로 나타났다. 최대 세굴심은 공기 유입량이 증가할수록, 그리고 공기 주입 면적이 늘어날수록 감소하는 것으로 확인되었다. 또한, 소류사 이송에 대한 사분면 분석 결과를 통해 공기 주입이 없을 때 주 난류 사건인 sweep 에 의해 초기 세굴량이 증가하는 것을 확인하였으며, 공기 주입이 있을 때는 outward 와 inward interaction 이 주 난류 사건으로 작용하면서 초기 세굴량이 급격하게 감소하는 것을 규명하였다.

주요어 : 소류사 이송; LES-DEM 결합 모형; 재부착 길이; 벽 제트 흐름; 표면 제트 흐름; 넓은 면적 공기 주입법

학 번 : 2017-31683

감사의 글

석사 과정을 포함하여 박사 과정까지, 대학원생으로서의 모든 마침표를 찍고 이렇게 감사의 글을 쓰니 감회가 무척 새롭습니다. 처음에는 석사까지만 해보자는 마음가짐으로 대학원에 입학하였지만 훌륭한 교수님과 좋은 선배님들이 귀감이 되어 박사 과정 진학이라는 길을 선택하는 큰 계기가 되었습니다. 우선, 대학원의 시작인 석사 과정 동안 논문을 성심껏 지도해 주셨던 조용준 교수님께 감사의 말씀을 드리고 싶습니다. 교수님과 함께 논문 정독을 했던 경험과 수치 모형을 분석하고 수정했던 경험이 박사 과정 동안 새로운 것을 공부하고 연구하는 데 큰 도움이 되었습니다. 그리고 오랜 박사과정 기간 동안 논문을 지도해 주신 Van Thinh Nguyen 교수님께 깊은 감사의 말씀을 드립니다. 교수님과 함께 했던 경험들은 제가 연구자로서 혼자서 연구할 수 있는 방법을 터득할 수 있는 좋은 발판이 되었습니다. 마지막까지 아낌없이 격려해 주시고 잘 지도해 주셔서 박사학위 논문을 잘 마무리할 수 있었습니다. 또한 귀중한 시간 내 주시어 오랜 연구 경험과 깊은 식견으로 제 학위논문이 더욱 완성도를 갖출 수 있도록 검토해 주시고 피드백을 주신 박용성 교수님, 우효섭 교수님, 송창근 교수님, 그리고 Philippe Gourbesville 교수님께도 깊은 감사의 말씀을 드립니다. 교수님들께 받은 가르침을 토대로 배움의 끈을 놓지 않으며 사회에 보탬이 될 수 있도록 노력하겠습니다.

또한, 오랜 학위 과정 동안 믿고 지지해 주신 가족들에게도 감사를 전합니다. 한결같이 올곧은 가치관으로 항상 귀감이 되어 주시는 아버지, 항상 밝고 긍정적으로 기다려 주시는 어머니, 그리고 자기 일에 최선을 다하며 집안 분위기를 항상 밝게 이끌어주는 형에게 미안함과 감사함을 전합니다.

그리고 박사 과정 기간 동안 물심양면으로 많은 도움을 주신 홍창배 이사님과 김신웅 박사님께도 감사의 말씀을 전합니다. 많은 좋은 말씀과 기회를 주셔서 부족했던 제가 조금 더 우리 학문 분야에 필요한 사람으로 성장하는 데 도움이 되었습니다. 또한, 오랜 시간 같은 수치 모형을 사용하면서 함께 논의하며 위안이 되어 준 최성은 박사에게도 고마움을 전합니다.

지면에 다 적지는 못하였지만, 지금까지의 시간을 함께해 주신 여러 선후배님들과 지인들께도 감사드립니다. 모든 분들에게 받은 도움들을 꼭 잊지 않고 저 또한 다른 사람들에게 도움이 될 수 있는 사람으로 발전해 나가도록 하겠습니다.